Astronomy Reports, Vol. 47, No. 5, 2003, pp. 357–376. Translated from Astronomicheskiĭ Zhurnal, Vol. 80, No. 5, 2003, pp. 387–408.

Minimum Velocity Dispersion in Stable Stellar Disks. Numerical Simulations

A. V. Khoperskov[1], A. V. Zasov[1], and N. V. Tyurina[1]

[1] *Sternberg Astronomical Institute, Universitetskiĭ pr. 13, Moscow, 119992 Russia*

Received February 20, 2002; in final form, November 27, 2002

Abstract—N-body dynamical simulations are used to analyze the conditions for the gravitational stability of a three-dimensional stellar disk in the gravitational field of two rigid spherical components—a bulge and halo whose central concentrations and relative masses vary over wide ranges. The number of point masses N in the simulations varies from 40 to 500 000 and the evolution of the simulated systems is followed over 10–20 rotation periods of the outer edge of the disk. The initially unstable disks are heated and, as a rule, reach a quasi-stationary equilibrium with a steady-state radial-velocity dispersion c_r over five to eight turns. The radial behavior of the Toomre stability parameter $Q_T(r)$ for the final state of the disk is estimated. Simple models are used to analyze the dependence of the gravitational stability of the disk on the relative masses of the spherical components, disk thickness, degree of differential rotation, and initial state of the disk. Formal application of existing, analytical, local criteria for marginal stability of the disk can lead to errors in c_r of more than a factor of 1.5. It is suggested that the approximate constancy of $Q_T \simeq 1.2$–1.5 for $r \simeq (1$–$2) \times L$ (where L is the radial scale of disk surface density), valid for a wide range of models, can be used to estimate upper limits for the mass and density of a disk based on the observed distributions of the rotational velocity of the gaseous component and of the stellar velocity dispersion.

1. INTRODUCTION

Galactic disks, which consist mostly of old stars, can be considered as collisionless systems in quasi-stationary equilibrium with very slow evolution. This state is characterized by certain radial dependences of the stellar velocity dispersions (c_r, c_φ, c_z) that ensure stability of the disk. Knowledge of the stability conditions makes it possible to develop self-consistent models for the disks of real galaxies for which both the rotational velocities and stellar velocity dispersions have been measured at various galactocentric distances.

The problem of determining the minimum stellar velocity dispersion sufficient to ensure stability of the disk against arbitrary perturbations is especially important if, as many authors have suggested (see, e.g., [1–7]), real galaxies are in a state of threshold (marginal) stability. This approach enables the local density or integrated mass of the disk to be estimated from the observed velocity dispersion. In the general case, the old stellar population of a galactic disk can have an excess velocity dispersion in the presence of other factors that heat the disk, which are not directly related to the gravitational instability. However, even in this case, the conditions for marginal stability provide valuable information by yielding an upper limit for the mass of the disk that enables it to be stable.

Fridman and Polyachenko [8, 9] carried out a detailed theoretical analysis of the stability of thin rotating disks against various perturbations (including bending modes). Together with certain advantages over numerical simulations (the mathematical rigorousness of the solutions in the framework of the problem formulated), the analytical approach to the dynamics of perturbations in a gravitating disk and the conditions for stability has the drawback that it can be implemented only using very simple models and can yield only coarse estimates for the parameters of the disk component when applied to real objects. Let us consider these simplifications in more detail.

First and foremost, the simple analytical models for collisionless disks that are used in stability analyses usually assume that the disk thickness is small; they actually consider an infinitely thin layer. Despite the smallness of the ratios h_z/r and h_z/L over most of the stellar disk (here, r is the radial coordinate, h_z the vertical scale height, and L the radial scale length for inhomogeneity of the disk), this condition may not be sufficient to justify neglect of vertical motions (see Gor'kavyi and Fridman [10, Appendix II[1]] for a detailed discussion of this issue; in the general case, the dynamics equations for astrophysical disks cannot be adequately treated in a two-dimensional formulation).

[1] Written in coauthorship with O.V. Khoruzhiĭ.

1063-7729/03/4705-0357$24.00

Analytical studies of the dynamics of small perturbations in a stellar disk usually assume that the disk parameters have small radial gradients (see, e.g., [1, 11, 12]). Attempts to allow for gradients have thus far been made only in terms of WKB approximations (see, e.g., [2, 13–15]). This means that the characteristic perturbation wavelength must be short compared to the local scale lengths for variations of the equilibrium rotational velocity $V(r)$, stellar radial-velocity dispersion $c_r(r)$, and surface density $\sigma(r)$. In many cases, these conditions are barely satisfied or even not satisfied. Taking into account differential rotation may pose the most difficult problem. Allowance for weakly differential rotation is possible for weakly nonradial perturbations [13, 16]. However, nonaxisymmetric (in the limiting case, spoke-like) perturbations are more unstable. Their stabilization under the same conditions requires significantly stronger disk heating, i.e., a higher stellar velocity dispersion [17], and these very perturbations apparently increase the stellar velocity dispersion at the nonlinear stage in the case of initially cool systems.

Analytical studies of the gravitational stability of disks usually apply the epicyclic approximation $c_r \ll V$, which is valid at the peripheries of most galaxies, where $c_r/V \simeq 0.1$–0.3, but breaks down near their centers, where $c_r \gtrsim V$.

Another important limitation of analytical approaches is that the criteria derived are local, whereas a number of studies suggest that the disk stability conditions have a global nature [18, 19]. This means that variation of the equilibrium parameters, e.g., at the center, while leaving their values at the disk periphery unchanged, it may affect the conditions for gravitational stability throughout the disk. In contrast to a local approach based on the analysis of dispersion equations, global analyses aim to determine the eigenfrequency for the entire disk by solving a boundary-value problem, which determines the influence of the conditions in one part of the system on the dispersion properties of the perturbations throughout the disk. Therefore, in a rigorous approach, the disk must be considered as a whole. However, global analyses have been performed only for certain specific power-law distributions [18–20]. For example, Bertin *et al.* [21] considered global modes in galactic disks as possible mechanisms for maintaining long-lived spiral density waves.

Numerical simulations of collisionless systems are more flexible in terms of the choice of model. They make it possible to go beyond simple two-dimensional models and directly follow the development of perturbations in a disk that is initially in equilibrium. However, this approach has drawbacks of its own. The most serious problems of N-body simulations include (1) certain mathematical simplifications that are inevitable when a disk is modeled as a system of N gravitating bodies, where N is incomparably smaller than the number of stars in real galaxies, and (2) the dependence of the final state of the system (after it reaches quasi-equilibrium) on the initial parameters, which are poorly known for real galaxies. When comparing simulation results with real galaxies, it can also be difficult to allow for the dissipative galactic medium (gas), in which the sound speed is much lower than the stellar velocity dispersion. We consider these problems in more detail below.

The principal goal of this study is to determine for galaxies with various mass distributions the minimum local disk velocity dispersions that enable their three-dimensional disks, which are initially in a weakly unstable equilibrium, to reach a quasi-stationary state. Sections 2 and 3 give a concise review of previous results of analytical and numerical approaches to estimating the stellar velocity dispersions required to ensure the stability of collisionless disks. Section 4 describes the principles underlying the construction of the dynamical models and the determination of the stability threshold used in this paper. Section 5 considers various three-dimensional models of galaxies, and the last section presents and discusses our main conclusions.

2. ANALYTICAL STABILITY CRITERIA

Several criteria for gravitational instability derived analytically using various models have been published. Let us review those we consider to be most important.

(a) The Toomre Criterion

In order for an infinitely thin, uniform, rigidly rotating stellar disk to be gravitationally stable against axisymmetric perturbations, it must satisfy the following condition derived by Toomre [1]:

$$c_r \geq c_T = \frac{3.36G\sigma}{\varkappa}, \qquad Q_T = \frac{c_r}{c_T} \geq 1, \quad (1)$$

where $\varkappa = 2\Omega\sqrt{1 + rd\Omega/2\Omega dr}$ is the epicyclic frequency and σ is the surface density. Condition (1) assumes that the epicyclic approximation is valid, i.e., that the difference between the velocity $V(r)$ and the circular velocity $V_c(r)$ can be neglected. Although this relation was derived in a local analysis, the study of Evans and Read [19] of the eigenmodes for self-similar disks in a corresponding approximation overall supports its validity. Miller [22] compared the theoretical increments derived for a Toomre model with the results of simulations of axisymmetric modes in

which all other perturbations were artificially suppressed. Experimental gradients were shown to be consistent with the theoretical results.

(b) Allowance for Finite Disk Thickness

Finite thickness is a stabilizing factor for gravitational instability in the plane of the disk [9, 12]. The generalization of the Toomre stability criterion (1) for the case of a disk of finite thickness obtained by Morozov [13, 14, 16] has the form

$$Q_T^{(1)} = \frac{1}{1 + 0.974\Delta\varkappa/c_r} < 1, \qquad (2)$$

where Δ is the half-thickness of the isothermal self-gravitating disk. However, this condition proved to be far from sufficient to ensure the stability of real systems. This became clear from the first numerical simulations performed in the 1970s, which showed that $c_r \simeq (1.5\text{–}5) \times c_T$ at the periphery of a stationary, collisionless disk [23–30].

(c) Simplified Allowance for Nonaxisymmetric Perturbations

The stronger instability of spiral waves compared to axisymmetric modes is one of the factors that makes the Toomre criterion inadequate. Polyachenko and Shukhman [31], Kalnajs [32], and Polyachenko and Fridman [9] were the first to show that nonaxisymmetric modes are the dominant instabilities in a gravitationally unstable disk. As pointed out by Polyachenko and Fridman [9], the azimuthal-velocity dispersion c_φ is smaller than c_r (except in the innermost regions). Therefore, the relation

$$c_\varphi = c_r \frac{\varkappa}{2\Omega}, \qquad (3)$$

implies that, in order for an azimuthally cooler disk to be stabilized, it must be heated more strongly, so that, in view of (3), the condition (1) can be rewritten in the form

$$Q_T^{(2)} \geq S, \qquad S = \frac{2\Omega}{\varkappa}. \qquad (4)$$

The parameter S characterizes the degree of differential rotation of the disk. In most cases, we can assume that $1 \leq S \leq 2$, based on the observed shapes of galactic rotation curves. This form of the stability condition is discussed in [13–16].

Thus, the azimuthal-velocity dispersion determines the elasticity of the medium against strongly nonaxisymmetric perturbations, and the suppression of gravitational instability requires stronger heating of the disk by a factor of $2\Omega/\varkappa$.

Criterion (4) can be considered the Toomre criterion with a simplified allowance for nonaxisymmetric perturbations.

(d) The Morozov Criterion

Morozov [13], Morozov and Khoperskov [14], and Morozov [16] analyzed the dynamics of weakly nonradial perturbations in a nonuniform disk in a WKB approximation. The resulting stability criterion takes into account many factors (radial nonuniformity of the surface density σ and radial-velocity dispersion c_r, the disk thickness, and differential rotation):

$$Q_T^{(M)} = c^{(M)}/c_T, \qquad (5)$$

$$c^{(M)} = SDc_T\left\{1 + 1.07 \times \left|1.87S\frac{c_T}{\varkappa}\left(\frac{d\sigma}{\sigma dr} + \frac{dS}{Sdr} - 1.09\frac{dc^{(M)}}{c^{(M)}dr}\right)\right|^{2/3}\right\},$$

where $S = 2\Omega/\varkappa$ and $D = (1 + 0.974\varkappa\Delta/(S^2 c_T))^{-1}$. In the general case, determining $c^{(M)}$ from (5) amounts to integrating a reduced differential equation [33]. The main drawback of this criterion is that it was derived in the context of the dynamics of tightly wound spiral waves ($m/r \ll k_r$, where k_r is the radial wavenumber) and then formally applied to spokelike perturbations.

If the scale length $L_c \equiv (d\ln c^{(M)}/dr)^{-1}$ is fixed, the differential equation (5) reduces to a simple algebraic relation [13, 14, 16]. For typical rotation-curve shapes, we have $D \simeq 0.6\text{–}0.8$. Introducing the factor D also makes it possible to formally allow for the disk thickness in criteria (3) and (6).

(e) The Polyachenko–Polyachenko–Strel'nikov Criterion

Unlike the criteria discussed above, the analysis of Polyachenko *et al.* [17] focused on extremely nonaxisymmetric perturbations in a thin disk. Under the assumptions made, the rotation curve is the sole factor determining the stability boundary, since this boundary depends only on the parameter $n \equiv -rd\Omega/(\Omega dr)$. Figure 1 in [17] shows the dependence of the dimensionless velocity dispersion at the stability boundary on the parameter $\alpha = 2/n$. We will use the approximating function

$$Q_T^{(P)} = \frac{c^{(P)}}{c_T} = 1.88\sqrt{1.1 + \frac{8}{\exp(\alpha - 1/4) - 1}}, \qquad (6)$$

where $Q_T^{(P)}$ is the minimum Toomre parameter for a stable disk.

This approximation has sufficient accuracy for our needs when $1.2 < \alpha^2$. The criterion of Polyachenko *et al.* [17] depends on a single parameter, since the form of the rotation curve fully determines the stability boundary. In particular, it follows that $Q_T^{(P)} \simeq 3$ in the region with constant rotational velocity ($n = 1$).

(f) Allowance for the Gaseous Subsystem in a Stability Analysis for Stellar Disks

The presence of a cooler component also contributes to destabilization of the stellar disk. A number of authors [34–38] have analyzed this problem in detail as applied to radial perturbations. Ortega *et al.* [38] considered a more general problem: they analyzed how the inhomogeneous composition of a thin disk influences the stability of the disk against small radial perturbations when the disk consists of particles having a mass spectrum such that more massive particles have lower velocity dispersions.

The problem is simplified if the mass of the "cool" component is relatively small. Assuming the gas surface density $\sigma_{\rm gas}$ to be usually much lower than the surface density of the stellar disk $\sigma_{\rm star}$ and $c_s \ll c_r$ (where c_s is the adiabatic sound speed in the gas), we can write for the velocity dispersion of a stellar disk containing gas at the stability boundary [37]

$$\frac{c_r^{\rm crit}}{c_T} = 1 + \frac{\sigma_{\rm gas}}{\sigma_{\rm gas} + \sigma_{\rm star}} \frac{1 - (c_s/c_T)^2}{1 + (c_s/c_T)^2}. \qquad (7)$$

For example, for the parameters of the solar neighborhood in the Galaxy, it follows from (7) that the gaseous subsystem, which contributes about 20% of the disk surface density, increases the minimum stellar-velocity dispersion sufficient for stabilizing radial perturbations by $\leq 10\%$.

Finally, we note that attempts have also been made to determine the parameters of the disk subsystem using other approaches based on the possible existence of various structures in the disk (spiral density waves or a bar) rather than on local stability conditions, assuming certain mechanisms that form and sustain these structures. However, the analysis of these approaches is beyond the scope of this paper.

3. ANALYSIS OF GRAVITATIONAL STABILITY IN NUMERICAL SIMULATIONS

Numerical simulations describing the dynamical evolution of disks can be used to analyze disk instabilities for given initial conditions allowing for nonuniform distributions of the mass and angular velocity. Such simulations naturally take into account the formation of appreciably nonlinear and nonaxisymmetric structures such as bars or transient spirals. The main problem with this approach is that the results depend on the initial conditions, since the evolution of a disk starting from a strongly unstable state can proceed very differently from the evolution of a disk starting in a subcritical state. Moreover, the disk can suffer from slow secular instabilities that are difficult to take into account in numerical simulations.

N-body evolutionary models are usually aimed at studying the development of instability or—which is of the most interest for us—analyzing the states of a system after many disk rotations. Of the large number of published studies of this type, we will mention those that are, in our view, most important in the context of establishing the conditions for stability of a disk.

Carlberg and Sellwood [39, 40] analyzed the influence of small, nonstationary perturbations of the potential on the evolution of the velocity-distribution function. In particular, they analyzed scattering by nonstationary spiral waves; the resulting growth of the stellar-velocity dispersion agrees well with the results of numerical simulations.

The critical velocity dispersion for stellar disks (the parameter Q_T) has been computed many times based on the results of N-body dynamical simulations (see, e.g., [7, 24, 28, 33, 40–46]). None of the simulations yielded a stable disk with $Q_T < 1$. As a rule, $Q_T(r)$ increases with distance from the center of the galaxy. This pattern appears both in simulations of three-dimensional disks [5, 46–48] and in some theoretical analyses [49].

The work of Athanassoula and Sellwood [34] can be considered to be classic. They concluded that a two-dimensional disk is always stable if its Toomre parameter exceeds $Q_T \gtrsim 2.2$–2.4. However, this conclusion did not take into account vertical motions. Since three-dimensional disks are gravitationally more stable, two-dimensional models underestimate the mass of a marginally stable disk. In addition, Athanassoula and Sellwood [34] used a radially averaged Q_T and simulated a specific density distribution based on a Toomre–Kuz'min model. It is therefore not clear whether their results are applicable for real three-dimensional disks.

4. CONSTRUCTION OF NUMERICAL MODELS. SPECIFYING INITIAL CONDITIONS

The dynamical models used in this paper are based on numerical integration of the equations of motion for N gravitationally interacting particles taking into account the external field produced by the steady-state mass distribution in the bulge and halo.

For the halo, we adopted the commonly used spatial distribution of the volume density in the form

$$\varrho_h(\xi) = \frac{\varrho_{h0}}{(1 + \xi^2/a^2)^k}, \qquad (8)$$

where $\xi = \sqrt{r^2 + z^2}$ is the radial coordinate. Choosing $k = 1$ yields a flat rotation curve in the halo-dominated region. The relative central density of the spherical component increases with k, imitating the influence of the bulge. Because the bulge enters our model as a separate spherical component, we restrict our analysis to a halo model with $k = 1$.

The following set of equations describes the dynamics of the N gravitating bodies:

$$\frac{d^2 r_i}{dt^2} = \sum_j^N \mathbf{f}_{ij} + \mathbf{F}_s \quad (i = 1, ..., N). \tag{9}$$

Here, the radius vector $\mathbf{r}_i(t)$ determines the position of the ith particle, $\mathbf{f}_{ij}$ is the force of interaction between the ith and jth particles, and the force $\mathbf{F}_s = \mathbf{F}_b + \mathbf{F}_h$ is due to the bulge/halo spheroidal subsystem. The halo mass distribution (8) with a central density of $\varrho_{h0} = M_h/\{4\pi a^3[R/a - \arctan(R/a)]\}$ yields for the force

$$\mathbf{F}_h(\xi) = -\frac{4\pi G a^3 \varrho_{h0}}{\xi^2}\left\{\frac{\xi}{a} - \arctan\left(\frac{\xi}{a}\right)\right\}\frac{\mathbf{r}}{\xi}, \tag{10}$$

which is determined by the spatial scale lengths a and mass M_h inside the sphere $\xi = |\mathbf{r}| < R$. We adopt a King model for the density distribution in the spherical bulge:

$$\varrho_b = \begin{cases} \varrho_{b0}/\left[1 + (\xi/b)^2\right]^{3/2}, & r < (r_b)_{\max} \\ 0, & r > (r_b)_{\max}, \end{cases} \tag{11}$$

where

$$M_b = 4\pi b^3 \varrho_{b0} \times \left\{\ln\left[(r_b)_{\max}/b + \sqrt{1 + ((r_b)_{\max}/b)^2}\right] - \frac{(r_b)_{\max}/b}{\sqrt{1 + ((r_b)_{\max}/b)^2}}\right\} \tag{12}$$

is the mass of the bulge. We have for the gravitational force inside $\xi \le (r_b)_{\max}$

$$\mathbf{F}_b = -\frac{4\pi G b^3 \varrho_{b0}}{\xi^2}\left\{\ln\left(\frac{\xi}{b} + \sqrt{1 + \frac{\xi^2}{b^2}}\right) - \xi/b\sqrt{1 + \xi^2/b^2}\right\}\frac{\mathbf{r}}{\xi}. \tag{13}$$

It is obvious that $\mathbf{F}_b = -GM_b\mathbf{r}/\xi^3$ in the domain $r > (r_b)_{\max}$.

The dynamical model must adequately describe the Newtonian interactions between stars and ensure that the system is collisionless. This is achieved by modifying the gravitational force at small distances by introducing a potential-cutoff radius r_c for any pair of interacting particles i and j. The optimum choice of cutoff radius and number of particles has been discussed many times in the literature (see, e.g., [50–53] and references therein).

Here, we use a Plummer model for the potential:

$$\Phi_{ij} = -G\frac{m_i m_j}{\sqrt{r_{ij}^2 + r_c^2}}, \tag{14}$$

where r_{ij} is the distance between particles and r_c is the cutoff radius. For a fixed number of particles N, it is always possible to choose a cutoff radius r_c that ensures that the model is collisionless. However, the number of particles must be sufficiently large to minimize the error introduced by the modification of the particle-interaction potential at small distances.

We characterize the disk surface density by the scale length L, which determines the exponential law $\sigma(r) = \sigma_0 \exp(-r/L)$. We assumed that the disk surface density is zero in the region $r \ge 5L$ at the beginning of the simulations. We used a system of units in which $G = 1$, $R = 4L = 1$, and the mass of the disk is $M_\mathrm{d} = 1$. We normalized the mass of the halo M_h inside the radius $\xi \le 4L$ to the mass of the disk, $\mu \equiv M_h/M_\mathrm{d}$. In this system of units, one period of rotation of the outer edge of the disk lies in the range $t \sim 3$–4 for $\mu = 1$–4.

Let us now describe the procedure for specifying the initial density distribution in z and the residual velocities of the equilibrium disk.

The vertical structure of the disk is determined by the equations [54]

$$\frac{1}{r}\frac{\partial}{\partial r}\left(r\frac{\partial \Phi}{\partial r}\right) + \frac{\partial^2 \Phi}{\partial z^2} = 4\pi G(\varrho + \varrho_s), \qquad c_z^2\frac{\partial \varrho}{\partial z} = -\frac{\partial \Phi}{\partial z}\varrho, \tag{15}$$

where ϱ and ϱ_s are the spatial density in the disk and spheroidal subsystems, respectively, and c_z is the vertical-velocity dispersion, which is assumed to remain constant with z at the initial time $t = 0$. Eliminating the potential Φ from (15) and introducing the circular velocity

$$V_c(r) \equiv \sqrt{r\left(\frac{\partial \Phi}{\partial r}\right)_{|z=0}}, \tag{16}$$

we can transform the set of partial differential equations to an approximate equation for the disk volume density $\varrho(z)$ in the form of an ordinary differential equation [54]:

$$\varrho\frac{d}{dz}\left(c_z^2\frac{d\varrho}{dz}\right) - c_z^2\left(\frac{d\varrho}{dz}\right)^2 + 4\pi G\varrho^2\left(\varrho + E + \varrho_s(z)\right) = 0, \qquad E = -\frac{1}{4\pi G r}\frac{dV_c^2}{dr}. \tag{17}$$

Together with the conditions $\varrho(z=0)=\varrho_0$, $d\varrho(0)/dz=0$, and $\int\limits_{-\infty}^{\infty}\varrho(z;r)dz=\sigma(r)$, this equation determines the vertical structure of the disk at the radius r for a given surface-density distribution σ. The E term can produce a large error in the estimated density at the disk center, and, in practice, it is assumed that $E(r\to 0)\to 0$. To determine ϱ_0 and $\varrho(z)$ for specified $\varrho_s(z,r)$, $c_z(z,r)$, and $\sigma(r)$, we construct the function $F(\varrho_0)=2\int\limits_0^{\infty}\varrho(z)dz-\sigma$. We solve the equation $F(\varrho_0)=0$ iteratively jointly with numerical integration (17). After determining the density distribution in z, the particles are arranged along the vertical axis on a grid $z_k=k\Delta z$ ($k=-K,\ldots,K$). The kth cell contains particles in proportion to σ_k/σ, where $\sigma_k=\int\limits_{z_{k-1}}^{z_k}\varrho(z)dz$.

Equation (17) is approximate, since it was derived neglecting the dependence of the potential on the vertical coordinate in the first term in (15). Strictly speaking, a disk constructed in this way is not in equilibrium. However, we are interested in initial, unstable states that evolve to new stationary states of the disk. Therefore, the lack of an exact equilibrium in the vertical direction plays the role of a small additional initial perturbation.

The initial velocity distribution is a Schwarzschild function and has the form of an anisotropic Maxwellian distribution:

$$f(u,v,w)=A\exp\left\{-\frac{u^2}{2c_r^2}-\frac{(v-r\Omega)^2}{2c_\varphi^2}-\frac{w^2}{2c_z^2}\right\},$$

where $\{u,v,w\}$ are the velocity components of the particles in cylindrical coordinates.

To obtain the model with the minimum velocity dispersion in the final, stable disk state, we chose a subcritical disk state whose dynamical evolution ensured at the end of the computations both the preservation of an exponential surface-density profile and stability against initial perturbations in the plane of the disk and against bending perturbations (responsible for the increase in the vertical velocity dispersion).

In practice, the initial radial-velocity dispersions c_r in models with low-mass bulges corresponded to Toomre parameters $Q_T\simeq 0.8$–1.1 and $Q_T\simeq 1.2$–2.2 in the central region ($r\lesssim 2L$) and at edge of the disk, respectively. In the case of massive bulges, the models started from higher central values of Q_T. We set the initial vertical-velocity dispersion c_z proportional to c_r. We considered two types of models with different initial disk thicknesses: "thin" disks unstable in the z direction,[2] which had central $(c_z/c_r)_0$ values $(c_z/c_r)_0=(0.4$–$0.5)$ at $t=0$, and "thick" disks with $(c_z/c_r)_0=(0.6$–$0.8)$, which are close to the stability limit against bending perturbations. We assumed that these ratios varied slowly in radius in accordance with an exponential law with a radial scale length appreciably exceeding L. This choice of velocity dispersion ensured weak instability of the disk at all r with the exception of specially stipulated cases, below we describe numerical models of thick disks.

In none of the models did the velocity dispersion c_r remain constant: the disk "heated up" in the course of its evolution.

We found the mean tangential velocity of the model point masses by solving the Jeans equation assuming the absence of systematic radial motions, axial symmetry, and symmetry about the plane $z=0$:

$$V^2=(<v>)^2=V_c^2+c_r^2 \qquad (18)$$
$$\times\left\{1-\frac{c_\varphi^2}{c_r^2}+\frac{r}{\varrho c_r^2}\frac{\partial(\varrho c_r^2)}{\partial r}+\frac{r}{c_r^2}\frac{\partial<uw>}{\partial z}\right\}.$$

Here, $<\ldots>$ denotes averaging of the velocities and the last term in (18) is due to the chaotic components of the radial velocity u and vertical velocity w. When specifying the initial state of the model, we assumed that $<u>=0$ and $<w>=0$ and specified the rotational velocity in accordance with (18). Thus, we have a balance of the radial and vertical forces at the initial time, and the disk begins to evolve from a nearly equilibrium state.

In all the computations, we specified the initial distribution of the velocity dispersion c_φ at $t=0$ in accordance with (3). We verified that the condition $Q_c\equiv\frac{c_r}{c_\varphi}\frac{\varkappa}{2\Omega}=1$ was satisfied as the disk evolved. In models with fairly massive halos ($\mu\gtrsim 2$), the mean deviations at a given r did not exceed 3% over several dozen rotations of the disk edge. This error is partially due to the numerical differentiation performed to compute the epicyclic frequency $\varkappa$. In the models with massive halos, the domain in which $c_r/\varkappa>r$ is small (for $\mu=3$, it has a size of $r\lesssim 0.03$). In the case of $\mu\lesssim 1$, this domain expands to $r\lesssim 0.15$. In addition, the vertical disk scale length increases in such models, and these factors result in stronger deviations from the equality (3). The amplitude of fluctuations $Q_c(t)$ decreases as the number of particles increases and does not exceed 2% in models with $\mu\gtrsim 2$ and $N=2\times 10^5$ (except for the innermost region of the disk,

[2] The bending instabilities of the oscillation mode lead to the heating of a thin disk in the vertical direction and, as a result, to its thickening. As our numerical models show, the axisymmetric bending oscillation mode plays an important role.

$r \lesssim 0.5L$), reflecting the *collisionless* nature of the models constructed.

Using the approach described above, we performed more than 40 numerical simulations of the dynamical evolution of a disk toward a steady state as a function of the initial velocity dispersions $c_r(r)$ and $c_z(r)$. We considered a wide range of parameters for the bulge ($M_b/M_\mathrm{d} = 0$–3, $b/L = 0.02$–0.8) and halo ($M_h/M_\mathrm{d} = 0$–3.5, $a/L = 1$–4). The number of particles was $N = (40$–$500) \times 10^3$ in the TREEcode computations.

We verified the stability of the solutions against our choice of computational method by comparing results for several models obtained using very different methods to compute the gravitational force: the TREEcode method and direct "particle to particle" (PP) integration, in which each particle interacts with each of the other particles, for $N = (20$–$80) \times 10^3$. As an example, Figure 1 shows the time dependence of the radial-velocity dispersions for one of the models computed using these two methods, with similar initial conditions.[3] A comparison of the two results reveals no significant differences between the final disk states.

5. DETERMINING THE THRESHOLD Q_T VALUES

5.1. Disk Heating Mechanism

An initially axisymmetric, equilibrium disk is heated, increasing its velocity dispersion with time. The question of greatest importance for dynamical simulations is the heating mechanism. To correctly describe the processes in stellar disks, it is important, in particular, to ensure that the heating is not due to the collisional relaxation of the particles, whose number N is many orders of magnitude smaller than the number of stars in real systems. This is achieved via appropriate choices of the number of particles and the cutoff radius. Our criterion for the absence of significant collisional-relaxation effects is that the character of the system's evolution be preserved when the computations are performed for an increased number of particles, as we verified for many models.[4]

Below, we summarize the most important features of the disk heating shown by the numerical simulations.

(1) The disk-heating time is much greater than the mean rotation period of the particles (Fig. 2a). In the initial stage ($t \lesssim 1$), c_r remains virtually constant, as long as the disk remains axisymmetric. In the case of a low-mass or nonexistent halo, the evolution of the disk is determined by the bar mode, and the disk is heated due to the formation of an nonaxisymmetric bar and associated two-armed spiral. Models with sufficiently massive halos show no enhancement of the bar mode but develop a complex transient system of small-scale spiral waves (Fig. 2b). The decrease of the amplitudes of these waves with time is accompanied by a transfer of rotational kinetic energy to the chaotic component of the velocity, resulting in heating of the disk.

(2) The heating of an initially cool disk ($0.5 \lesssim Q_T \lesssim 1$) begins in its central region (Figs. 2a, 2b). The heating at the periphery proceeds much more slowly. The velocity dispersion at the periphery usually begins to rise when the center has already reached a quasi-stationary state (Fig. 2a). At the same time, the processes at the center and at the periphery are interrelated: rapid instability in the central region can speed up the heating of the outer part of the disk, while stability of the central region can slow down this process.

(3) If the system does not develop a bar, the amplitude of the perturbations begins to decrease with increasing velocity dispersion. In turn, the increase of the radial-velocity dispersion c_r slows with decreasing wave amplitude. The heating virtually ceases after the decay of the transient spiral waves (Figs. 2a, 2b). The integrated amplitude of the Fourier harmonics

$$\hat{A}(m;t) = \sqrt{\sum_p A^2(m,p,t)},$$

$$A(m,p,t) = \frac{1}{N}\sum_{j=1}^{N} \exp\{i\,[m\varphi_j(t) + p\ln(r_j(t))]\}$$

decreases with time for all mode numbers m, but most slowly for $m = 2$ (Fig. 2c). The density distribution in the disk becomes almost axisymmetric (if the mass of the spherical components is large enough to prevent the development of a bar), and, on the whole, the velocity dispersion c_r maintains its level over several

[3] The velocity-dispersion components in the plane of the disk c_r and c_φ increase rapidly during the initial stage ($t < 10$) of the heating of an initially cool disk with initial Toomre parameter $Q_T(r < 2L) \simeq 0.85$. The relaxation of the disk in the vertical direction is appreciably slower, so that small local decreases of c_r are possible when the disk is heated in z and there are radial motions (see curve *1* in Fig. 7 after $t > 7$).

[4] The minimum number of particles N_crit for which this criterion is satisfied to sufficient accuracy (i.e., to within random fluctuations of the estimates of the final parameters) depends, in particular, on the form of the rotation curve. The number N_crit is larger for highly concentrated nuclei (bulges), due to the higher rotational angular-velocity gradient in the central region of the disk. In the limiting case of a very short, rigidly rotating region, N_crit can reach 3×10^6 [20]. Our simulations showed that, if the rotation curve grows monotonically to $r \simeq 2L$, then N_crit can be set equal to $\simeq 4 \times 10^4$.

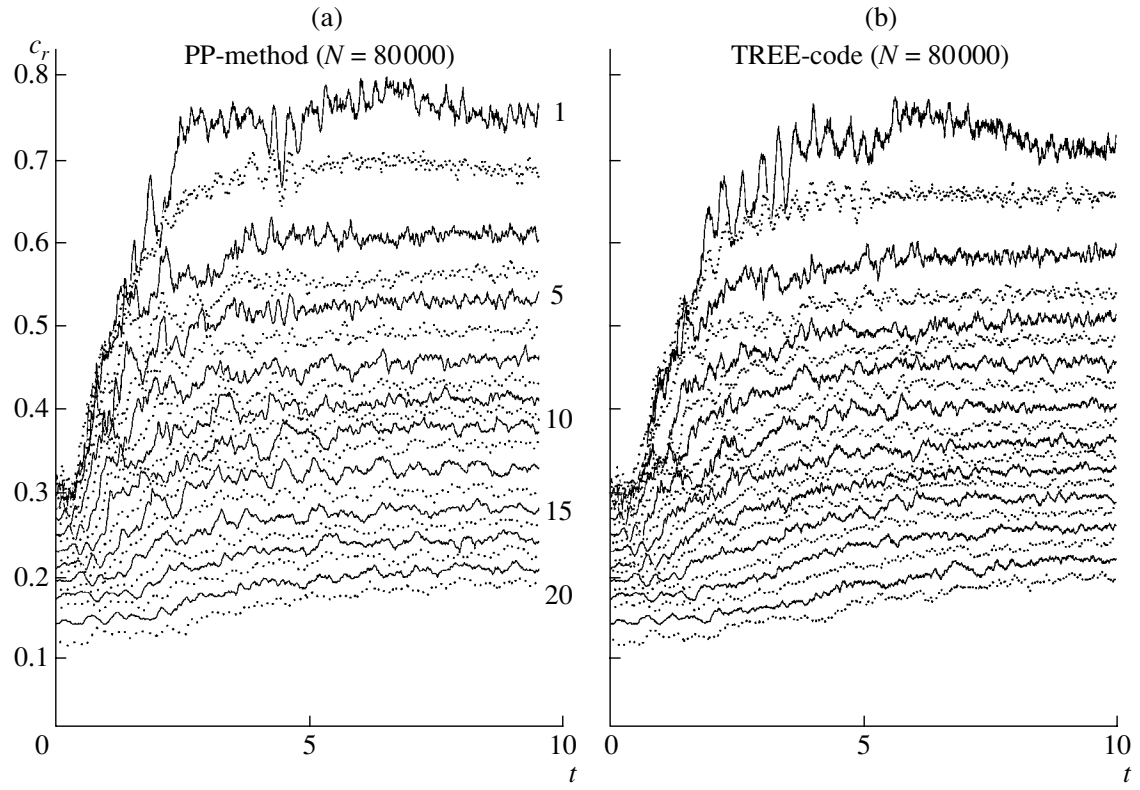

Fig. 1. Time dependence of the radial-velocity dispersion $c_r(r)$ for particles at 20 different galactocentric distances (1 is the central zone, and each zone has a width of $0.05R$) at the initial stage of heating of a cool, thin disk ($t = 10$ corresponds to ~ 3 rotations of the outer edge of the disk) for two methods of computing the gravitational force with $N = 80\,000$: (a) the PP algorithm and (b) the TREE-code algorithm.

dozen rotations, provided that relaxation processes have ceased in the vertical direction.

(4) Whereas three- and even four-armed modes can dominate at the initial stage of evolution of an initially cool disk ($Q_T(r \lesssim 2L) < 1$; Figs. 2b, 2c), the spiral pattern changes if we choose a subcritical initial state (i.e., a state that is unstable, but not so cool that $Q_T \gtrsim 1$). The spatial structure of the perturbations depends to a considerable degree on the relative mass of the spheroidal subsystem. Figure 3 shows the distributions of the logarithm of the disk surface density at various times. The two-armed mode is dominant in this model, although the $m = 3$ harmonic is also important, especially in initial stages of the evolution. It is typical for the spirals to join in the outer region of the disk to form a ring-shaped structure.

(5) Models with low-mass spheroidal subsystems starting from a very cool initial state undergo a substantial mass redistribution in the disk, accompanied by a change in the form of the rotation curve $V(r)$ in the process of heating and formation of a bar. In this case, the final distribution of the surface density $\sigma(r)$ differs strongly from an exponential law (Fig. 4).[5]

Another feature of model disks starting from a very cool initial state ($Q_T \lesssim 1$) is that the velocity dispersion at the end of the computations (after 10–15 rotations) is somewhat higher than is required for gravitational stability. This is due to heating by collective processes—high-amplitude wave motions that develop in the presence of strong instability. When the disk is heated and reaches marginal stability, these perturbations die out, but the wave-decay process has a certain inertia: the velocity dispersion is already high enough to maintain the stability of the disk, but the spiral waves have not yet decayed (as is confirmed by Fourier analysis of the density perturbations in the disk) and continue to heat the disk. Therefore, to obtain the minimum velocity dispersion required for

[5]It is possible, in principle, to choose an initial density profile that yields an exponential profile at the end of the computations (dashed line in Fig. 4); however, this approach is artificial. It seems that the stellar disks of most of the galaxies do not pass through a stage of strong dynamical instability.

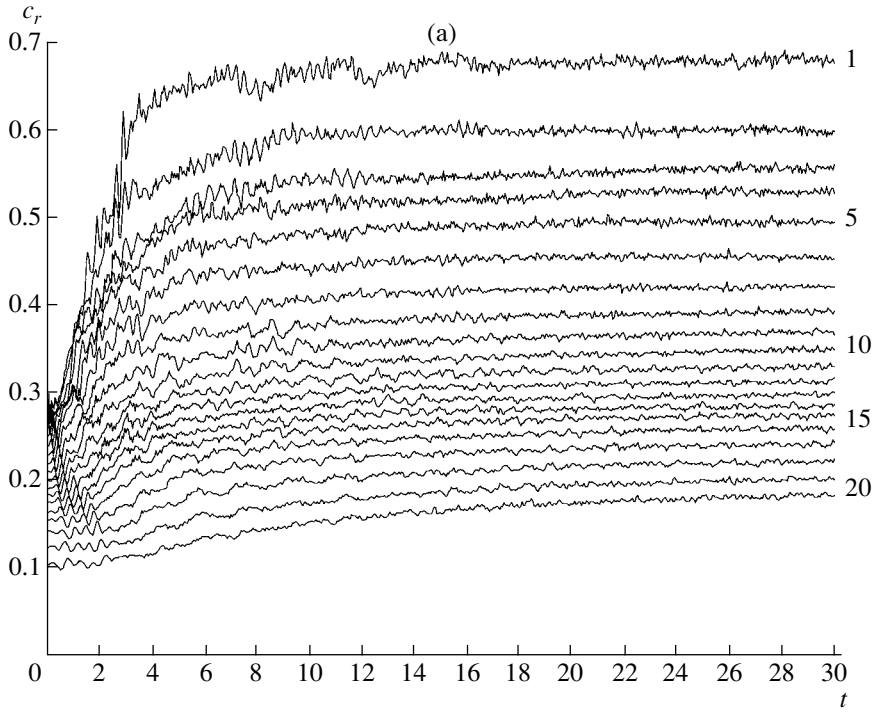

Fig. 2. Evolution of an initially unstable thin disk ($\mu = 3$, $a = L$). (a) Time dependence of the radial-velocity dispersion in 20 radial zones. (b) Development of a system of transient spiral waves in an initially axisymmetric disk. Shown are the positions of point masses in the (x, y) plane at various times (since the model consists of 5×10^5 particles, only some of the point masses are shown). (c) Time dependence of the integrated amplitudes $\hat{A}(m)$ of the Fourier harmonics for various modes $m = 2, ..., 6$. The parameters $\hat{A}$ reach their maximum values in the interval $1 \lesssim t \lesssim 4$, and it is in this time interval that the perturbations reach their maximum amplitudes (Fig. 1b). After $t > 4$, $\hat{A}$ decreases, corresponding to the beginning of wave dissipation and a slowing of the increase in the dispersion c_r (Fig. 2a).

disk stability, we used an iterative algorithm to make the initial velocity dispersion approach the stability limit.

Our *iterative approach* is based on a series of several (two to four) consecutive computations, each of which starts with an initial dispersion that is somewhat closer to the critical level than that for the previous computation. For each radius r, we chose an initial velocity dispersion that was intermediate between the initial and final values (after five to ten rotations) in the previous computation.

As expected, the stability limit also depends on the initial disk thickness.[6] If the disk is initially thick (with a vertical scale height $h_z \gtrsim 0.2L$) and unstable only in its plane ($c_r < c_r^{\rm crit}$), its heating proceeds more slowly and ceases at lower radial-velocity dispersions than in the case of an initially thin disk. This is due to two factors: the stabilizing effect of the finite thickness of the disk and the slowness of the relaxation in the vertical direction compared to the heating in the plane of the disk.

The results of dynamical simulations can be used to determine the disk parameters at the gravitational-stability limit (when the velocity dispersion ceases to change, after 5–20 rotations of the outer edge of the disk).

5.2. Gravitational-Stability Threshold for Bulgeless Models

We computed a series of bulgeless galaxy models, differing in the relative mass $\mu = M_h/M_{\rm d}$ and the halo scale length a, with a fixed radial disk scale L.

When $a \gtrsim L$, the rotation curve has an extended section $V_c(r)$ (which we will call the "rigid-rotation" section), which makes a transition to a plateau $V_c \simeq const$ at $r \gtrsim 2L$ (curve *1* in Fig. 5a). Figure 5a

[6] The initial thicknesses of the disks of real galaxies depend on the conditions under which they were formed. For example, if the collapse of a gaseous disk involved violent star formation before it reached a quasi-stationary state, the resulting stellar disk may be much thicker and have a higher velocity dispersion c_z than the minimum value required for stability. However, such a scenario is difficult to reconcile with the existence of very thin ($h_z/L < 0.2$) stellar disks in edge-on galaxies. The dependence of the disk thickness on the relative mass of the halo is also consistent with the assumption that the stellar-velocity dispersion is close to the value expected for marginal stability [7].

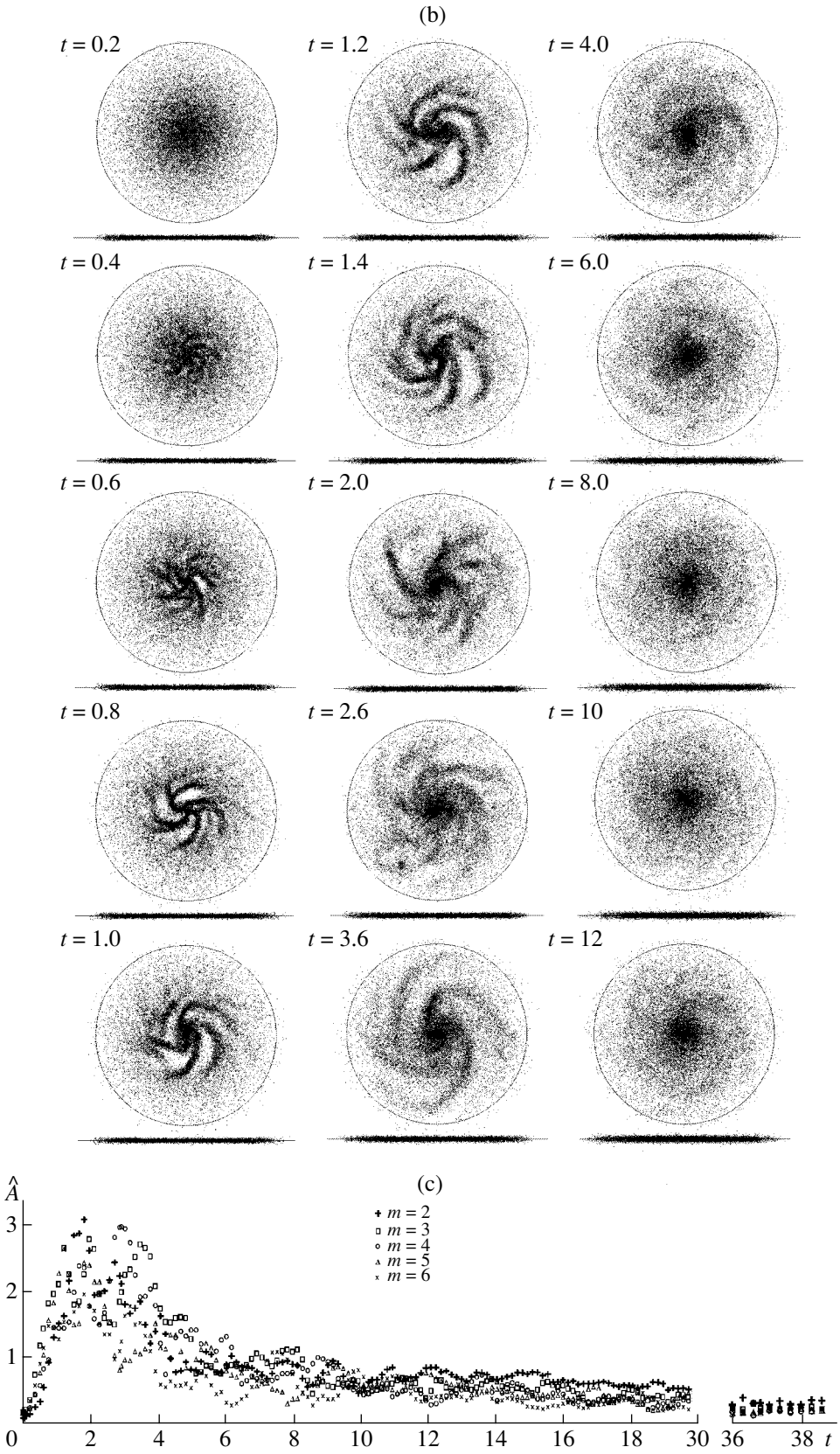
(b)
t = 0.2
t = 1.2
t = 4.0
t = 0.4
t = 1.4
t = 6.0
t = 0.6
t = 2.0
t = 8.0
t = 0.8
t = 2.6
t = 10
t = 1.0
t = 3.6
t = 12
(c)
Â
m = 2
m = 3
m = 4
m = 5
m = 6
0 2 4 6 8 10 12 14 16 18 30 36 38 t

Fig. 2. (Contd.)

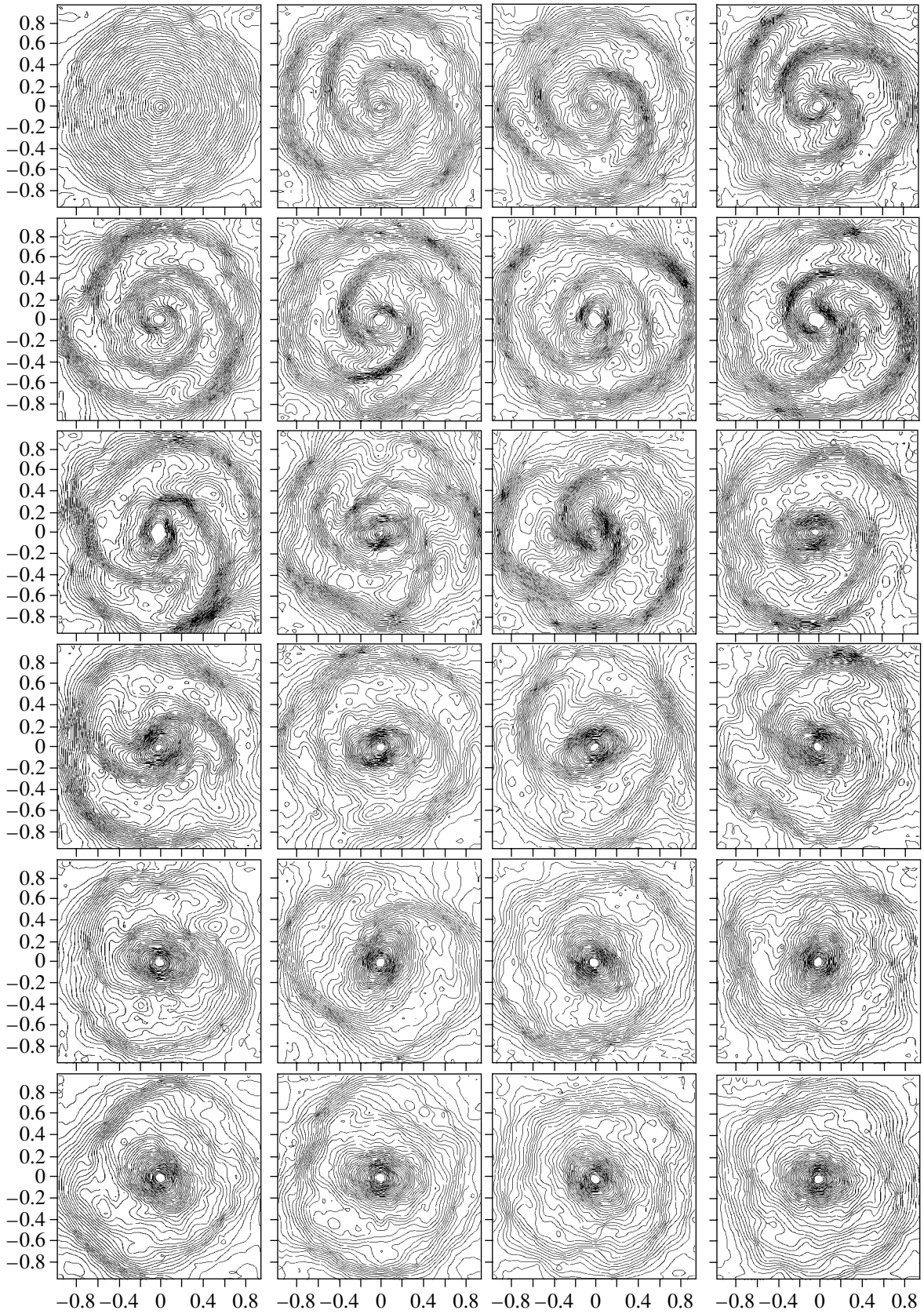

Fig. 3. Distribution of the logarithmic surface density $\log \sigma$ at various times from $t = 1$ to $t = 30$ for the initial subcritical state with $Q_T \gtrsim 1$.

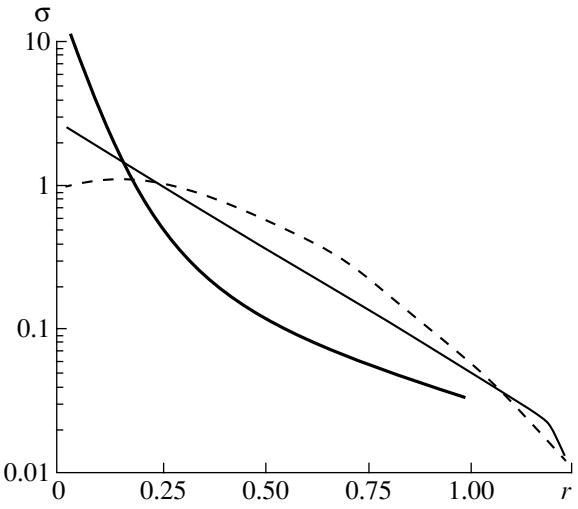

Fig. 4. Radial dependences of the surface density for an initially cool model disk in which there is subsequently a substantial density redistribution. The thin solid curve shows an exponential profile, the bold solid curve the final profile averaged in azimuth after strong heating and development of a bar, and the dashed curve the initial profile that produces a quasi-exponential distribution at the end of the computations.

shows for a bulgeless galaxy with $\mu = 1$ the radial distributions of the circular rotational velocity $V_c(r)$ (curve *1*), mean particle rotational velocity $V(r)$ (curve *2*), radial-velocity dispersion $c_r(r)$ (curve *3*), and the differential-rotation parameters $S = 2\Omega/\varkappa$ computed separately for $V_c(r)$ and $V(r)$ (4 and 5).

Knowing the final velocity dispersions, disk density, and rotational velocity, it is possible to compare the Toomre stability parameters Q_T (1) for the corresponding model with the analytically derived local criteria discussed above and compare these criteria with each other. Note that the analytical criteria were derived assuming that the circular rotational velocity $V_c(r)$ differs little from the mean velocity $V(r)$ of the gravitating point masses. However, the difference between these velocities can be quite significant for collisionless disks. We therefore determined the stability parameters for both $V_c(r)$ and $V(r)$.

Figure 5b shows for this model the computed Q_T and the Toomre parameters required for marginal stability according to the criteria of Polyachenko, Polyachenko, and Strel'nikov (PPS) $Q_T^{(P)}$ (6) and Morozov $Q_T^{(M)}$ (5) calculated separately using the circular velocity and the mean rotational velocity of the particles. In the case of a massive halo ($\mu \gtrsim 2$), the difference between the stability parameters for $V_c(r)$ and $V(r)$ is small, but it can become appreciable for $\mu \lesssim 1$ (Figs. 5a, 5b). This is due to the fact that the difference $V_c - V$ increases with increasing velocity dispersion in accordance with (18).

The condition $S \simeq Q_T^{(M)} \lesssim Q_T \lesssim Q_T^{(P)}$ is satisfied both in the case considered here and for most of the models (recall that $Q_T = S$ is the Toomre condition for marginal stability with crude allowance for nonaxisymmetric perturbations; see Section 2).

Figures 5c and 5d compare the stability criteria in a different way. These figures show the radial dependences of the ratio of the model velocity dispersion c_r of the disk when it becomes stable to the critical velocity dispersion for the various criteria considered in Section 2. The ratio $c_r/c_{\rm crit} = 1$ corresponds to full agreement with the model dependences.

Although none of the criteria explain the model dependences $Q_T(r)$ at all r, the closest results are given by the PPS criterion generalized for the case of finite thickness (2) and the Morozov criterion (5) (symbols *15* and *16* in Fig. 5c). When the stability criteria are determined in terms of the mean rotational velocity (Fig. 5b), the radial variations of $c_r/c_{\rm crit}$ maintain their form (Fig. 5d), and the ratio $c_r/c_{\rm crit}$ is closest to unity in the interval $0.1 < r < 0.8$ for the Morozov criterion (curve *16*). It is striking that the PPS criterion (curve *12*) overestimates $c_{\rm crit}$ in all cases, but $c_r/c_{\rm crit}$ remains nearly constant over a wide range of r, enabling easy introduction of a correction factor for $c_{\rm crit}$.

One important result is that the radial dependence of the Toomre parameter $Q_T(r)$ computed for the circular velocity $V_c(r)$ shows qualitatively similar behavior for all the bulgeless models we considered (Fig. 5e). Moreover, $Q_T(r)$ remains approximately constant at the level $Q_T \simeq 1.2$–1.6 in the interval $0 \lesssim r/L \lesssim 2$ (see Fig. 5e). At the disk periphery ($r \gtrsim 2L$), Q_T increases with radius, reaching $Q_T \simeq 2.5$–3 at the edge of the disk ($r \simeq 4L$). However, the scatter of the Q_T values for the various models is small, enabling us to adopt the following function as a lower envelope

$$Q_T^{(*)} = A_0 + A_1 \times \left(\frac{r}{L}\right) + A_2 \times \left(\frac{r}{L}\right)^2, \qquad (19)$$

where $A_0 = 1.25$, $A_1 = -0.19$, and $A_2 = 0.134$ (bold curve in Fig. 5e). This function reaches its minimum, equal to 1.2, at $r/L = 0.7$.

The observational estimates of the stellar-velocity dispersions are usually based on data for the inner region of the disk $r < 2L$. Therefore, the approximate constancy of Q_T in this region makes this quantity a convenient tool for estimating the surface density and mass $M_{\rm d}$ of a disk (assuming it is stable) based on the known rotation curve of the galaxy and the radial

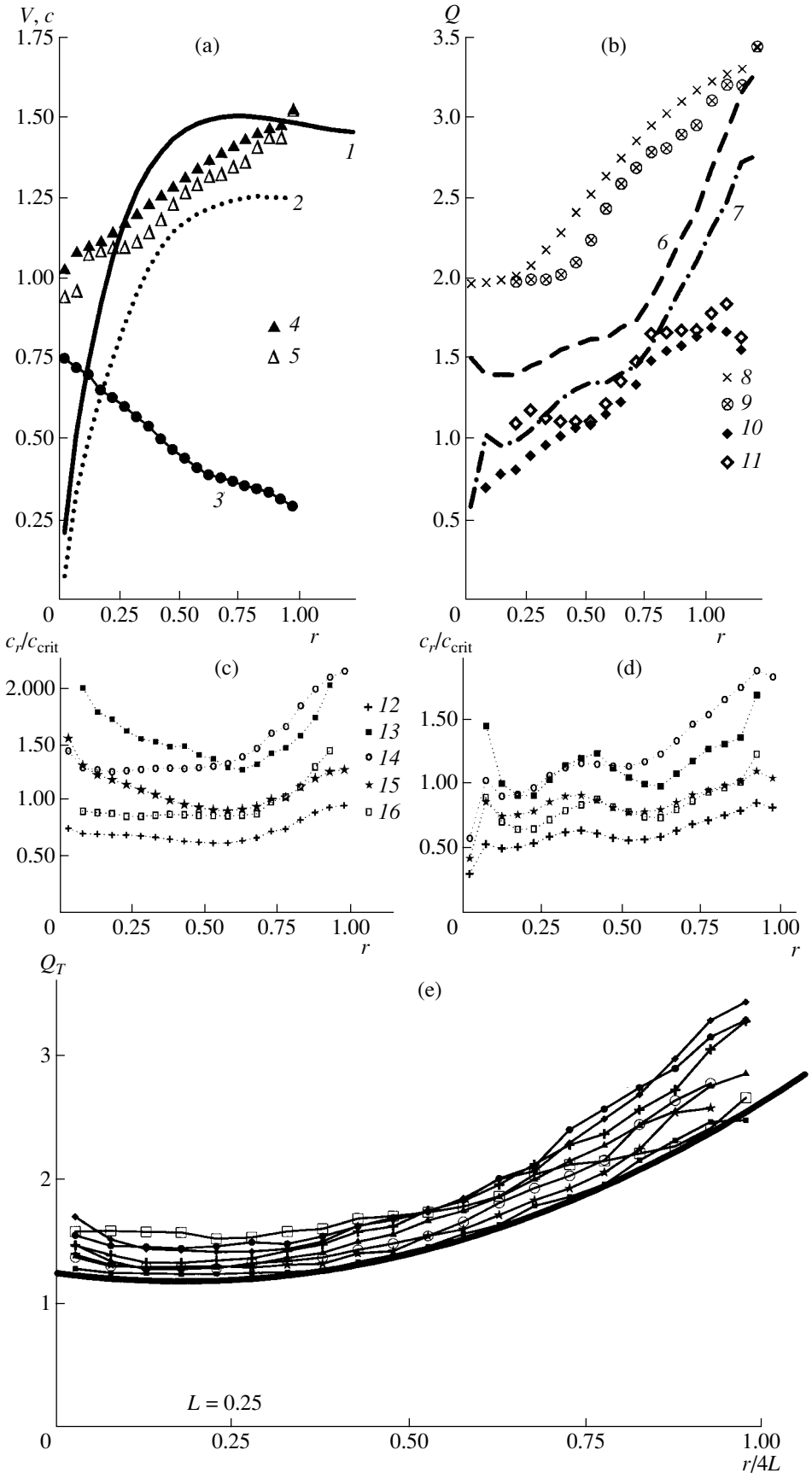
V, c
(a)
1
2
3
4
5
r
Q
(b)
6
7
8
9
10
11
r
c_r/c_{crit}
(c)
12
13
14
15
16
r
c_r/c_{crit}
(d)
r
Q_T
(e)
L = 0.25
r/4L

Fig. 5. Parameters of a disk that has evolved to a stable state at the stability limit, for bulgeless models. (a) Radial dependences of the circular velocity $V_c(r)$ (curve *1*), disk rotational velocity $V(r)$ (curve *2*), radial-velocity dispersion $c_r(r)$ (curve *3*), and parameters $S = 2\Omega/\varkappa$ computed for the circular velocity (curve *4*) and disk rotational velocity (curve *5*), respectively. Results are shown for a model in which the mass of the halo within $r \leq 1 = 4L$ is equal to that of the disk and the halo scale length a is equal to the radial disk scale length L. (b) Radial dependences of the Toomre parameter at the stability limit computed using various stability criteria for the model shown in Fig. 5a: *6* Q_T determined from V_c, *7* Q_T determined from V, *8* $Q_T^{(P)}$ determined from V_c, *9* $Q_T^{(P)}$ determined from V, *10* $Q_T^{(M)}$ determined from V_c, and *11* $Q_T^{(M)}$ determined from V. (c) Radial distributions of the ratio $c_r/c_{\rm crit}$ of the radial-velocity dispersions in the numerical models (curve *3* in Fig. 5a) to the critical values computed using the circular rotational velocity $V_c(r)$ (curve *1* in Fig. 5a) for *12* the Polyachenko–Polyachenko–Strel'nikov criterion (6) and *13* the Morozov criterion (5). Also shown are *14* $c_r/(c_T 2\Omega/\varkappa)$ derived using the simplified criterion (4); *15* c_r normalized to $c^{(P)}Q_T^{(1)}$, which is a generalization of criterion (6) for the case of a finite-thickness disk, derived using (2); and *16* the ratio obtained for the Morozov criterion (5) in the case of an infinitely thin disk ($D = 1$). (d) Same as Fig. 5c using the disk rotational velocity $V(r)$ (see curve *2* in Fig. 5a). (e) The Toomre parameter $Q_T(r)$ at the stability limit for a series of bulgeless models with various halo parameters. The bold thick curve is computed using (19).

exponential disk scale L. The equation relating these quantities is

$$c_r = Q_T^{(*)}(r)\frac{3.36G\sigma_0\exp(-r/L)}{\varkappa}, \qquad (20)$$

where $Q_T^{(*)}$ for galaxies with extended intervals of increasing $V_c(r)$ is determined by (19). In turn, the disk mass estimate $M_{\rm d} = 2\pi\sigma_0 L^2$ makes it possible to separate out the mass of the dark halo within a specified radius.

5.3. Models with Formation of a Bulge

In the case of a low-mass or very "loose" halo and no bulge, the evolution of an initially cool dynamical model inevitably results in the development of a bar. As a rule, the formation of a bar involves an appreciable radial redistribution of the mass, whose intensity increases when the velocity dispersion in the initial state decreases. The outer boundary of the disk shifts outward. As a result, the radial scale for the azimuthally averaged surface density $L = -(d\ln\sigma/dr)^{-1}$ varies, which can lead to deviations from an exponential profile ($L = $ const throughout the disk). In the innermost region ($r \lesssim 0.3L$), the surface density can increase appreciably over its initial value (Fig. 4), bringing about a decrease of Q_T in accordance with (1). A similar conclusion concerning the increase in the central density during the formation of a bar was also reached for models with "living" (evolving) halos [55]. Numerical simulations have shown that, under certain conditions, the interaction between the bar and "living" halo can appreciably affect the dynamical evolution of the bar [56].

The stability conditions considered above were derived for and applied to axisymmetric disks. However, it is of interest to formally compute these criteria based on azimuthally averaged parameters in the absence of axial symmetry in the inner region—for example, for barred galaxies. As an example, Figure 6 shows the radial distributions of the parameters of a disk that has developed a bar (Figs. 6a–6c show results for a model with a low-mass halo and Figs. 6d–6f results for a model with a halo whose initial mass within $r = 4L$ is twice that of the disk). The radial distributions of the surface density in the bar region can differ from those outside the bar (Figs. 6c, 6f). The development of a bar usually results in additional thickening of the disk. The function $Q_T(r)$ depends on the bar parameters (essentially, on the initial conditions), but the condition $Q_T \gtrsim 1.5$ is satisfied when $r \gtrsim L$, and the radial dependence $Q_T(r)$ is qualitatively similar to that observed for an axisymmetric disk. Other conditions being the same, the development of a bar in models with more massive halos is accompanied by weaker deviations from the initial exponential surface-density profile (Fig. 6f).

The characteristic dependences for the model with a massive halo (Figs. 6d–6f) differ little from the cases shown in Fig. 5 for barless models. As expected, suppressing the bar mode requires a higher initial velocity dispersion c_r or a more massive halo, in accordance with classical concepts (see, e.g., [29, 44]).

5.4. Models with Bulges

Let us consider now model galaxies whose rotation curves in the central region ($r \lesssim L$) are determined primarily by the bulge. As a rule, the rotations curves outside the bulge ($r \gtrsim L$) are almost flat $V \simeq$ const. Figure 7 shows typical model radial dependences of the disk parameters for this case. In the presence of a bulge, Q_T increases strongly in the central region of the disk, where the dynamics are determined by the bulge potential (Figs. 7b, 7e). However, outside this region, at $r \simeq (1–2) \times L$, the radial dependence of Q_T retains its form [see (19), Fig. 5e]. Q_T increases monotonically with r to values 2.5–3.5. The resulting radial dependence of Q_T is typical of systems with bulges that are not too

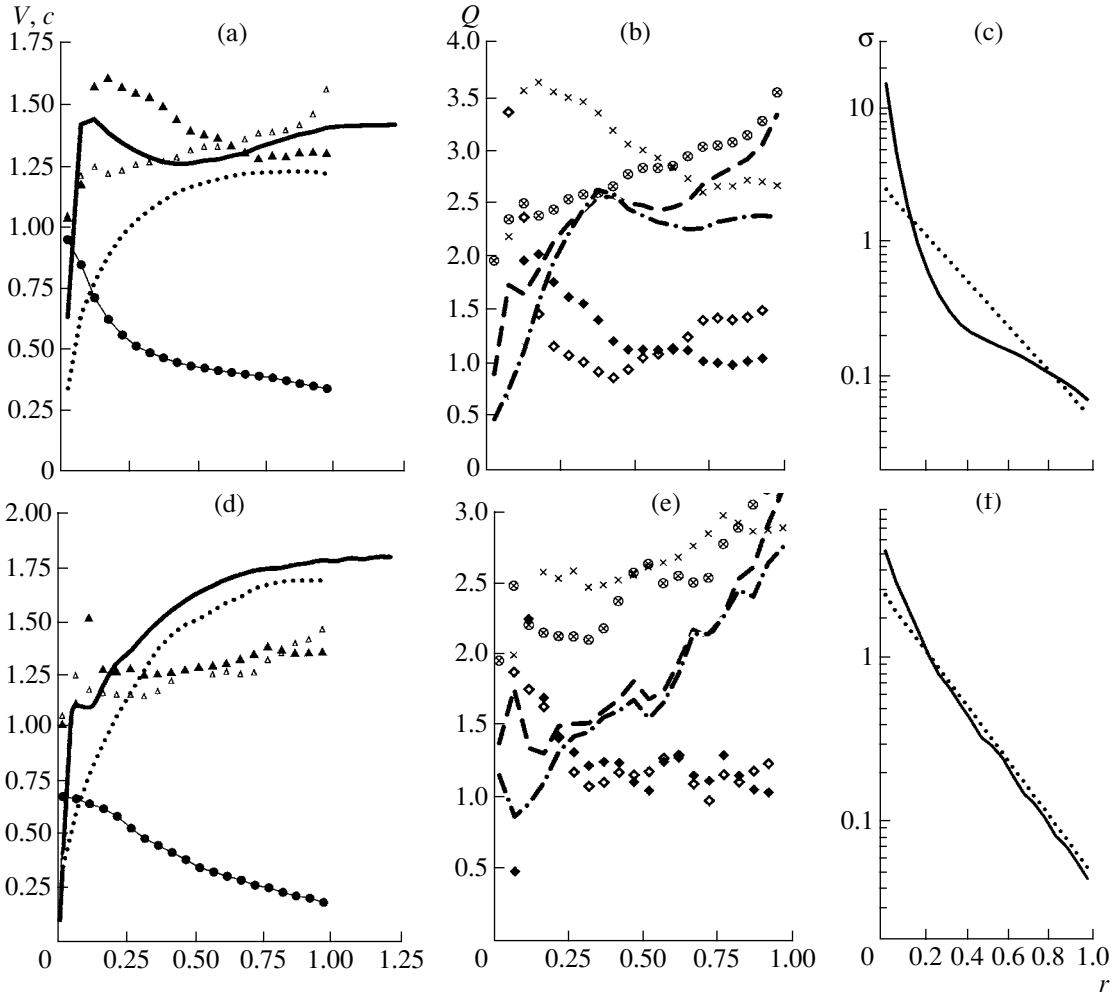

Fig. 6. Bulgeless models that develop bars in the course of their evolution. (a)–(c) $M_h = 0.7M_\mathrm{d}$, and $a = 2L$; (d)–(f) $M_h = 2M_\mathrm{d}$ and $a = 1.6L$. Same notation as in Fig. 5. Plots (c) and (f) show azimuthally averaged surface-density profiles at the initial time (dashed) and after the development of a quasi-stationary state with a bar at $t \geq 25$ (solid).

massive ($M_b/M_\mathrm{d} \lesssim 0.3$) and not very extended ($(r_b)_\mathrm{max} \lesssim L$).

The more massive and more compact the bulge, the higher the value of Q_T at the disk center. This increase of the Toomre parameter is due mainly to the increase of the epicyclic frequency $\varkappa$. The radial-velocity dispersion in the central region also increases somewhat with increasing mass of a strongly concentrated bulge. Additional heating of the center of the disk subsystem ($r \lesssim 0.5L$) in the model shown in Fig. 7a has no direct bearing on gravitational instability. At the initial stage of its evolution, the model with $\mu = 1$ develops a bar, which disrupts with time as a result of scattering of particles passing near the concentrated nucleus, which has a scale length of $b = 0.01$. This mechanism for bar disruption is similar to the effect produced by a black hole [57].

As a result, the disk undergoes additional heating and becomes thicker in the central region (Fig. 7f). The degree of additional heating and the circular velocity V_c at the disk center are very sensitive to the bulge parameters, first and foremost, the core radius b (in particular, the bar disruption described above does not take place if $b \gtrsim 0.05L$). Therefore, the Toomre parameter Q_T can vary very strongly in different models at distances $r \lesssim 0.5L$ (Fig. 7f).

5.5. Differential Rotation as a Factor Increasing the Threshold for Gravitational Stability

Consider two limiting cases: a disk that rotates almost rigidly and a quasi-Keplerian disk whose rotational velocity decreases as $V \propto r^{-1/2}$. Since differential rotation is a destabilizing factor, rigidly rotating disks are expected to have lower Q_T, other conditions being the same.

Galaxies usually exhibit an extended interval of almost rigid rotation if the mass of the disk dominates throughout most of the disk ($r \lesssim 2L$), so that

suppression of the bar instability requires stronger disk heating than in the presence of massive spherical components. Therefore, to elucidate the role of differential rotation, we analyzed a model in which the development of a bar is suppressed by a massive halo and the outer part of the disk ($r \gtrsim L$) contains a rigidly rotating section. The differential-rotation parameter in this model $S(r > L) = 2\Omega/\varkappa = 1.1$–$1.2$ is close to $S = 1$, which corresponds to completely rigid rotation (Fig. 8a). Figure 8a shows the radial dependences of Q_T, $Q_T^{(P)}$, $Q_T^{(M)}$, and S characterizing the stability of the system. It is clear that, on the whole, the disk is stable at lower values of Q_T (curve 6) than in the cases considered above. We have $Q_T \simeq 1$ and $Q_T \simeq 2$ at the disk center and periphery, respectively.

Consider now another limiting case, corresponding to a nearly Keplerian rotation curve (Fig. 8b). Such behavior is very rarely seen in the rotation curves of real galaxies, but we are interested in the fundamental question of how strong differential rotation affects the minimum velocity dispersion required for stability. To produce quasi-Keplerian disks, we introduced massive concentrated components into our dynamical model. The resulting series of models is a natural extension of those with very massive bulges ($M_b > (2$–$4)M_\mathrm{d}$). Figure 8b shows the results obtained for such models. The Toomre parameter increases appreciably for disks with strong differential rotation, so that the condition $Q_T > 2$ must be met for stability, even in the region where Q_T reaches its minimum ($r \simeq (1$–$2)L$).

Since the central region is dominated by the spheroidal system, no bar develops, and the increase in the velocity dispersion pointed out in Section 5.4 does not arise (Fig. 7a).

6. DISCUSSION AND CONCLUSIONS

We have carrid out numerical simulations of the evolution of disks that are initially unstable, collisionless, and in equilibrium for a whole series of three-dimensional models. The aim of our analysis was to compare the minimum radial-velocity dispersions c_r at which the disks reach their final, quasi-stationary state (as a rule, after 5–10 rotations of the outer edge of the disk) with the velocity dispersion $c_T = 3.36\pi G\sigma/\varkappa$ required to suppress gravitational instability of a thin disk against axially symmetrical perturbations (the Toomre criterion), as well as with other local stability criteria. We separately analyzed the influence of the bulge, dark halo, differential rotation, and initial disk parameters on the radial behavior of $Q_T = c_r/c_T$.

Our numerical simulations show that differential rotation and inhomogeneity of the disk, the action of global perturbations, and the finite thickness of the disk can change the local velocity dispersions (or the local Toomre parameters) of marginally stable disks by $\gtrsim 50\%$. The numerical models enable a separate analysis of the effects of each of these factors.

The models considered here clearly demonstrate rapid heating of initially unstable disks during the formation and disruption of transient spiral arms. The low-contrast "remnants" of these arms can be traced over more than ten rotations. A similar pattern of disk evolution was obtained for models with different numbers of particles and derived using a different (PP) computational algorithm.

As expected, the minimum radial-velocity dispersion at the end of the simulations (in units of the circular velocity) is higher the lower the relative mass of the halo, the smaller the initial disk thickness, and the higher the degree of differential disk rotation. Although the radial dependence of Q_T differs for different models and is determined primarily by the relative mass and degree of concentration of the spherical components, in all cases, $Q_T(r)$ passes through a minimum $Q_T \simeq 1.2$–1.6 at a galactocentric distance of $(1$–$2)L$, and this behavior depends only slightly on the choice of model. This fact can be used to approximately estimate the density (and, consequently, the mass) of a galactic disk (or place limits on these quantities) from observed radial-velocity dispersions using formulas (19) and (20) without the use of numerical simulations or analytical stability criteria. If the halo is not too massive ($M_h/M_\mathrm{d} \lesssim 2$), a disk that begins its evolution from a strongly unstable state rather than a subcritical state can experience a substantial mass redistribution over one or two rotations. The fact that galaxies usually have exponential brightness distributions indicates that the formation of stellar disks, apparently, was not accompanied by the development of strong gravitational instability.

The thicker is initially the disk, the lower is the minimum radial velocity dispersion c_r, which determines its stability. Therefore, the minimum critical dispersions in both coordinates z and r are reached if the disk begins to evolve from a subcritical state, both for gravitational perturbations in the plane and for bending perturbations (global, primarily axisymmetric mode, and small-scale ones).

The disk evolution traced by the numerical models clearly demonstrates the interrelations of processes at different r. Initial stability of the central disk region slows while strong initial instability accelerates the increase of the velocity dispersion at the disk periphery, having, however, no significant effect on the final state.

Existing analytical criteria for the stability of thin disks are based on other considerations, and, strictly

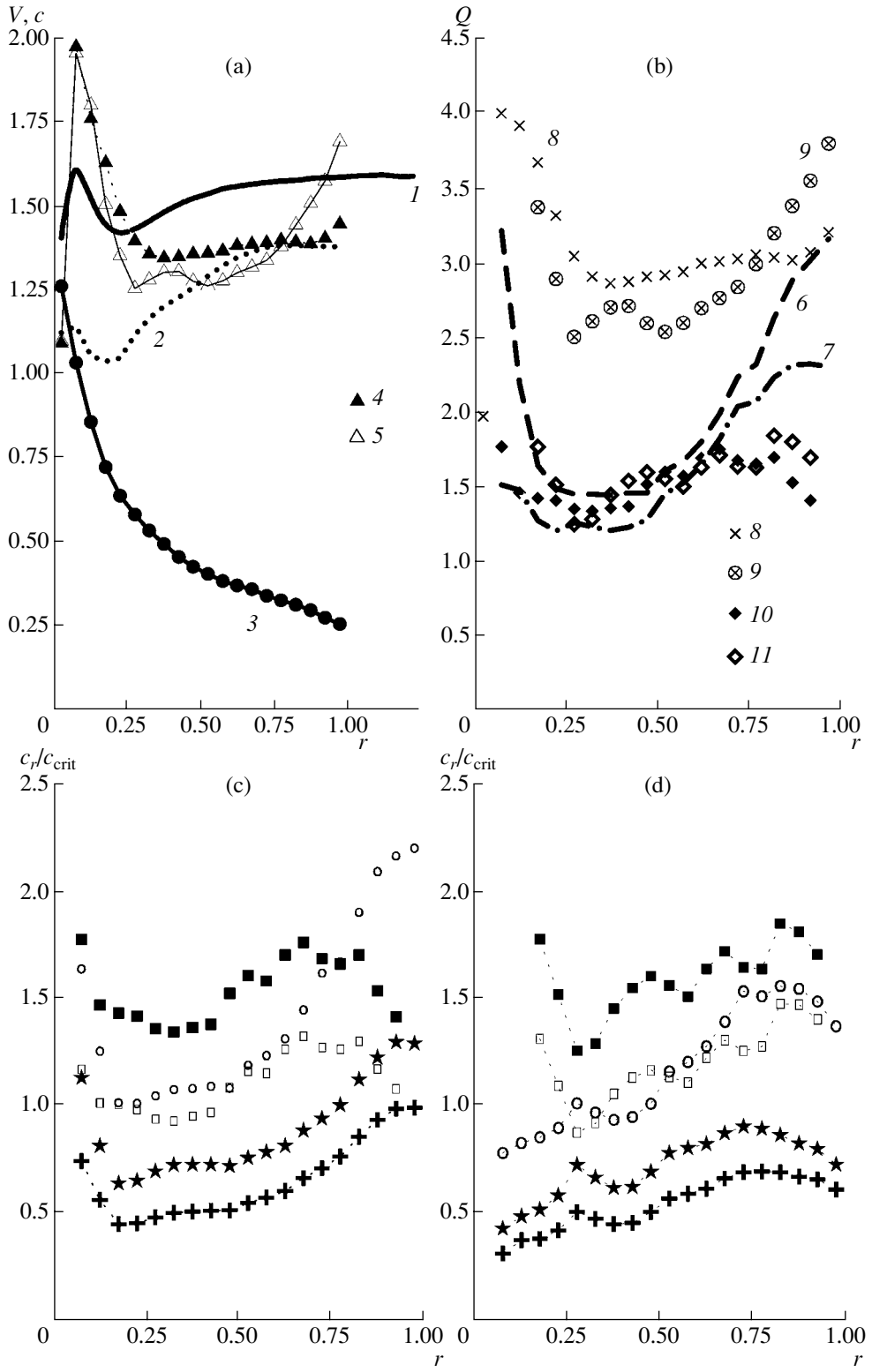

Fig. 7. Disk parameters at the stability limit for models with bulges. (a)–(d) Radial dependences of the disk parameters (same notation as in Fig. 5). The mass of the halo within $r \leq 1 = 4L$ is equal to that of the disk, and the halo scale length is $a = 3.6L$. The bulge parameters are $M_b = 0.24M_d$, $b = 0.04L$, and $(r_b)_{max} = 0.5L$. (e) Toomre parameter $Q_T(r)$ computed using $V_c(r)$ at the stability limit for the series of models with bulges. The bold solid curve is based on (19). (f) Edge-on view of the disk at the end of the computation of the model shown in a. The dots show the positions of the particles. The model develops an appreciable bulge-like feature in the central region of the disk.

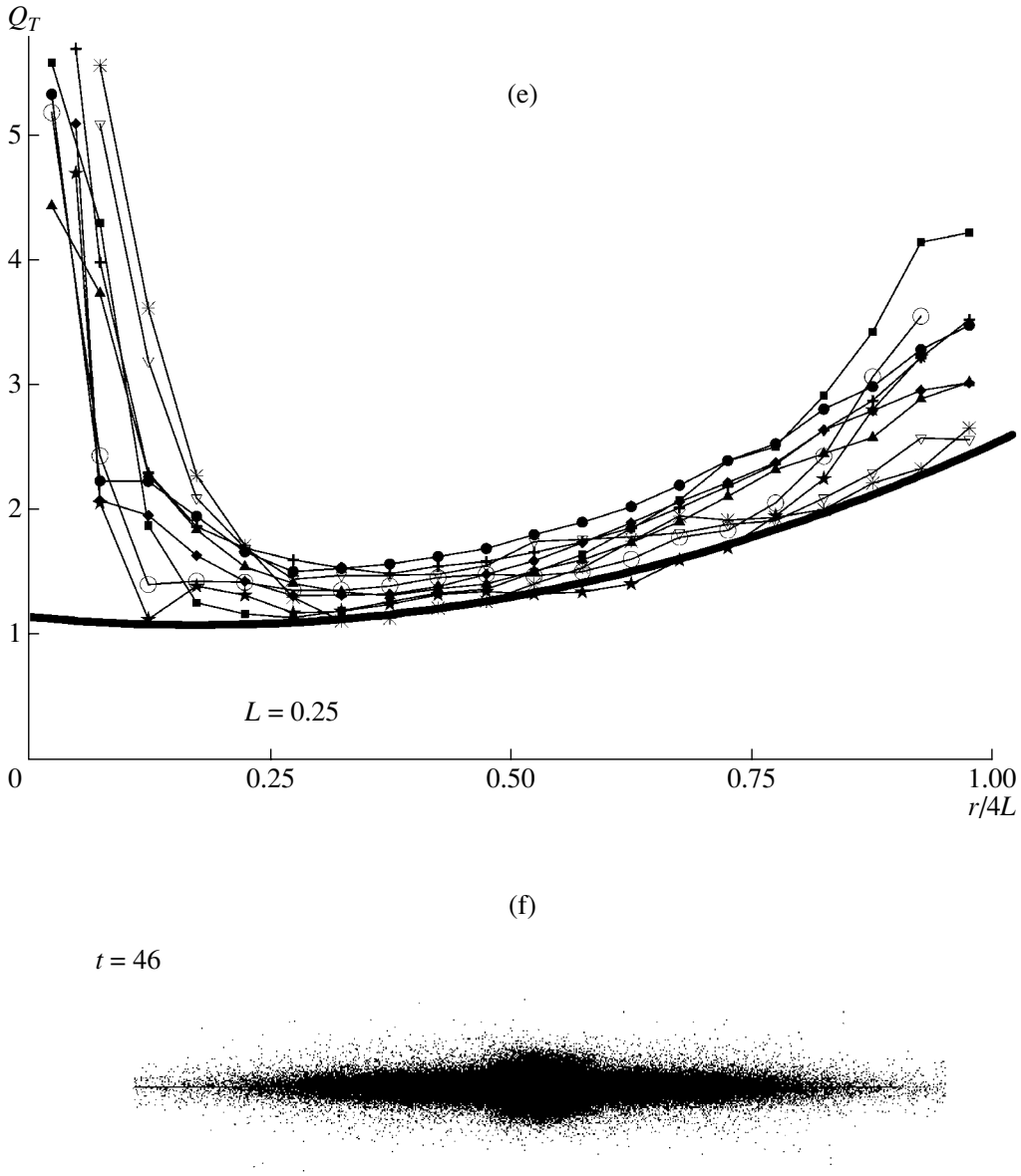

Fig. 7. (Contd.)

speaking, there is no reason why they must coincide with the Q_T values we have found, due to the local nature of the criteria applied, as well as due to the use of two-dimensional analytical models, while dynamical models treat the disk heating in three dimensions. The model velocity dispersions differ significantly from those predicted by various criteria (Figs. 5b–5d, 6b, 6e, 7b–7d, 8a, and 8b). However, there is no doubt that the formal application of these criteria will yield results that are correct to order of magnitude. In particular, like model estimates, they imply that $Q_T > 1$ at all r and that this parameter increases at the disk periphery. However, in none of the cases considered do the $Q_T(r)$ relations derived using local criteria agree with those found in this work for all radial distances ($0 < r < 4L$), and that they can differ from the model estimates by more than a factor of 1.5 at some distances r.

After passing through its minimum, the Toomre parameter $Q_T(r)$ for a disk that has reached a stable equilibrium state increases monotonically with r from $Q_T \simeq 2$–3 at a radius of $(3$–$4)L$ (this is usually close to the optical boundary of the disk in real galaxies). A similar increase of $Q_T(r)$ from 1.5 to 2.5 at the periphery was obtained earlier by Pichon and Lynden-Bell [49] using a different method (by constructing stable equilibrium distribution functions for flat systems over a wide range of free parameters) and has

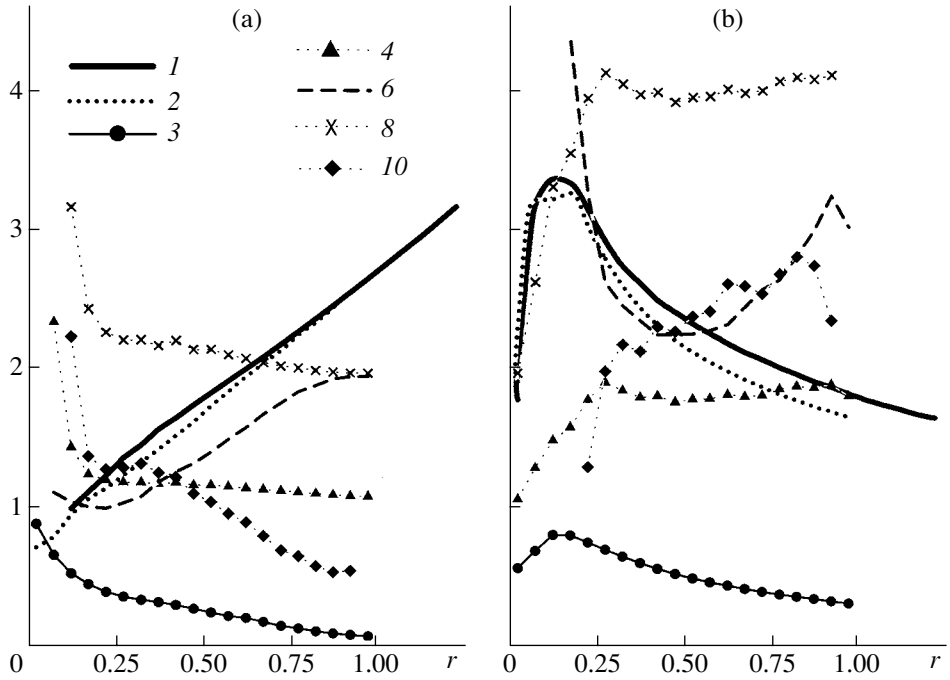

Fig. 8. Radial dependences of the disk parameters in the adopted units for the cases when (a) a significant part of the disk rotates in accordance with a quasi-rigid law, and (b) the rotation at $r > L = 0.25$ is close to Keplerian: *1* the circular velocity $V_c(r)$; *2* the rotational velocity of the disk (stars) $V(r)$; *3* the radial-velocity dispersion $c_r(r)$; *4* the parameter S computed using (3) for the circular velocity; *6* the Toomre parameter Q_T computed using the circular velocity; *8* the critical Toomre parameter $Q_T^{(P)}$ computed using (6) with $V_c(r)$; *10* the critical Toomre parameter $Q_T^{(M)}$ computed using (5) with $V_c(r)$. The notation is analogous to that in Fig. 5.

also been noted in results obtained for a number of dynamical models [5, 21, 24, 44–47].

The disks of galaxies whose halos are not too massive ($\mu \lesssim 1.5$) are subjected to bar instability. The suppression of the development of a long-lived bar in galaxies with low-mass spherical components requires not only a higher velocity dispersion (as shown long ago by Ostriker and Peebles [29] in their classic work) but also a higher value of the Toomre parameter Q_T, compared to galaxies possessing a massive halo or bulge. In this case, the development of a bar is accompanied by an increase in Q_T even in regions of the galaxy beyond the bar. This effect is apparently associated with the system being "overheated" above the threshold level: the development of the bar is accompanied by a redistribution of mass in the disk, so that the local decrease of the disk surface density for the given velocity dispersion results in an additional increase in Q_T. However, in this case, our models fail to yield *bona fide* quantitative estimates, since the parameters of the bar depend strongly on the initial conditions in the system. We have not analyzed here the conditions for the development of the bar mode in detail.

Our results make it possible to use numerical models to estimate the degree of dynamical heating of stellar disks and to derive estimates for the *a priori* unknown mass and density of a galactic disk from the observed velocity dispersion of the old stars making it up.

7. ACKNOWLEDGMENTS

We are grateful to A.M. Fridman, O.V. Khoruzhiĭ, and V.L. Polyachenko for useful discussions of this work and comments. This work was supported by the Russian Foundation for Basic Research (project no. 01-02-17597) and partially supported by the Federal Research and Technology Program "Research and Development in Priority Fields of Science and Technology" (contract 40.022.1.1.1101).

REFERENCES

1. A. Toomre, Astrophys. J. **139**, 1217 (1964).
2. A. G. Morozov, Astron. Zh. **58**, 734 (1981) [Sov. Astron. **25**, 421 (1981)].
3. A. V. Zasov, Pis'ma Astron. Zh. **11**, 730 (1985) [Sov. Astron. Lett. **11**, 307 (1985)].
4. R. Bottema, Astron. Astrophys. **275**, 16 (1993).
5. R. Bottema and J. P. E. Gerritsen, Mon. Not. R. Astron. Soc. **290**, 585 (1997).

6. B. Fuchs, in *Galaxy Dynamics*, ASP Conf. Ser. **182**, Ed. by R. D. Merritt, M. Valluri, and J. A. Sellwood (Astronomical Society of the Pacific, San Francisco, 1999), p. 365.
7. A. V. Khoperskov, A. V. Zasov, and N. V. Tyurina, Astron. Zh. **78**, 213 (2001) [Astron. Rep. **45**, 180 (2001)]; A. V. Zasov, D. V. Bizyaev, D. I. Makarov, and N. V. Tyurina, Pis'ma Astron. Zh. **28**, 599 (2002) [Astron. Lett. **28**, 527 (2002)].
8. A. M. Fridman and V. L. Polyachenko, *Physics of Gravitating Systems* (Springer-Verlag, New York, 1984).
9. V. L. Polyachenko and A. M. Fridman, *Equilibrium and Stability of Gravitating Systems* [in Russian] (Nauka, Moscow, 1976).
10. N. N. Gor'kavyĭ and A. M. Fridman, *Physics of Planetary Rings* [in Russian] (Nauka, Moscow, 1994).
11. C. C. Lin and F. H. Shu, Astrophys. J. **140**, 646 (1964).
12. O. P. Vandervoort, Astrophys. J. **161**, 87 (1970).
13. A. G. Morozov, Astron. Zh. **57**, 681 (1980) [Sov. Astron. **24**, 391 (1980)].
14. A. G. Morozov and A. V. Khoperskov, Astrofizika **24**, 467 (1986).
15. E. Griv, C. Yuan, and M. Gedalin, Mon. Not. R. Astron. Soc. **307**, 1 (1999).
16. A. G. Morozov, Pis'ma Astron. Zh. **7**, 197 (1981) [Sov. Astron. Lett. **7**, 109 (1981)].
17. V. L. Polyachenko, E. V. Polyachenko, and A. V. Strel'nikov, Pis'ma Astron. Zh. **23**, 598 (1997) [Astron. Lett. **23**, 525 (1997)].
18. N. W. Evans and J. C. A. Read, Mon. Not. R. Astron. Soc. **300**, 83 (1998p).
19. N. W. Evans and J. C. A. Read, Mon. Not. R. Astron. Soc. **300**, 106 (1998c).
20. J. A. Sellwood and N. W. Evans, Astrophys. J. **546**, 176 (2001).
21. G. Bertin, C. C. Lin, S. A. Lowe, and R. P. Thurstans, Astrophys. J. **338**, 78 (1989).
22. R. H. Miller, Astrophys. J. **223**, 811 (1978).
23. R. H. Miller, K. H. Prendergast, and W. J. Quirk, Astrophys. J. **161**, 903 (1970).
24. F. Hohl, Astrophys. J. **168**, 343 (1971).
25. F. Hohl, Astron. Space Sci. **14**, 91 (1971).
26. R. H. Miller, Astron. Space Sci. **14**, 73 (1971).
27. R. H. Miller, Astrophys. J. **190**, 539 (1974).
28. R. H. Miller, Astrophys. J. **223**, 811 (1978).
29. J. P. Ostriker and P. J. E. Peebles, Astrophys. J. **186**, 467 (1973).
30. R. A. James and J. A. Sellwood, Mon. Not. R. Astron. Soc. **182**, 331 (1978).
31. V. L. Polyachenko and I. G. Shukhman, Preprint Nos. 1–2, SIBIZMIR (Sib. Otd. Akad. Nauk SSSR, 1972).
32. A. J. Kalnajs, Astrophys. J. **175**, 63 (1972).
33. E. A. Mikhaĭlova and A. V. Khoperskov, Astron. Zh. **69**, 1112 (1992) [Sov. Astron. **36**, 573 (1992)].
34. E. Athanassoula and J. A. Sellwood, Mon. Not. R. Astron. Soc. **221**, 213 (1986).
35. C. J. Jog and P. M. Solomon, Astrophys. J. **276**, 114 (1984).
36. C. J. Jog and P. M. Solomon, Astrophys. J. **276**, 127 (1984).
37. B. Wang and J. Silk, Astrophys. J. **427**, 759 (1994).
38. V. G. Ortega, E. Volkov, and L. Monte-Lima, Astron. Astrophys. **366**, 276 (2001).
39. J. A. Sellwood and R. G. Carlberg, Astrophys. J. **282**, 61 (1984).
40. R. G. Carlberg and J. A. Sellwood, Astrophys. J. **292**, 79 (1985).
41. J. A. Sellwood and E. Athanassoula, Mon. Not. R. Astron. Soc. **221**, 195 (1986).
42. J. A. Sellwood, Mon. Not. R. Astron. Soc. **238**, 115 (1989).
43. J. A. Sellwood and D. N. C. Lin, Mon. Not. R. Astron. Soc. **240**, 991 (1989).
44. J. A. Sellwood and E. Athanassoula, in *Internal Kinematics and Dynamics of Galaxies* (Reidel, Dordrecht, 1983), p. 203.
45. H. C. Schroeder and N. F. Comins, Astrophys. J. **346**, 108 (1989).
46. B. Fuchs and S. von Linden, Mon. Not. R. Astron. Soc. **294**, 513 (1998).
47. J. M. Bardeen, *IAU Symp. 69: Dynamics of Stellar Systems,* Ed. by A. Hayli (D. Reidel, Dordrecht, 1975), p. 297.
48. A. V. Zasov and A. G. Morozov, Astron. Zh. **62**, 475 (1985) [Sov. Astron. **29**, 277 (1985)].
49. C. Pichon and D. Lynden-Bell, Mon. Not. R. Astron. Soc. **282**, 1143 (1996).
50. A. B. Romeo, Astron. Astrophys. **286**, 799 (1994).
51. A. B. Romeo, Astron. Astrophys. **335**, 922 (1998).
52. J. Sommer-Larsen, H. Vedel, and U. Hellsten, Mon. Not. R. Astron. Soc. **294**, 485 (1998).
53. J. C. Lambert and A. Bosma, Mon. Not. R. Astron. Soc. **314**, 475 (2000).
54. J. N. Bahcall, Astrophys. J. **276**, 156 (1984).
55. E. Athanassoula and A. Misiriotis, Mon. Not. R. Astron. Soc. **330**, 35 (2002).
56. V. P. Debattista and J. A. Sellwood, Astrophys. J. **543**, 704 (2000).
57. H. Hasan and C. Norman, Astrophys. J. **361**, 69 (1990).

Translated by A. Dambis

Astronomy Reports, Vol. 47, No. 5, 2003, pp. 377–385. Translated from Astronomicheskiĭ Zhurnal, Vol. 80, No. 5, 2003, pp. 409–418.

Spectroscopy of RC Sources

V. L. Afanas'ev[1], S. N. Dodonov[1], A. V. Moiseev[1], O. V. Verkhodanov[1], A. I. Kopylov[1], Yu. N. Pariĭskiĭ[1], N. S. Soboleva[2], A. V. Temirova[2], O. P. Zhelenkova[1], and W. M. Goss[3]

[1]*Special Astrophysical Observatory, Nizhniĭ Arkhyz, Russia*

[2]*St. Petersburg Branch of the Special Astrophysical Observatory, St. Petersburg, Russia*

[3]*National Radio Astronomy Observatory, Socorro, NM 87801, USA*

Received January 5, 2002; in final form, October 10, 2002

Abstract—The results of spectroscopic observations of the host galaxies of objects in the RC catalog (the "Big Trio" program) obtained using the new SCORPIO spectrograph of the Special Astrophysical Observatory are presented. The spectroscopic redshifts of the objects are compared with their photometric color redshifts, and the errors in the latter are estimated. Based on $BVRI$ observations obtained on the 6-m telescope of the SAO, the errors for the population of powerful radio galaxies are close to those found previously for radio quiet galaxies (about 10–20%). The detection of Ly α in the B filter in RC 1626+0448 is confirmed. This object is the second spectrally studied FR II radio source from the RC catalog to have a redshift $z > 2.5$. Star formation in its host galaxy began at a redshift $z > 3.3$. This first use of the new SCORPIO spectrograph demonstrates its promise for studies of very distant steep-spectrum radio galaxies brighter than 23^m–24^m in V. © *2003 MAIK "Nauka/Interperiodica".*

1. INTRODUCTION

It has become clear that the sensitivities of modern radio and optical observations are sufficiently high to detect radiation from the most distant high-luminosity objects in the Universe, in particular quasars and powerful radio galaxies. The "Big Trio" (RATAN-600, VLA, and 6-m telescope of the Special Astrophysical Observatory) project [1–3] was aimed at searching for candidate distant radio galaxies in a strip of sky with an area of about 100 square degrees deeply surveyed using the RATAN-600 telescope.

It is not possible to physically interpret the results of these observations without knowledge of the distances of the radio galaxies and of their spectra in all wavelength ranges. Radio spectra can be obtained relatively easily, but they enable only crude distance estimation based on the statistical "$\alpha - z$" dependence for these objects, where α is the radio spectral index and z the redshift of the source [4]. Refined estimates can be obtained once the objects are optically identified, based on the"$m - z$" dependence, where m is the apparent magnitude [5]. Analysis of the color characteristics enables two important new steps: refining the redshift and estimating the age of the host galaxy. The most complete information about the nature of an object can be derived only if its line and continuum radiation throughout the electromagnetic spectrum has been studied [6].

However, the dramatic growth in the volume of catalogs (to 10^6 or more objects) and the interest posed by weak (distant) objects makes it infeasible to perform deep spectroscopic observations of all cataloged objects due to the low photon fluxes involved. Exposures of hours are required for many objects, even using multichannel spectrographs to observe modest-size fields [7]. Therefore, the main thrust in research outside Russia has been surveys based on multicolor photometry with very accurate ties to direct spectral methods (for example, the Sloan survey [8, 9]).

Here, we report the results of photometric and color ($BVRI$) observations of some objects included in the Big Trio program using the 6-m telescope of the Special Astrophysical Observatory (SAO). These objects are powerful radio galaxies with supermassive black holes, and their photometric and color properties may differ from those of standard field galaxies. The use of non-Russian color data for calibration purposes is hindered by the absence of $BVRI$ data for this population of distant, powerful radio galaxies [10, 11].

Results of the first attempts to carry out spectroscopic observations of the host galaxies of objects from the RC catalog were published in [12]. Here, we present observations of four RC galaxies obtained using the new-generation SCORPIO spectrograph of the SAO. A brief description of this instrument is given on the web page

http://www.sao.ru/~moisav/scorpio/scorpio.html.

1063-7729/03/4705-0377$24.00

Table 1. Log of SAO 6-m spectral observations

Source name	Date	$T_{\rm exp}$, s	Seeing	z	PA
RC 0908+0451	March 17/18, 2001	4×600	2.0″	42°	107°
RC 1154+0431	March 17/18, 2001	2×600	1.6	40	108
RC 1626+0448	July 27/28, 2001	2×900	1.0	45	83
RC 1722+0442	July 26/27, 2001	2×360	1.3	47	62

Table 2. Comparison of redshifts obtained in different ways

Source name	$z_{\rm col}$	$z_{\rm sp}$	$\Delta z_{\rm col}$	$m - m_{\rm lim}$	Comments
RC 0908+0451	0.48	0.525	−0.03	−2.2	FRII, BLRG
RC 1722+0442	1.01	0.604	0.25	−0.1	FRII, NLRG
RC 1626+0448	2.35	2.656	−0.08	0.3	FRII, NLRG

Table 3. Ages

Source name	$t(z_{\rm sp})$ Myr	$t(z_{\rm col})$ Myr	T_U Myr	t_{sf} Myr	z_{sf}	Comments
RC 0908+0451	3250	3500	9050	<5800	>1.1	FRII, BLRG
RC 1722+0442	3500	4500	8450	4950	1.4	FRII, NLRG
RC 1626+0448	115	500	2600	2500	2.8	FRII, NLRG
RC 0444+0501	290	3000	2560	2270	3.0	FRII, NLRG

The SCORPIO spectrograph has made it possible to unambiguously determine the redshifts of such objects and consequently their absolute luminosities in both the radio and the optical. In principle, combined with color data, this enables the refinement of estimates of the ages of the galaxies' stellar populations and of the redshifts corresponding to the formation of the host galaxies.

Spectroscopic data are essential for the calibration of other indirect methods for estimating the distances and ages of objects in the special population of powerful radio galaxies. An initial selection of objects based on their radio properties has known advantages—a high relative radio luminosity compared to a galaxy's optical or infrared luminosity is a simple and efficient indication that the object is a giant stellar system with an old, supermassive black hole in its nucleus.

2. OBSERVATIONS

Spectroscopy

The observations were carried out during the testing phase of the new SCORPIO aperture-ratio reducer mounted at the primary focus of the 6-m telescope of the SAO. The maximum quantum efficiency of the instrument in its spectral regime was approximately 30% (at a wavelength of about 6500 Å). A direct-view prism with 300 lines/mm was used, which enabled observations at 3500–9500 Å with a spectral resolution of about 20 Å. This resolution is close to optimal for studies of FR II radio galaxies, which have narrow emission lines whose luminosities are close to the bolometric luminosity of the stellar population of the host galaxy [5]. The receiver was a TK1024 CCD detector with 1024×1024 pixels. The scale along the slit was 0.3″/pixel and the slit width was about 1.5″. A He–Ne–Ar calibration lamp was

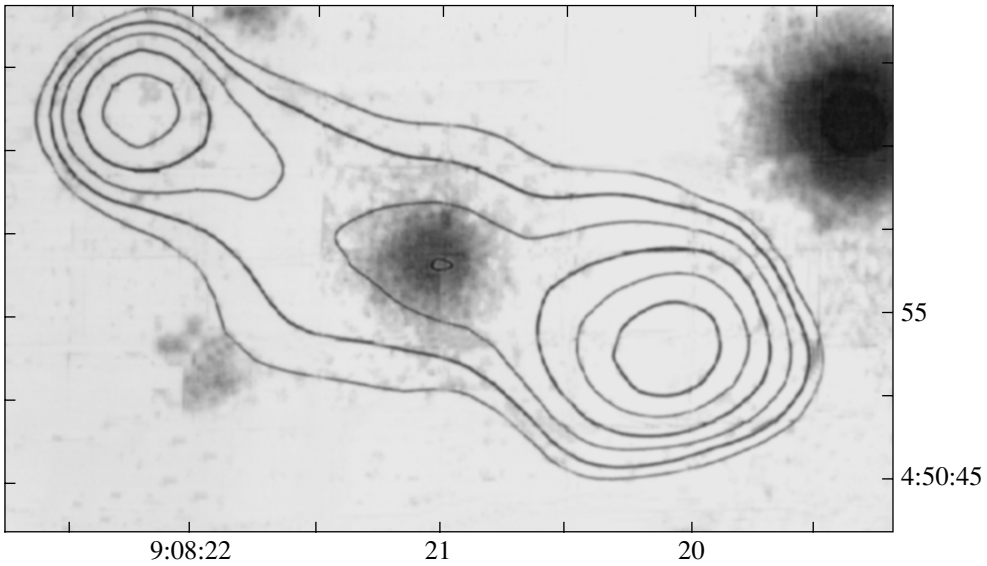

Fig. 1. Radio image of RC 0908+0451 at 1435 MHz (VLA) superposed on the R optical field (6-m telescope of the SAO). The axes plot right ascension and declination (2000). The contour levels are 0.0034, 0.0054, 0.0085, 0.0135, 0.0215, and 0.0340. The coordinate tie was carried out using the USNO catalog.

used to calibrate the wavelength scale. The absolute energy scale of the spectra were calibrated using nightly observations of a spectroscopic standard star in a slitless regime.

An interference pattern associated with the transmitted light (a moiré pattern) is observed for the CCD detector at wavelengths longer than 7500 Å. Since bright night-sky lines are included in this wavelength interval, we carried out the following procedure to subtract these lines more accurately. We made several exposures with the object shifted along the slit by $\sim 10''$ between each one. In the subsequent reduction of the object spectra, a "pure" sky spectrum was subtracted from the same position but on the shifted frame. Table 1 presents a log of the observations indicating the object name, observation date, total exposure time, mean seeing, mean zenith distance of the object, and the position angle of the slit.

RC 0908+0451. Figure 1 presents a radio image of this object superimposed on the corresponding optical field. The galaxy spectrum obtained using the new SCORPIO spectrograph is presented in Fig. 2. The slit passed through a neighboring star. The object was shifted along the slit between exposures of 2×600 s. The result of summing four 600-s exposures is shown. The MgII 2798, [NeV] 3426, [OII] 3727, Hγ, Hβ, and [OIII] 4959 and 5007 emission lines can be seen in the spectrum. The last line is distorted by an atmospheric absorption band. The stellar population of the radio galaxy can be identified fairly certainly from the CaII K and H absorption-line blend. Since the Hβ and MgII 2798 lines are rather broad, we classify the object as a broad-line radio galaxy (BLRG) with a redshift of $z = 0.525$.

RC 1154+0431. The spectrum of this source is presented in Fig. 2. The slit passed through a neighboring star. The result of summing two 600-s exposures is shown. MgII 2798, [NeV] 3346 and 3426, [OII] 3727, and [NeIII] 3869 emission lines with a redshift of $z = 0.998$ can be seen in the spectrum. The MgII 2798 line is very broad and strong, while the remaining lines are narrow. It appears reasonable to classify this object as a quasar. No compact core is visible on the VLA map, and we estimate the core-dominance ratio to be $R = S_{\rm core}/S_{\rm lobes} < 0.1$. The spectrum of the object resembles the mean spectrum for quasars with $R < 0.1$ from the MRC survey [13].

RC 1626+0448. The radio image superimposed on the optical field is presented in Fig. 3, and the spectrum is presented in Fig. 2. The observations were carried out in the presence of significant contamination by moonlight, and it was difficult to estimate the stellar continuum in the spectrum. Figure 2 presents only the gaseous component of the spectrum, which is of primary use for determining the redshift of the object. The spectrum is typical for high-z radio galaxies: narrow Lyα 1216, CIV 1549, HeII 1640, and CIII 1909 emission lines at a redshift of $z = 2.656$ are visible.

RC 1722+0442. The radio image superimposed on the optical field is presented in Fig. 4. The ratio of the object's radio luminosity to its optical luminosity is typical for powerful radio galaxies ($m - m_{\rm lim} = 0.1$, which corresponds to $L_{\rm rad}/L_{\rm opt} \sim 1$; Table 2). The

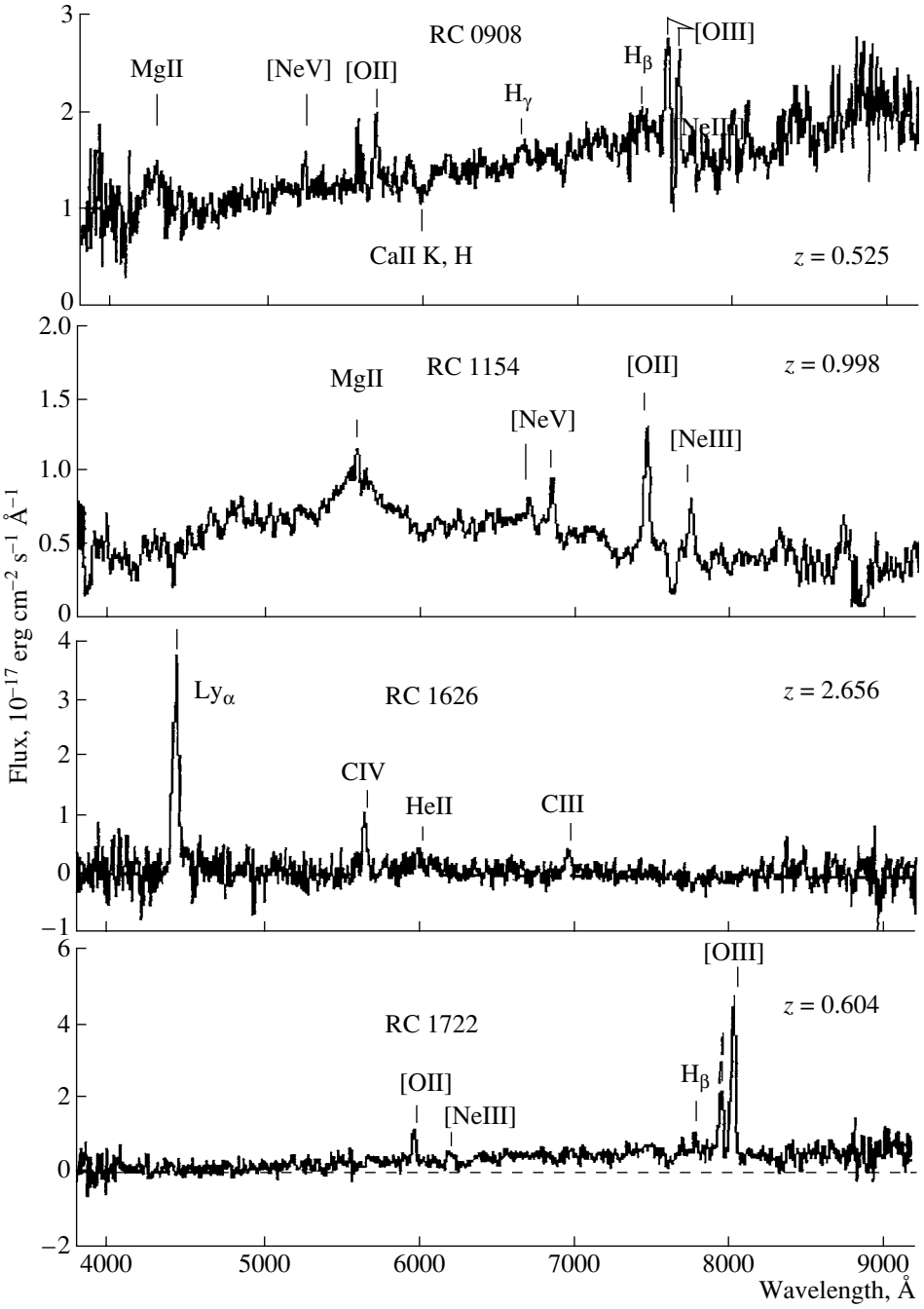

Fig. 2. Spectra of the radio sources RC 0908+0451, RC 1154+0431, RC 1626+0448, and RC 1722+0442.

object is situated in a group of galaxies. Its shape and size are typical of gE galaxies. The galaxy's spectrum is presented in Fig. 2. [OII] 3727, [NeIII] 3869, and H β emission lines are visible, as well as the [OIII] 4959, 5007 doublet. The line-intensity ratios are close to the standard values for powerful steep-spectrum radio galaxies [5]. The object's redshift is $z = 0.604$.

The absolute calibration of the spectra of weak objects requires additional study, and we have thus far used these spectra only to determine the source redshifts.

Spectral Energy Distributions

The color redshifts and ages of the stellar population were determined from the $BVRI$ observations obtained on the 6-m telescope and the PEGASE [15] and GISSEL98 [16, 17] model evolutionary spectral energy distributions (SEDs) [14]. The program used

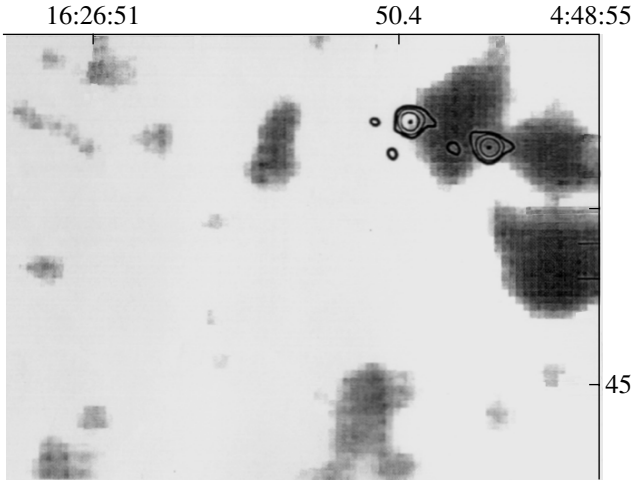

Fig. 3. Radio image of RC 1626+0448 at 4860 MHz (VLA) superposed on the R optical field (6-m telescope of the SAO). The axes plot right ascension and declination (2000). The contour levels are 0.0008, 0.0020, 0.0050, and 0.0127.

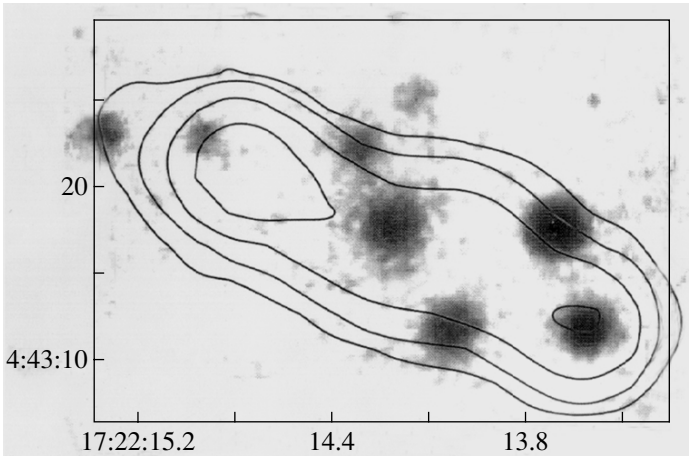

Fig. 4. Radio image of RC 1722+0442 at 1425 MHz (VLA) superposed on the R optical field (6-m telescope of the SAO). The axes plot right ascention and declination (2000). The contour levels are 0.006, 0.015, 0.038, and 0.095.

for these calculations is accessible in an interaction regime at the "Radio-Galaxy Evolution" web page http://sed.sao.ru. The main uncertainty in estimating the ages of the host galaxies is correct selection of an evolutionary model, even in the case of isolated galaxies.

Figure 5a presents contours of the normalized likelihood function in the $z - \log(t)$ plane for the radio galaxy RC 0908+0451, where t is the age of the galaxy; Figure 5b shows the corresponding model SED curve $\log S - \log \lambda$ for which the sum of the square residuals for the fit to the observed flux densities S in the four bands is lowest (for an age of 3500 million years and the GISSEL98 model).

According to its colors, this is a "blue" object, and it is located in the $(B - R) - (V - I)$ two-color diagram halfway between the position of normal elliptical galaxies with $z = 0.5$ and the region occupied by quasars. The jump in the spectrum at 4000 Å (in the rest frame of the object) is not prominent, suggesting that the spectrum at wavelengths shorter than 4000 Å is probably determined by the nonthermal continuum of the active nucleus and not the stellar population of the galaxy. This is supported by the fact that a core component is firmly detected in the FIRST radio map. Nevertheless, there is good agreement between the spectral redshift and the color estimates: $z_{\mathrm{PEGASE}} = 0.49$, $z_{\mathrm{GISSEL98}} = 0.48$. The age of the stellar population according to the PEGASE and GISSEL98 models is 1600 and 3500 million years, respectively. Due to the presence of a nonthermal continuum, these estimates should be considered lower limits for the true age of the galaxy.

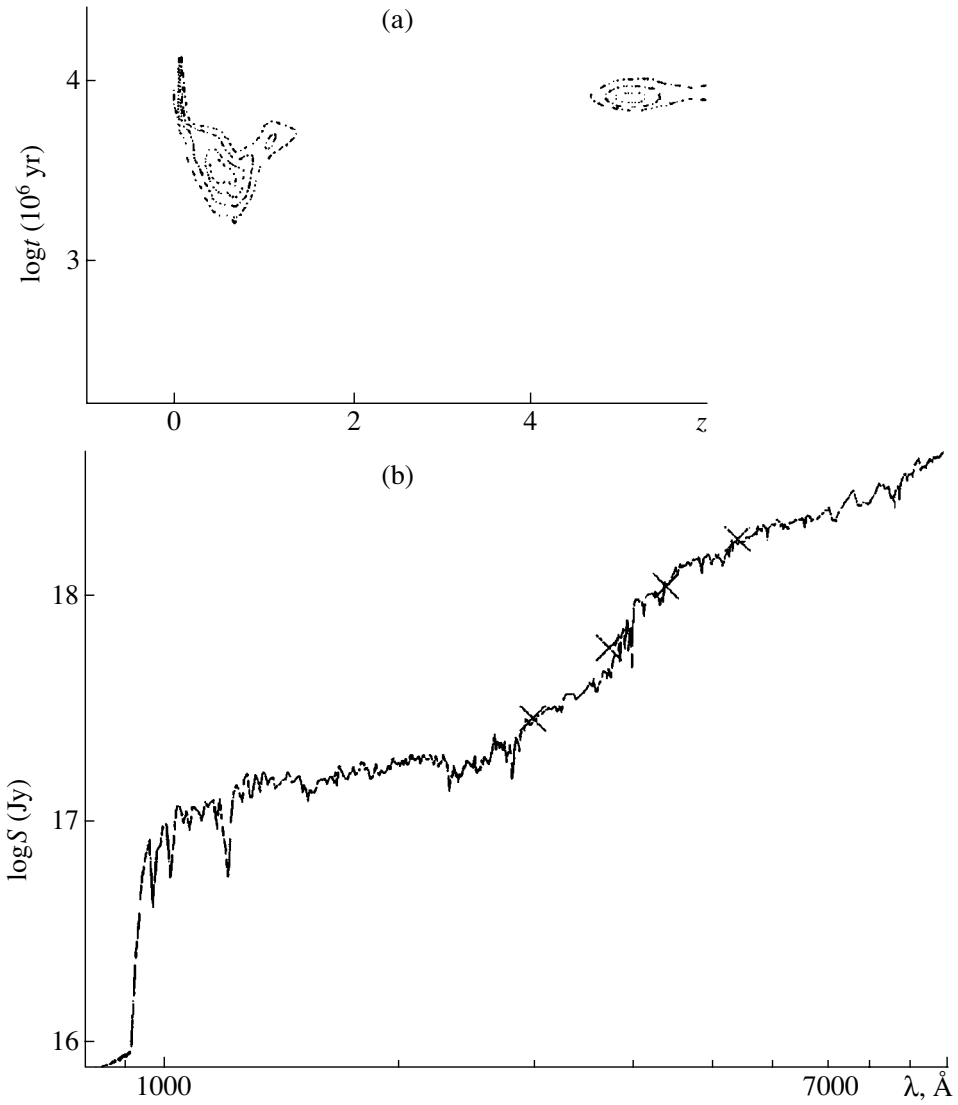

Fig. 5. (a) Normalized likelihood function in the z–$\log(t)$ plane, where t is the age of the galaxy in millions of years and z is its redshift, and (b) model SED $\log(S)$–$\log(\lambda)$ for an age of 3500 million years and the GISSEL98 model for RC 0908+0451. The crosses show the observed flux densities in the four filters in relative units (Jy).

Figure 6 presents the optical field of RC 1626+0448 in the $BVRI$ bands [18]. The brightness of the radio galaxy in the B band compared to nearby objects is striking. This is associated with the presence of powerful Lyα emission in this filter.

It was not possible to unambiguously determine the age of the stellar population of this galaxy on the basis of the model SEDs and four-color photometry. Figures 7a and 7b show two model SED curves for ages of 350 and 6000 million years. The x's denote the $BVRI$ flux densities obtained on the 6-m telescope. The redshift was taken to be equal to the spectral redshift ($z = 2.66$). It follows from Fig. 7 that the sums of the square residuals are roughly the same for ages from 350 to 6000 million years. Note that the age of the stellar system cannot exceed the age of the Universe at $z = 2.66$, or 2640 million years for a flat model with a Λ term ($\Omega_\Lambda = 0.7$, $H_0 = 65$ km s^{-1} Mpc^{-1}). The UV spectrum suggests the presence of a young stellar population with an age of 115 million years, which apparently dominates over the radiation of the older bulge stellar population. In such situations, IR observations are required to properly distinguish the population of old stars.

Figure 8a presents the normalized likelihood function in the $z - \log(t)$ plane for the radio galaxy RC 1722+0442, while Fig. 8b shows the corresponding model SED curve $\log S - \log \lambda$ for which the sum

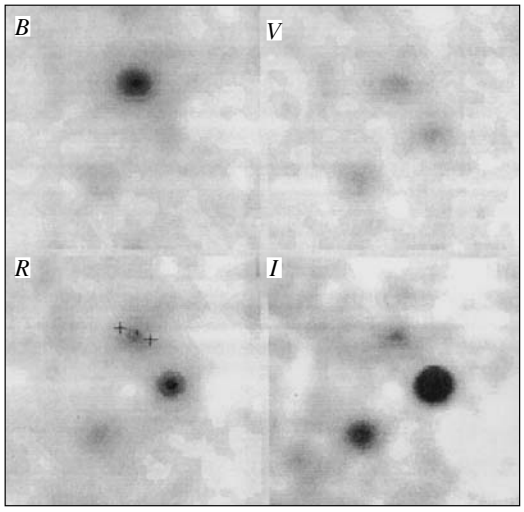

Fig. 6. Optical fields in $BVRI$ for RC 1626+0448 (6-m telescope of the SAO). The crosses mark the positions of radio components.

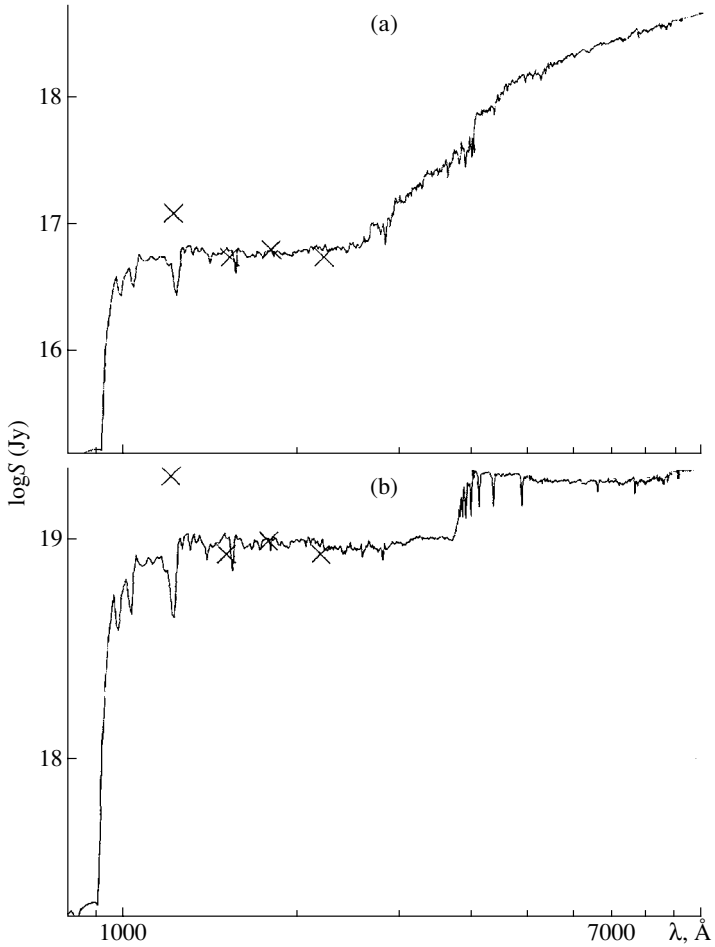

Fig. 7. Model SED (GISSEL98) $\log(S)$–$\log(\lambda)$ for RC 1626+0448 for ages of (a) 350 million years and (b) 6000 million years. The crosses show the observed flux densities in the four filters in relative Jy. The redshift is $z = 2.6$.

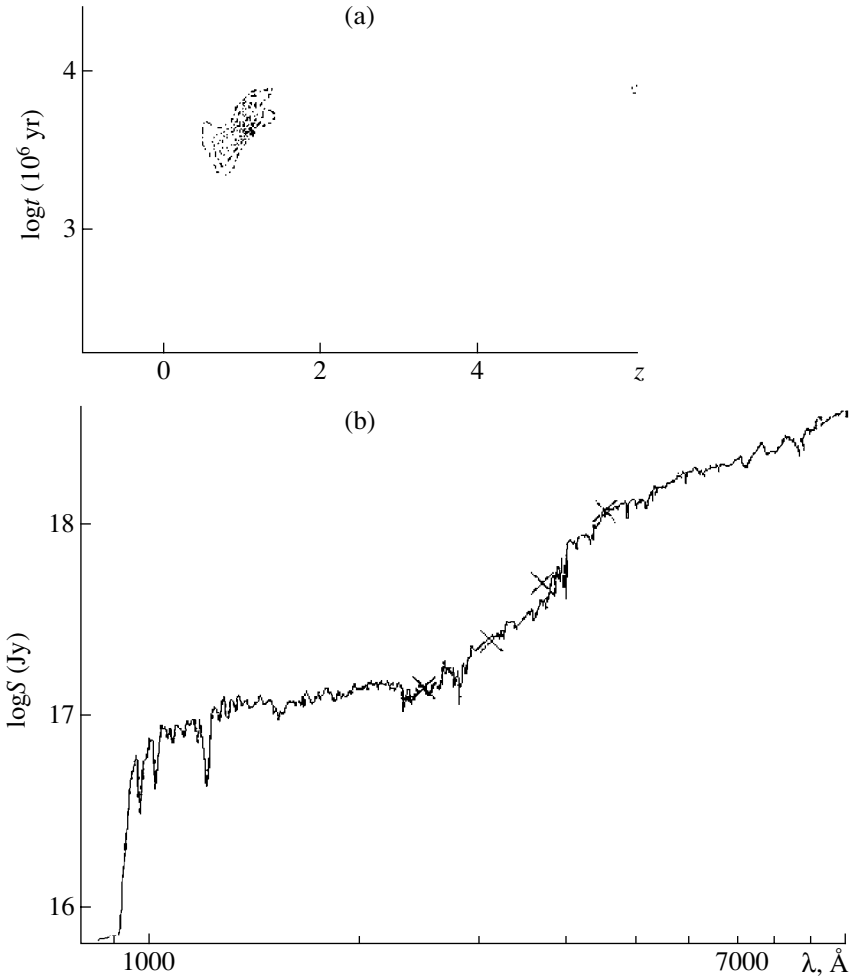

Fig. 8. (a) Normalized likelihood function in the z–log(t) plane, where t is the age of the galaxy in millions of years and z is its redshift, and (b) model SED log(S)–log(λ) for an age of 3500 million years and the GISSEL98 model for RC 1722+0442. The crosses show the observed flux densities in the four filters in relative Jy.

of the square residuals for the fit to the observed flux densities in the four bands is lowest (for an age of 3750 million years and the GISSEL98 model).

3. DISCUSSION

Redshifts

All the objects already show several emission lines in short exposures of about ten minutes, and their redshifts are easily determined. This is associated with the presence of a powerful gaseous component in the spectra of radio galaxies and quasars. A comparison with the multicolor photometric data is given in Table 2, which presents the name of the source, its color redshift $z_{\rm col}$, spectroscopic redshift $z_{\rm sp}$, the relative errors of the spectroscopic and color redshifts $\Delta z_{\rm col} = (z_{\rm col} - z_{\rm sp})/(1 + z_{\rm sp})$, and the value of $m - m_{\rm lim}$ [4], which characterizes the closeness of the radio and optical luminosities.

The mean and rms deviation of the color redshifts for the three FR II radio galaxies were 0.01 and 0.16, respectively. The errors in the color redshifts were no more than 25% for all the objects, in agreement with the pioneering results of the 1980s for nearby radio galaxies with $z \gg 1$ [19].

Ages of the Host-Galaxy Stellar Populations

We estimated the ages of the host galaxies with measured spectroscopic redshifts $t(z_{\rm sp})$ using evolutionary model SEDs for the integrated radiation of the stellar populations of gE galaxies, applying the method described in [14, 4] and evolutionary schemes in accordance with the GISSEL98 models [16, 17]. The results are summarized in Table 3, which includes high-luminosity FR II radio galaxies from the Big Trio sample whose spectra we had obtained by February 2002. Table 3 presents the source name, age of the host-galaxy stellar population calculated using

the GISSEL98 model $t(z_{\rm sp})$, the age of the stellar population derived simultaneously with the color redshift from the multicolor ($BVRI$) photometry $t(z_{\rm col})$, the age of the Universe at the epoch of the measured spectroscopic redshift for a flat model with a Λ term ($\Omega_\lambda = 0.7$, $H_0 = 65\ {\rm km\,s^{-1}\,Mpc^{-1}}$) T_U, the epoch of the last burst of star formation t_{sf}, and the redshift corresponding to t_{sf} for a flat model with a Λ term z_{sf}.

Formally, it follows from Table 3 that the epoch of the last burst of star formation is not very different from the epoch of high activity of galaxies in the radio.

4. CONCLUSION

(1) The use of the new SCORPIO spectrograph of the SAO for observations of radio galaxies has demonstrated qualitatively new capabilities for investigations of the early Universe based on studies of distant radio galaxies with emission lines in their spectra. Exposures comparable with those required for simple optical identification are able to remove ambiguity in estimates of the photometric and color redshifts of such radio galaxies and increase the accuracy of estimates of the ages of their stellar populations.

(2) The color redshifts of powerful radio galaxies are in satisfactory agreement with their spectral redshifts at least to redshifts of about three if the radiation of the stellar population dominates and quasars and radio galaxies are not confused. Closeness of the radio and optical luminosities can provide a useful criterion for selecting powerful radio galaxies. In the case of more distant (weaker) galaxies, only spectroscopic observations or the Lyman-break method [20] can remove ambiguity in the photometric and color redshift estimates.

(3) Spectroscopic observations of distant radio galaxies are required to estimate the ages of their stellar populations based on their metallicities, as well as to calibrate indirect methods (including multicolor photometry). However, this requires exposures of many hours. Such expenditure of observing time will surely be justified by new, model-independent methods for obtaining information about the evolution of the equation of state of the Universe from the dependence of the ages of old galaxies on their redshifts.

5. ACKNOWLEDGMENTS

This work was partially supported by a grant from the "Astronomy" program. Yu.N.P., N.S.S., and A.B.T. acknowledge partial support from the Russian Foundation for Basic Research (project no. 02-02-7-17 819, INTAS (grant 97-1192), COSMION, and the "Integration" program. The Very Large Array of the National Radio Astronomy Observatory is a facility of the National Science Foundation operated under cooperative agreement by Associated Universities, Inc.

REFERENCES

1. W. M. Goss, Yu. N. Parijskij, N. S. Soboleva, *et al.*, Astron. Zh. **69**, 673 (1992) [Sov. Astron. **36**, 343 (1992)].
2. W. M. Goss, Yu. N. Parijskij, A. I. Kopylov, *et al.*, Turk. J. Phys. **18**, 894 (1994).
3. T. Pursimo, K. Nilsson, P. Teerikorpi, *et al.*, Astron. Astrophys., Suppl. Ser. **134**, 505 (1999).
4. Yu. N. Parijskij, W. M. Goss, A. I. Kopylov, *et al.*, Bull. Spets. Astrofiz. Obs. **40**, 5 (1996).
5. P. J. McCarthy, Ann. Rev. Astron. Astrophys. **31**, 639 (1993).
6. L. Jones and G. Worthey, Astrophys. J. Lett. **446**, L31 (1995).
7. V. L. Afanas'ev, V. V. Vlasyuk, S. N. Dodonov, *et al.*, *Multipupil Spectrograph MPFS. Users Manual* (1995) (in Russian).
8. A. Fernandez-Soto, K. M. Lanzetta, H. W. Chen, *et al.*, Astrophys. J., Suppl. **135**, 41 (2001).
9. R. Stevens and M. Lacy, Mon. Not. R. Astron. Soc. **235**, 897 (2001).
10. O. V. Verkhodanov, A. I. Kopylov, Yu. N. Parijskij, *et al.*, Preprint No. 135 (St. Petersburg Spec. Astrophys. Obs., 2001).
11. O. V. Verkhodanov, A. I. Kopylov, Yu. N. Parijskij, *et al.*, Astron. Zh. **79**, 1 (2002) [Astron. Rep. **46**, 531 (2002)].
12. S. N. Dodonov, Yu. N. Parijskij, W. M. Goss, *et al.*, Astron. Zh. **76**, 323 (1999) [Astron. Rep. **43**, 275 (1999)].
13. J. C. Baker and R. W. Hunstead, Astrophys. J. Lett. **452**, L95 (1995).
14. O. V. Verkhodanov, A. I. Kopylov, O. P. Zhelenkova, *et al.*, Astron. Astrophys. Trans. **19**, 663 (2000).
15. M. Fioc and B. Rocca-Volmerange, Astron. Astrophys. **326**, 950 (1997).
16. M. Bolzonella, J. Miralles, and C. R. Pello, Astron. Astrophys. **363**, 476 (2000).
17. G. Brusual and S. Charlot, anonimous@ftp://gemini.tuc.noao.adu/pub/charlot/bc96 (1996).
18. Yu. N. Parijskij, W. M. Goss, A. I. Kopylov, *et al.*, Astron. Astrophys. Trans. **18**, 437 (1999).
19. C. Benn, J. Wall, M. Vigotty, *et al.*, Mon. Not. R. Astron. Soc. **235**, 465 (1988).
20. X. Fan, R. L. White, M. Davis, *et al.*, Astron. J. **120**, 1167 (2000).
21. S. Stern,H. Spinrad, P. Eisenhardt, *et al.*, Astrophys. J. Lett. **533**, L75 (2000).

Translated by D. Gabuzda

Astronomy Reports, Vol. 47, No. 5, 2003, pp. 386–400. Translated from Astronomicheskiĭ Zhurnal, Vol. 80, No. 5, 2003, pp. 419–435.

Wolf–Rayet Stars, Black Holes, and Gamma-Ray Bursters in Close Binaries

A. V. Tutukov[1] and A. M. Cherepashchuk[2]

[1] *Institute of Astronomy, Russian Academy of Sciences, ul. Pyatnitskaya 48, Moscow, 109017 Russia*

[2] *Sternberg Astronomical Institute, Universitetskiĭ pr. 13, Moscow, 119899 Russia*

Received September 10, 2002; in final form, October 10, 2002

Abstract—We consider the evolutionary status of observed close binary systems containing black holes and Wolf–Rayet (WR) stars. When the component masses and the orbital period of a system are known, the reason for the formation of a WR star in an initial massive system of two main-sequence stars can be established. Such WR stars can form due to the action of the stellar wind from a massive OB star ($M_{\rm OB} \geq 50M_\odot$), conservative mass transfer between components with close initial masses, or the loss of the common envelope in a system with a large (up to $\sim$25) initial component mass ratio. The strong impact of observational selection effects on the creation of samples of close binaries with black holes and WR stars is demonstrated. We estimate theoretical mass-loss rates for WR stars, which are essential for our understanding the observed ratio of the numbers of carbon and nitrogen WR stars in the Galaxy $\dot{M}_{\rm WR}(M_\odot\ {\rm yr}^{-1}) = 5\times10^{-7}(M_{\rm WR}/M_\odot)^{1.3}$. We also estimate the minimum initial masses of the components in close binaries producing black holes and WR stars to be $\sim 25M_\odot$. The spatial velocities of systems with black holes indicate that, during the formation of a black hole from a WR star, the mass loss reaches at least several solar masses. The rate of formation of rapidly rotating Kerr black holes in close binaries in the Galaxy is $\sim 3\times10^{-6}\ {\rm yr}^{-1}$. Their formation may be accompanied by a burst of gamma radiation, possibly providing clues to the nature of gamma-ray bursts. The initial distribution of the component mass ratios for close binaries is $dN \sim dq = dM_2/M_1$ in the interval $0.04 \lesssim q_0 \leq 1$, suggesting a single mechanism for their formation. © *2003 MAIK "Nauka/Interperiodica".*

1. INTRODUCTION

A primarily qualitative scenario for the evolution of massive close binaries from two initial main-sequence components to a final system of two relativistic stars was formulated in [1, 2]. In this scenario, the formation of Wolf–Rayet (WR) stars with OB companions results from the loss of the envelope by the primary in the course of its interaction with its companion, with the subsequent exposure of its helium core, which essentially is a WR star. The observed variation of the nitrogen and carbon abundances along the sequence WN → WC [3] was explained by the gradual baring of the helium core of the OB star due to mass loss via an intense stellar wind [4]. The existence of such winds is now beyond doubt [5], though their origin remains unclear. Theoretically, the evolution of a WR star ends with the collapse of its core and, as a rule, the formation of a black hole or neutron star. Therefore, the evolution of WR stars and black holes appear to be closely related and should be analyzed together using modern observations of massive close binaries (Tables 1, 2). Note, however, that details of the formation of a neutron star or black hole during the collapse of a WR core remain unclear [6].

WR stars are among the brightest stars; their basic parameters and distribution in the Galaxy have been well studied [7]. The ratio of the numbers of carbon and nitrogen WR stars $N_{\rm WC}/N_{\rm WN}$ increases toward the Galactic center. This is clearly a consequence of the increase in the abundance of heavy elements Z toward the Galactic center, with the gradient $d\log Z/dR \cong -0.05/{\rm kpc}$ [8]. As a result, in a neighborhood around the Sun with radius $\sim$4 kpc [7], the heavy-element abundance in young stars varies by almost a factor of two. The increase in the fraction of carbon WR stars toward the Galactic center can be understood if we assume that the mass-loss rate of these stars is proportional to their heavy-element abundance.

Studies of the local density of WR stars in the vicinity of the Sun can be used to estimate their total number in the Galaxy [7]. This number is close to 10^3 and will be used below to estimate the minimum initial masses of the OB components in close binaries that are transformed into WR stars during their evolution. Currently, about 200 Galactic WR

Table 1. Binary systems with WR components from [5, 24, 57]

System	Spectrum	$M_{\rm WR}M_\odot$	M_0, $M_\odot$	P, days	$e \pm \delta e$	Evolution
HD 63099	WC5+O7	9	32	14.3	0.0	CE
γ^2Vel	WC8+O7.5 III- V	9.5	30	78.5	0.33 ± 0.01	CE
HD 90657	WN5+O4-6	19	37	8.25	0.04 ± 0.03	CE
HD 92740	WN7h+O9 III- V	55	21	80.3	0.60 ± 0.01	W
HD 94305	WC6+O6-8	16	34	18.8	0	CE
HD 94546	WN4+O8 V	9	26	4.83	0.0	CE
HD 97152	WC7+O7 V	14	23	7.89	0.0	CE
HDE 311884	WN6+O5 V	51	60	6.24	0	W
HD 152270	WC7+O5-8	11	29	8.89	0	CE
CV Ser	WC8d+O8-9 IV	13	27	29.7	0.19 ± 0.03	CE
HD 186943	WN3+O9.5 V	17	36	9.56	0.07 ± 0.04	CE
HD 190918	WN5+O9 I	17:	34:	112	0.39 ± 0.07	CE
V444 Cyg	WN5+O6 III- V	9.3	27.9	4.21	0.04 ± 0.01	CE
HD 193793	WC7pd+O4- 5	27:	60:	2900	0.85 ± 0.01	W
CX Cep	WN4+O5 V	20	28.3	2.13	0	CE
HD 211853	WN6/WCE+O6 I(+WN+O)	15	27	6.69	$0.0 + 0.000$	CE
CQ Cep	WN6+O9 II-Ib	24	30	1.64	0.01 ± 0.01	W, CE
B22	WC6+O5-6 V-III:	12:	35:	14.9	0.17	C, CE
B32	WC4+O6 V-III:	5	30	1.92	0	CE
AB8	WO4+O4 V	14	52	16.6	0.19	C
HD 5980	WN4+O7 I	8:	27:	19.3	0.49	CE
AB6	WN3+O7	8	47	6.68	0	C
HD 193928	WN5+O5 V-III	45	30	21.7	0.02 ± 0.03	W
System	Spectrum	$f_{\rm WR}(M)$, $M_\odot$		P, days	e	
HD 62910	WN7/WCE+?	0.20		85.4	0.4	
HD 192641	WC7pd+O9	12.1		4760	> 0.12	
HD 193077	WN5o+B?	4.7		1538	0.28 ± 0.07	
AS422	WN+WC+?	7.7:		22.0	0	
B26	WN7+?	2.4		1.91	0	CE
B65	WN7+?	4.2		3.00	0	CE
B72	WN6+B1 Ia	3.8		4.31	0	CE
B82	WN6+O5	0.02		4.38	0	CE
B86	WNL/Of	1.6:		52.7:	0	
B87	WN6+?	0.10		2.76	0	CE
B90	WN7+?	1.4:		25.2	0	
HD 16523	WC5+?	~ 0.01		2.41	0.0	CE

Table 2. Parameters of binaries with black holes from [5, 54, 56]

System	Spectrum of optical star	$P_{\rm orb}$, days	$f_v(M)$, $M_\odot$	M_x, $M_\odot$	M_v, $M_\odot$	$V_{\rm pec}$, km/s	Comments	Evolution
Cyg X-1 (V 1357 Cyg)	O9.7Iab	5.6	0.24 ± 0.01	16 ± 5	33 ± 9	49 ± 14	Stationary	CE
LMC X-3	B3 Ve	1.7	2.3 ± 0.3	9 ± 2	6 ± 2	–	Stationary	CE
LMC X-1	O (7–9) III	4.2	0.14 ± 0.05	7 ± 3	22 ± 4	–	Stationary	CE
SS433	∼A7Ib	13.1	~ 1.3	11 ± 5	19 ± 7	–	Stationary	C
A0620-00 (V616 Mon)	K5V	0.3	2.91 ± 0.08	10 ± 5	0.6 ± 0.1	-15 ± 5	Transient	CE
GS 2023+338 (V404 Cyg)	K0 IV	6.5	6.08 ± 0.06	12 ± 2	0.7 ± 0.1	8.5 ± 2.2	Transient	CE
GRS 1124-68 (GU Mus)	K2 V	0.4	3.01 ± 0.15	6(+5, −2)	0.8 ± 0.1	26 ± 5	Transient	CE
GS 2000+25 (QZ Vul)	K5 V	0.3	4.97 ± 0.10	10 ± 4	0.5 ± 0.1	–	Transient	CE
GRO J0422+32 (V 518 Per)	M2 V	0.2	1.13 ± 0.09	10 ± 5	0.4 ± 0.1	–	Transient	CE
GRO J1655-40 (XNSco1994)	F5 IV	2.6	2.73 ± 0.09	6.3 ± 0.5	2.4 ± 0.4	-114 ± 19	Transient	CE
H1705-250 (V2107 Oph)	K5 V	0.5	4.86 ± 0.13	6 ± 1	0.4 ± 0.1	38 ± 20	Transient	CE
4U 1543-47 (HL Lup)	A2 V	1.1	0.22 ± 0.02	4.0–6.7	~ 2.5	–	Transient	CE
GRS 1009-45 (MM Vel)	(K6-M0)V	0.3	3.17 ± 0.12	3.6–4.7	0.5–0.7	–	Transient	CE
SAX J1819.3-2525 (V4641 Sgr)	B9III	2.8	2.74 ± 0.12	9.61(+2.08–0.88)	6.53(+1.6– 1.03)	–	Transient	CE
XTE J1118+480	(K7-M0)V	0.17	6.1 ± 0.3	6.0–7.7	0.09–0.5	126	Transient	CE
GRS 1915+105	(K-M)III	33.5	9.5 ± 3.0	14 ± 4	1.2 ± 0.2		Transient	CE

Note: Here, $P_{\rm orb}$ is the orbital period, $f_v(M) = \dfrac{M_x^3 \sin^3 i}{(M_x + M_v)^2}$ the mass function of the optical star, m_x and m_v the masses of the relativistic object and optical star, respectively, and $V_{\rm pec}$ the peculiar radial velocity of the center of mass of the binary.

stars are known, 24 of which are members of (WR + OB) spectral binaries with known orbital periods and component masses (Table 1 [5]). In addition, 12 WR stars are components of spectral binaries with known orbital periods but unknown masses (and sometimes natures) of their invisible components, which may be A stars, B stars, or black holes. These observational data form an invaluable basis for detailed studies of both the WR stars themselves and of the evolution of the massive close binaries from which they originate. We present here a quantitative analysis of the evolution of binaries that give rise to WR stars, with the aim of refining their basic evolutionary parameters and constructing a fuller picture of the previous evolution of certain particularly interesting systems.

According to the currently accepted scenario for the evolution of massive close binaries and the results of numerical simulations, nuclear burning in the core of a WR star ultimately results in its collapse and the formation of a relativistic remnant: a black hole (BH) or neutron star (NS) [1, 2]. Therefore, OB + WR and OB + BH systems are closely related in terms of their evolution. This evolution cannot be understood without a joint consideration of the observed parameters of these systems, which provides a basis for estimating the mass loss that occurs during the supernovae accompanying the formation of black holes in close binaries. Table 2 presents the main observed parameters of X-ray binaries with black holes according to [5]. We will use these data to estimate the minimum initial masses of the black-hole progenitors, as well as the mass loss from WR stars in supernova explosions.

Modern theories acknowledge three basic ways to bare the helium cores of massive stars, resulting in the formation of WR stars. In a close binary with comparable initial component masses, one component can lose its hydrogen envelope in the semidetached phase via conservative mass transfer between the components [4, 9, 10]. The total mass of the system remains constant; we call this the conservative (C) scenario. When the initial component mass ratio is large ($q_0 \gtrsim 1.5$), conservative evolution becomes impossible due to limitations on the accretion rate [11]. Under these conditions, the inevitable rapid and substantial expansion of the accretor during the accretion results in the formation of a common envelope, which is lost over a short time (possibly years) due to the orbital energy of the system [12]. For simplicity, the mass of the accretor is usually assumed to remain constant in this case. We call this the common-envelope (CE) scenario. The other currently known way for WR stars to form is related to the intense stellar winds from the most massive O stars [13, 14]. The possibility of such evolution for stars with masses exceeding $\sim 50M_\odot$ is confirmed by the absence of red supergiants with these masses [15]. In this case, binarity is not necessary, and the main-sequence star is transformed into a WR star with essentially no expansion [14–17]. We denote this the stellar-wind (W) scenario. For completeness, we should also note another previously discussed possible mechanism for the formation of a massive helium star: the continuous and total mixing of a massive star by Eddington rotational circulation. Standard estimates for the rate of this circulation can formally sustain the chemical homogeneity of the star if the velocity of its rotation is close to the critical velocity required to maintain equilibrium. We will consider this case in the Conclusion.

The above scenarios specify the variations of three basic parameters of close binary systems in the process of forming WR stars: the masses of the two components and the semimajor orbital axis. We will show that analyses of the main parameters of known binaries with WR components can be used to reconstruct the previous evolution of these systems. Secondary components with sufficiently large masses can also undergo a WR stage [2]. However, in the absence of a significant number of observed systems of this type (excepting possibly Cyg X-3), we will consider here only the evolution of the massive primary components.

2. THE EVOLUTIONARY STATUS OF WR STARS AND BLACK HOLES IN CLOSE BINARIES

Our quantitative estimates of the evolutionary parameters of massive close binaries are based on computed grids of evolutionary tracks for components with initial masses of $10M_\odot$–$64M_\odot$ [9]. Our results were confirmed by subsequent calculations [16], both qualitatively and quantitatively.

Let us present the main data required for numerical estimates of the key parameters of WR stars. Figure 1 displays the positions of a number of singular points that depend on the initial mass of the star. Line *1* indicates the relation between the mass of the convective stellar core and the initial mass of the star. If the mass of the star becomes smaller than the initial mass of its convective core due to mass loss, the abundance of hydrogen in its envelope will decrease, and the ratio of the nitrogen and carbon abundances will exceed unity. Starting from this moment, the massive OB star is transformed for an observer into a nitrogen WR star [4]. Mass loss in the most massive O stars is also followed by a WNL stage [18], when the helium core is enshrouded in an envelope with a substantial abundance of hydrogen. The optical component of the SS 433 system, which is a massive close binary near the completion of the second mass-transfer stage, can serve as an example of a massive star approaching its WNL stage. Line *2* in Fig. 1

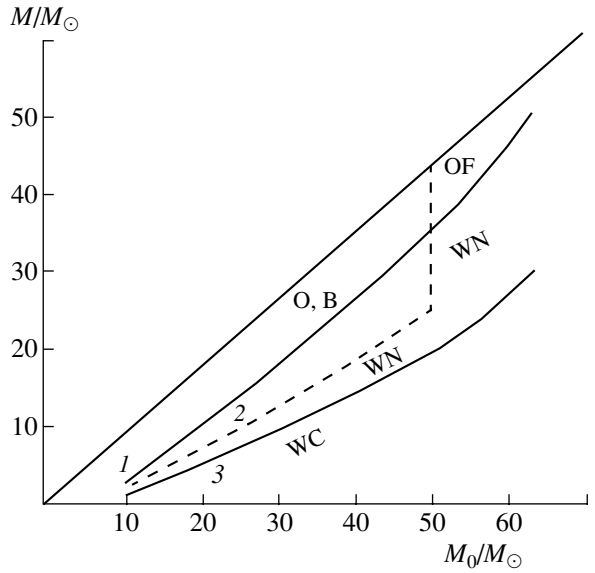

Fig. 1. Dependences of the (*1*) initial mass of the convective core, (*2*) mass of the helium remnant of the OB component, and (*3*) maximum mass of the convective helium core of the helium remnant on the initial mass of the star M_0. The evolutionary status of the remnant (WN or WC) is indicated.

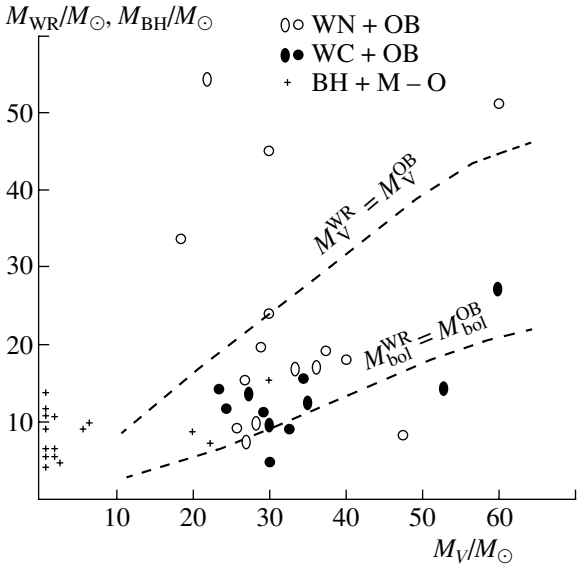

Fig. 2. Correlation between the masses of WR stars ($M_{\rm WR}$) and black holes ($M_{\rm BH}$) and the masses of the optical components (M_V) for the systems in Tables 1 and 2. See notation in the figure. The ellipses denote elliptical orbits ($e > \delta e$), while the circles correspond to circular orbits. The dashed lines delineate the region of comparable luminosities of the components of WR + OB systems. See the detailed description of these lines in the text.

indicates the relation between the mass of the helium remnant of the OB star M_R and the star's initial mass M_0. This dependence can be expressed analytically by the simple formula [2]

$$\frac{M_R}{M_\odot} = 0.1\left(\frac{M_0}{M_\odot}\right)^{1.4}. \qquad (1)$$

Finally, line *3* indicates the dependence of the maximum mass of the convective stellar core in the helium-burning phase on M_0. These cores are enriched in carbon, which is produced by helium burning, so that their exposure by their stellar wind transforms the nitrogen WR star into a carbon star [4].

Numerical models can be used to estimate the lifetime of a WR star in the core-burning phase [9]:

$$T_{\rm WR}({\rm years}) = 1.8\times 10^6\left(\frac{M_\odot}{M_{\rm WR}}\right)^{0.5}. \qquad (2)$$

It is important for estimates of the mass-loss rate in WR stars that the time for helium burning in the core is almost independent of the mass loss in the transition from the WN to the WC stage [9].

Observations indicate that the numbers of nitrogen and carbon WR stars in the solar neighborhood are comparable [7]. The relative abundance of WC stars probably depends on the heavy-element abundance [6, 19]; near the Sun, however, we can assume that the masses of the nitrogen-enriched and carbon-enriched layers ejected by a star in the WR stage are comparable. Since the total mass loss by a WR star in this case is $\Delta M/M_\odot \approx (M_{\rm WR}/M_\odot)^{0.8}$ (Fig. 1), the intensity of the stellar wind required to provide $N_{\rm WN} = N_{\rm WC}$ should be

$$\dot M_{\rm WR}(M_\odot/{\rm yr}) \cong 5\times 10^{-7}(M_{\rm WR}/M_\odot)^{1.3} \qquad (3)$$
$$\approx 2.3\times 10^{-9}\left(\frac{L_{\rm WR}}{L_\odot}\right)^{0.7}.$$

This assumes that there is no additional mixing in the interior of the star, except for convection. For V444 Cyg, formula (3) yields the observed mass-loss rate for the WR component [20], $\sim 10^{-5}M_\odot$ yr. Figure 1 indicates that the mass-loss rate (3) will be insufficient to expose the carbon-rich core of a star with an initial mass exceeding $\sim 50M_\odot$. Indeed, observations have shown that there are virtually no WC stars among the brightest [7] and most massive WR stars (Table 1, Fig. 2).

The mechanism by which WR stars maintain their intense stellar winds remains unclear [5]. Let us compare the momentum flux for the stellar wind from a WR star with the momentum flux for the star's radiation, or $L_{\rm WR}/c$ and $\dot M_L v_\infty$, where $L_{\rm WR}$ is the luminosity of the WR star, c—the speed of light, $\dot M_L$—the intensity of the stellar wind, and $v_\infty \cong 10^3$ km/s the velocity of the stellar wind at infinity. Then, the

ratio of the intensities of the momentum fluxes is

$$\frac{\dot{M}_{\rm WR}}{\dot{M}_L} = 115\left(\frac{L_\odot}{L_{\rm WR}}\right)^{0.3} \approx \left(\frac{86M_\odot}{M_{\rm WR}}\right)^{0.56}. \quad (4)$$

This clearly indicates that the wind momentum flux required to provide a comparable number of WN and WC stars exceeds the momentum flux of the radiation of a typical WR star with a mass of $\sim 10M_\odot$ by a factor of a few. For an OB star, empirically estimating the mass loss via the stellar wind in accordance with Conti [13] and Stothers [21] and adopting $\dot{M}_{\rm OB}(M_\odot/{\rm yr}) \cong 10^{-20}(L_{\rm OB}/L_\odot)^{2.5}$, and $v_\infty \approx 1000$ km/s, this ratio is

$$\frac{\dot{M}_{\rm OB}}{\dot{M}_L} \approx \left(\frac{L_{\rm OB}}{1.6\times 10^6 L_\odot}\right)^{1.5} \approx \left(\frac{M_{\rm OB}}{85M_\odot}\right)^{3.4}. \quad (5)$$

When (4) is compared with (5), it is apparent that the relations between the mass-loss rate and the luminosity are dramatically different for WR and OB stars. While the stellar wind from an OB star could be due to radiative acceleration, the nature of the WR stellar wind remains unclear. Though the pulsation instability of helium stars has not been exhaustively studied, this a very likely mass-loss mechanism for by WR stars.

The mass-loss rate of a star pulsating with an amplitude $\Delta R = \alpha R$ can be estimated by equating the work of the pressure forces in its atmosphere to the energy needed for mass loss from its surface. As a result, we obtain $dM/dt = 4\pi dvr/\kappa$, where v is the parabolic velocity on the surface and R is the radius of the Wolf–Rayet star, κ is the opacity. Substituting in the numerical values from [9] yields $dM/dt = 10^{-6}\alpha(M_{WR}/M_\odot)^{0.8}M_\odot$/year. The estimate shows that at $\alpha = 1$, this rate is high enough for the Wolf–Rayet stars to expose their carbon-rich layers in the time of helium burning in their nuclei. As a result, pulsation instability can actually be responsible for the mass loss by Wolf–Rayet stars and deserves further numerical studies.

Figure 1 shows that it is sufficient for a star with a mass exceeding $\sim 50M_\odot$ to lose $\sim 15M_\odot$ in order for it to be transformed into a nitrogen WR star. A simple estimate of the total mass loss at the above empirical rate [13] by an O star with luminosity $L_{\rm OB}/L_\odot = 63(M_{\rm OB}/M_\odot)^{2.25}$ over its lifetime on the main sequence ($T_{\rm MS} \approx 5.6\times 10^7(M_\odot/M_{\rm OB})^{0.75}$ years, according to the models of [2]) shows that a single O star whose initial mass exceeds $\sim 68M_\odot$ has time to lose a hydrogen envelope with the ratio C/N > 1 and so to be transformed into a nitrogen WR star (Fig. 1). The large (a factor of five) dispersion of the "observed" mass-loss rates of O stars and uncertainty in empirical upper limits for the masses of stars reaching the red-supergiant domain ($\sim 50M_\odot$) prevent us from estimating the significance of the discrepancy between the two limits above. This inconsistency can be removed by a quite plausible increase of the empirical mass-loss rates for OB stars by a factor of 4–5, or alternatively by taking into account the impact of rotational mixing on the evolution of the most massive stars. This latter possibility will be discussed in the Conclusion. Penetrating convection (overshooting) may also play a role.

Let us now consider the positions of close binaries with WR components from Table 1 in the $M_{\rm WR}$–$M_{\rm OB}$ plane (Fig. 2). Close X-ray binaries with black-hole components from Table 2 are also plotted here, as well as two lines indicating the obvious influence of observational selection effects. It is clear that, in order for both components of a close binary to be detected, their apparent luminosities must be comparable. The appropriate bolometric correction for a WR star, which is determined by its effective temperature, is not completely clear. We therefore plotted one line for the case when this correction is equal to that for an OB star ($M_{\rm bol}^{\rm WR} = M_{\rm bol}^{\rm OB}$) and another line corresponding to the assumption that the bolometric corrections for OB and WR stars can be derived from their theoretical temperatures using the models of [22] and the bolometric-correction tables of [23] ($M_V^{\rm WR} = M_V^{\rm OB}$).

The positions of the systems from Table 1 with known component masses are consistent with those expected based on the obvious observational selection effects. The fact that several systems are located beyond the delineated region may be due to remaining uncertainties in their effective temperatures, bolometric corrections, or component masses. The group of three WN stars with masses 30–$55M_\odot$ is especially worthy of attention. Their unusual position may be due to high hydrogen abundances in their cores resulting from total mixing during their evolution. This possibility is discussed in more detail in the Conclusion. It is evident that the frequently noted weak correlation (with correlation coefficient 0.07) between the masses of the OB and WR stars [24] is probably the result of the observational selection of systems whose components have comparable apparent magnitudes.

The scarcity of WR + OB systems beyond the strip marked in Fig. 2 does not indicate a real scarcity or absence of such systems. This is confirmed by the positions of close binaries from Table 2 with black-hole components in this diagram. Three systems whose optical components have masses of ~ 20–$40M_\odot$—Cyg X-1, LMC X-1, and SS 433—are located among their immediate progenitors—(WR + OB) stars. In most known systems with black holes, the donor masses do not exceed $\sim M_\odot$. Evolutionary computations indicate that the

initial masses of the donors in these systems did not exceed $\sim M_\odot$ [25]. Since the initial masses of main-sequence stars that produce black holes exceed $\sim 25M_\odot$ [25, 26], this implies that the initial mass ratio for the main-sequence components in massive close binaries reaches values as low as ~ 0.04. This is close to the value for recently detected planetary systems with massive planets around solar-type stars: ~ 0.01 [27]. Studies of spectral binaries have shown that the distribution of initial mass ratios q_0 for close binaries is flat, with $q_0 \geq 0.2$; i.e., $dN \sim dq$ [28]. The lifetimes of X-ray binaries with massive donors are on the order of the time for hydrogen burning in their cores, $\sim 3 \times 10^6$ yrs, while the lifetimes of systems with solar-mass donors are $\sim 10^9$ yrs [25]. For massive X-ray binaries, $q_0 \cong 1$; for low-mass systems, $q_0 \approx 0.04$. As a result, the ratio of the numbers of X-ray systems with solar-mass donors and massive donors should be ~ 10, given comparable intervals of initial semimajor axes of the systems and masses of their primaries. The observed ratio is close to this value (Table 2), which to first approximation confirms the validity of the law $dN \sim dq_0$ to $q_0 \approx 0.04$. This may provide evidence for a single mechanism for the formation of close binaries with a broad range of initial component-mass ratios. Note that X-ray systems with orbital periods shorter than ~ 10 days are intrinsic and are not the result of exchange collisions in the cores of globular clusters.

Figure 2 indicates that carbon WR stars possess smaller average masses than nitrogen WR stars. This is clear evidence for intense mass loss in WR stars due to their stellar winds. It is difficult to estimate these effects quantitatively on the basis of Table 1, which is incomplete and is not representative due to observational selection effects.

A formal comparison of the characteristic masses of the WR stars and black holes in Fig. 2 suggests that the transformation of a WR star into a black hole is accompanied by the loss of $\sim 5M_\odot$. However, as follows from Fig. 2, this estimate may be distorted by observational selection effects, which inhibit the detection of systems with low-mass WR stars, and also by the fact that the mass of the pre-supernova is ~ 30–50% [5] lower than the mass of the WR star, due to mass loss via the wind. We can estimate the mass loss accompanying a type Ib, Ic supernova resulting in the formation of a black hole using the peculiar spatial velocities of close binaries with black holes (Table 2). Assuming a cylindrically symmetrical supernova explosion, the spatial velocity of the system can be estimated from the conservation of momentum [2]:

$$v(\mathrm{km/s}) = 210 \frac{M_2(M_{\mathrm{WR}} - M_{\mathrm{BH}})}{(M_{\mathrm{WR}} + M_2)^{2/3}(M_{\mathrm{BH}} + M_2)P_{\mathrm{orb}}^{1/3}}. \quad (6)$$

Here, M_2 is the mass of the WR star's companion, assumed to remain constant during the explosion, M_{WR} is the mass of the WR pre-supernova taking into account radial mass loss via the wind, M_{BH} is the mass of the black hole produced by the supernova, and P_{orb} is the orbital period of the system in days. All masses in (6) are given in solar units.

Using this expression, we will now estimate the mass loss during the supernovae ($M_{\mathrm{WR}} - M_{\mathrm{BH}}$) for a number of systems with known spatial velocities (Table 2). In phases preceding the X-ray stage, systems with low-mass donors $M_2 < M_\odot$ have initial donor masses $\lesssim 1.5M_\odot$ [25]. Adopting for XTE J1118+480 $M_2 \cong 1.5M_\odot$, we find that the required mass loss during the supernova is $\sim 15.5M_\odot$. However, the preservation of the binary as a bound system during a cylindrically symmetrical explosion requires $M_{\mathrm{WR}} - M_{\mathrm{BH}} < M_{\mathrm{BH}} + M_2$, which yields an unacceptably large mass loss. It may be that the current estimates of the system parameters, particularly its spatial velocity, are still uncertain. Alternatively, it may be that the high velocity of this system is provided by a "kick" accompanying the supernova that formed the black hole. Such kicks are frequently introduced to explain the high spatial velocities of some radio pulsars. However, the need for kicks in connection with neutron stars is not obvious, since their high velocities can also be understood as a result of the decay of close binaries due to a second supernova in the system [28]. In addition, the preservation of XTE J1118+480 as a bound system after the supernova requires fine tuning of the kick: its value and direction must be close to those of the orbital velocity of the companion of the WR star at the time of the explosion. However, the other X-ray systems from Table 2 with close component masses and orbital periods do not display such high spatial velocities. This casts doubt on the existing estimates for the spatial velocity of XTE J1118+480.

The other system with a high spatial velocity is XN Sco1994. According to (6), the mass loss from this system during the supernova must have been $\sim 35M_\odot$. However, as in the previous case, this contradicts the preservation of the system during a symmetrical explosion. The estimated mass loss can be decreased to $14M_\odot$ by varying the system parameters within the uncertainties indicated in Table 2. However, this value is still larger than is reasonable for the preservation of the system. It is likely that the accuracy of the main observed parameters of this system is also overestimated. For the systems V2107 Oph, GU Mus, and V616 Mon, the mass losses during the supernovae required to explain the observed spatial velocities for $M_2 \approx 1.5M_\odot$ are 3.5, 2, and $2M_\odot$, respectively.

Summarizing the results of our estimates of the mass loss accompanying the formation of black holes in close binaries, we conclude that the currently available spatial velocities of X-ray binaries with black holes indicate mass losses comparable to the mass of the forming black hole. However, the preservation of the binaries as bound systems during the supernova requires that the mass loss not exceed the mass of the remaining black hole over a broad interval of black-hole masses. Refinement of these estimates requires that the accuracy of the parameters of X-ray systems be increased and the mass loss of the WR star due to its wind be taken into account [5]. An alternative explanation for the appearance of a high-velocity X-ray binary could be its ejection from a globular cluster [55] with a low minimum escape velocity ($\sim$30 km/s) and a high spatial velocity ($\sim$200 km/s).

The preservation of a system after a spherically symmetrical supernova can be used to derive an upper limit for the mass loss during the formation of its black hole. Since the minimum mass of the black hole is 4–$5M_\odot$ (Table 2) and the initial mass of the donor is $\sim M_\odot$, the total mass loss during the supernova in such a system should not exceed $\sim 6M_\odot$. Hence, the mass of a WR star producing a black hole with the minimum mass does not exceed ~ 10–$11M_\odot$, while the minimum mass of an OB star producing a black hole at the end of its evolution does not exceed 27–$29M_\odot$, according to (1).

The maximum masses of black holes in close binaries can be estimated based on the maximum luminosity of X-ray sources in the nearby Andromeda Galaxy and NGC 1316: $\sim 10^{40}$ erg/s [29]. Assuming that this is equal to the Eddington luminosity for helium accretion, we obtain $M_{\rm BH} \cong 50M_\odot$, while the initial mass of a star producing a black hole with this mass is $\sim 100M_\odot$.

Returning to Fig. 2, we note that the four most massive WR stars are nitrogen stars. This is consistent with the possibility that WR stars with such large masses form due to a stellar wind. As we noted while discussing formula (3), these stars should lose appreciably more matter during the "nitrogen" stage than their less massive analogues (Fig. 1). According to Fig. 1 and formula (1), the masses of the progenitors of the most massive WR stars can reach 65–$90M_\odot$. The characteristic minimum masses of WR stars (Fig. 2) are ~ 5–$8M_\odot$, which corresponds to OB progenitors with initial masses 23–$28M_\odot$, taking into account mass loss during the WR stage. Massey *et al.* [30] derived a similar limit of $\sim 20M_\odot$ by analyzing the rate of occurrence of WR stars in 12 young stellar clusters and associations for which the exact positions of the main-sequence turning points are known. Frequently used estimates of the minimum masses of stars undergoing the WR phase based on the star-formation function are less reliable due to uncertainties in the total number of WR stars [4, 7] and in the current star-formation rate in the Galaxy [28]. Comparing the lower limits on the masses of OB stars producing black holes and WR stars in close binaries, we conclude that they coincide within the remaining uncertainties and are equal to $25 \pm 5M_\odot$. It is presently difficult to tell whether this proximity has a physical basis or is purely coincidental.

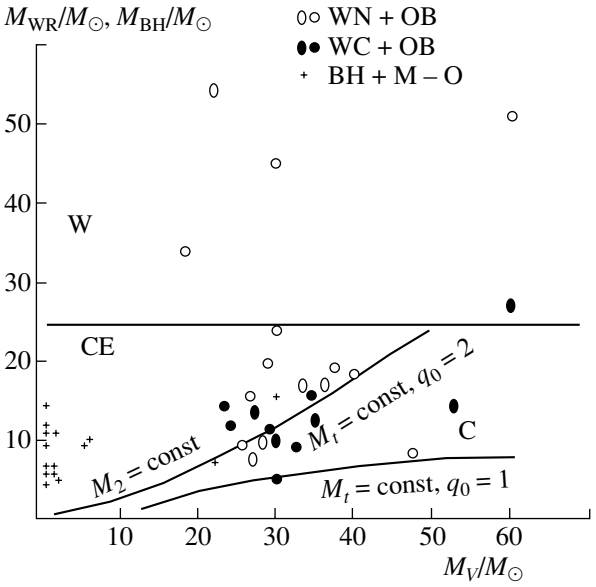

Fig. 3. Distribution of scenarios for the previous evolution of WR + OB and BH + M–O systems from Tables 1 and 2. W denotes systems with WR components formed due to outflow in the form of a stellar wind.

Finally, let us note another feature of the distribution of WR binaries in Fig. 2. Stars with OB-component masses lower than $23M_\odot$ are absent from the strip delineated by the observational selection effects. However, it appears that close binaries with black holes populate this domain uniformly. The absence of systems with less massive OB components could be explained partly by the cessation of the intense stellar wind in helium stars with masses lower than $\sim 8M_\odot$. Such stars become ordinary helium sub-dwarfs, which produce neutron stars and white dwarfs at the end of their evolution. Another reason for the lack of these systems in this domain could simply be that the total number of WR binaries with known orbital parameters is small. It remains unclear whether these two reasons suffice to explain this peculiarity.

Now, using the basic parameters of close binaries containing WR stars, we will attempt to reconstruct their evolution preceding the formation of the WR stars. We will adopt the component masses and orbital periods of the systems as the main identifying

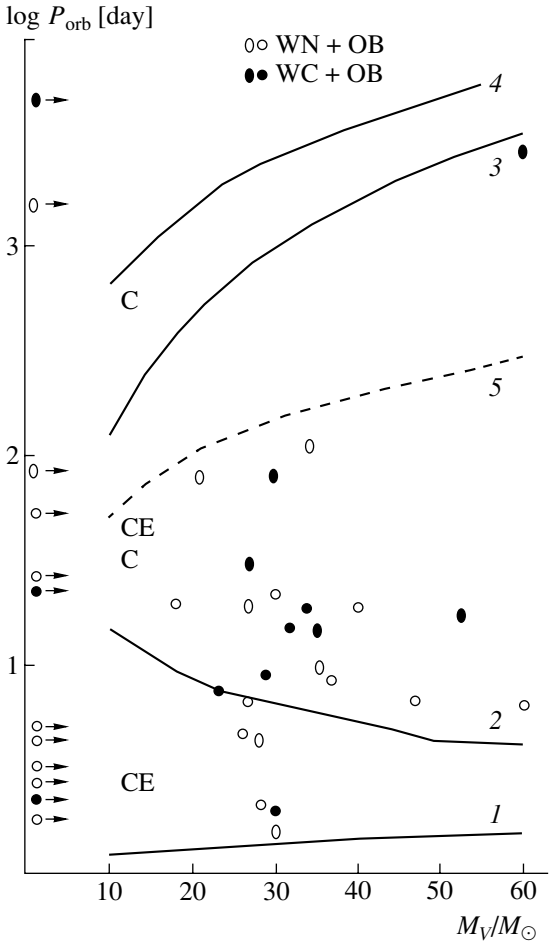

Fig. 4. Distribution of WR + OB systems from Table 1 in the P_{orb}–M_V plane. The dashed line indicates the position of systems for which the amplitude of the WR star's radial-velocity variations is $\Delta v = 250$ km/s (11). The orbital periods of systems with known mass functions are indicated to the left. The positions of the boundaries for various scenarios for the formation of WR stars are described in the text.

parameters (Table 1, Figs. 3 and 4). We can use theoretical evolutionary tracks [9] and the relation (1) together with Fig. 3 to determine the regions in which close binaries that have undergone qualitatively different evolutionary paths are located. Due to the stellar wind, components with initial masses higher than $\sim 50 M_\odot$ are transformed into WR stars with initial masses exceeding $\sim 24 M_\odot$, without significant mass transfer. According to (1), evolution that conserves the total mass transforms a system with initial component masses $M + M$ into a system with $0.1(M/M_\odot)^{1.4} + (2M - 0.1(M/M_\odot)^{1.4})$. This boundary is plotted in Fig. 3 as the line $M_t = \text{const}$.

After the end of hydrogen burning in the core of the primary, close binaries with large initial mass ratios evolve through a stage associated with the formation of common envelopes, due to the expansion of the accreting star [28]. In this case, the formation of a WR star is determined by the virtually complete loss of the extended hydrogen envelope of the primary, with the mass of the secondary remaining constant. In Fig. 3, the lower boundary of the region in which such systems can be located is indicated by the line $M_2 = \text{const}$. This line nearly coincides with that corresponding to the positions of WR + OB systems with initial mass ratios for their main-sequence components $q_0 = M_1/M_2 \approx 2$. This latter line can be adopted as an upper boundary for the region in which massive close binaries evolving conservatively during the WR-component formation phase are located.

As the result of this procedure, the M_{WR}–M_V plane (Fig. 3) becomes divided into four parts. The domain below the lines $M_t = \text{const}$, $q = 1$ should be inaccessible for WR + OB close binaries originating via any of the three currently known scenarios. Indeed, these binaries are absent from this region. Unfortunately, the fact that this domain coincides with that excluded by observational selection effects (Fig. 2) prevents us from knowing whether the absence of WR + OB systems from this forbidden region is significant. A zone of conservative systems (C) containing several systems with nitrogen and carbon WR stars is situated above this region. Above this zone is a region in which systems that have undergone a common envelope (CE) stage are located. About half of the WR stars in close binaries lie here, as well as nearly all known black holes in close binaries. Finally, the most massive WR stars in binaries are the products of mass loss by the primaries via their stellar wind (W). As expected, most of the WR stars in this domain are nitrogen stars. Since mass loss by WR stars decreases their masses by at least 20–30% (Fig. 1), the lower boundary of the W zone is actually situated near $\sim 19 M_\odot$. As a result, seven of the eight WR stars whose masses exceed $\sim 19 M_\odot$ are nitrogen stars. This makes it possible to place limits on the mass loss by the most massive WR stars (Fig. 1), 15–$20 M_\odot$.

The positions of WR binaries with eccentric orbits (Table 1) are interesting (Fig. 3). Nearly all belong to systems that have undergone a conservative mass-transfer phase or common-envelope stage. Known semidetached binaries undergoing a mass-transfer stage—Algol-type stars and cataclysmic binaries—possess circular orbits. The most massive Algols are HD 115071, with component masses $7 M_\odot + 17 M_\odot$ [31], and RY Sct, with component masses $M_1(\text{He}) = 11 M_\odot$, $M_2(\text{O7}) = 35 M_\odot$ [32]. One reason for the rareness of such systems may be that the massive progenitors of WR stars undergo short mass-transfer stages, whose duration coincides with the thermal

timescale, $\sim 3 \times 10^7 \left(\frac{M}{M_\odot}\right)^2 \left(\frac{R_\odot L_\odot}{RL}\right)$ yrs. During the brief common-envelope stage, the system will be observed as a single massive star displaying intense mass loss. The very likely formation of dust in the envelope may turn the star into a bright infrared source. Stars like η Car may be massive close binaries in a common-envelope phase.

It is important to note that the example of Algols with circularized orbits is obviously not appropriate for the progenitors of WR + OB systems, which retain substantial orbital eccentricities [24] (Table 1). The reasons for this evident difference remain unclear. As a rule, the envelopes of the donors in Algol and cataclysmic binaries are convective, and the duration of the Algol phase is usually not specified by the thermal timescale of the donor envelope but instead by the much longer time for the growth of the helium-core mass and the magnetic stellar wind [28]. These circumstances probably promote the comparatively rapid circularization of the orbits of observed Algols and cataclysmic binaries in the semidetached phase. As is shown in [24], the orbits of most Algols have already been circularized in the detached main-sequence stage, and the role of mass transfer in this process is secondary. For most of the observed massive WR + OB binaries in Table 1 and Fig. 3, the circularization of their orbits was probably excluded by the short time for the interaction between the components of the massive progenitors of these systems and by the low-viscosity radiative envelopes of these components. As a result, the orbits of WR + OB systems with orbital periods exceeding $\sim$14–15 days [24, 30] (Table 1) retain substantial eccentricities, despite the fact that they have undergone a conservative mass-transfer stage or common-envelope stage.

The orbital periods of the binaries should also be taken into account in order to ensure reliable identification of the WR + OB systems according to their preceding evolution. This is illustrated by Fig. 4, which presents the positions of the studied binaries in a plot of the mass of the optical component M_V vs. the orbital period of the system P. Several theoretical lines in this figure serve as guidelines for their evolutionary paths.

Line *1* denotes the lower limit for the orbital periods of systems consisting of main-sequence stars with equal masses. Line *2* marks the position of systems with equal initial component masses after conservative mass transfer, for the case when the mass of the remnant is described by formula (1). All conservative systems should be located above line *2*. As a result, all systems lying within the domain bounded by lines *1* and *2* may appear in this region only in the common-envelope stage. Generally speaking, systems with initial primary masses exceeding $\sim 50 M_\odot$ could also fall into this region if they have an intense stellar wind; however, none of the systems from Table 1 whose WR stars have masses higher than $\sim 25 M_\odot$ appear there.

Numerical models [9] indicate that the bolometric luminosity of a massive star in the red-supergiant stage is given by the equation

$$L_{\rm OB}/L_\odot \approx 100 (M_{\rm OB}/M_\odot)^{2.35}. \quad (7)$$

Assuming the temperature of the red supergiants to be $\sim$2500 K, we can find the dependence of the maximum radius of a star on its mass and therefore also the maximum possible semimajor axes for massive close binaries:

$$\frac{R_{\max}}{R_\odot} \cong 24 \left(\frac{M}{M_\odot}\right)^{1.2}; \quad \frac{A_{\max}}{R_\odot} = 60 \left(\frac{M}{M_\odot}\right)^{1.2}. \quad (8)$$

After the common-envelope phase, the maximum semimajor axis of a system with equal initial component masses will be

$$\frac{A_f}{R_\odot} = \frac{A_{\max}}{R_\odot}\frac{M_R}{M} \cong 6 \left(\frac{M}{M_\odot}\right)^{1.6},$$

while the orbital period of the system in the WR + OB stage is

$$P_{\rm orb} = 1\overset{\rm d}{.}5 (M/M_\odot)^{1.9}. \quad (9)$$

The boundary (3) is plotted in Fig. 4. After the common-envelope phase, a system can become even closer if the mass of the secondary is lower than the adopted value. However, this boundary represents an upper limit for the orbital periods of systems that have undergone a common-envelope phase. In Fig. 4, the lower boundary for these systems is specified by the limit (1). The boundary between close and wide systems can be estimated using formula (4) for the limiting semimajor axes of close binaries:

$$P_{\rm orb} \approx 33^{\rm d} (M/M_\odot)^{1.3}. \quad (10)$$

This is plotted as line *4* in Fig. 4.

Before proceeding to an evolutionary analysis of WR + OB systems with known orbital parameters, we will estimate the role of another obvious observational selection effect. Spectroscopic detection of the binarity of such massive stars with broad spectral lines requires that the amplitude of the WR star's radial-velocity variations due to the orbital motion exceed some value. For an observer located in the orbital plane of the system, this amplitude is

$$\Delta v ({\rm km/s}) = 430 \frac{M_{\rm OB}}{M_\odot} \frac{M_\odot^{2/3}}{(M_{\rm OB} + M_{\rm WR})^{\frac{2}{3}}} \frac{1}{P_{\rm orb}^{1/3}}, \quad (11)$$

where $P_{\rm orb}$ is the orbital period of the system in days. Adopting $M_{\rm WR} = M_{\rm OB}/3$ and $\Delta v = 250$ km/s, we derive for the upper limit of the orbital periods of detectable spectroscopic binaries $P_{\rm orb} \cong 5\dfrac{M_{\rm OB}}{M_\odot}$ days, plotted in Fig. 4 by the dashed line. It is obvious that nearly all WR + OB systems with known orbital periods satisfy this constraint. It is interesting that WR binaries with unknown secondary masses (Table 1) also obey this constraint. This testifies that the component masses are high—as a rule, comparable to the masses of the WR stars. This means that most of these components are either OB stars or massive black holes. Low-mass main-sequence stars or neutron stars are unlikely in these systems, if they are possible at all.

Let us now consider the evolutionary identification of the various domains in Fig. 4, delineated by the boundaries indicated above. First and foremost, the entire space above the boundary for extremely close systems (1) is accessible to (WR + OB) stars in which the WR stars originated as a result of mass loss due to their stellar wind. Therefore, Fig. 3 remains the sole basis for the evolutionary identification of systems with the most massive WR components. The domain confined between lines *1* and *2* (Fig. 4) is only accessible to systems after the common-envelope stage. Lines *2* and *3* restrict the domain accessible to systems that have undergone both a conservative mass-transfer stage (C) and a common-envelope phase (CE). Finally, the zone between boundaries *3* and *4*, populated by systems from Table 1, should contain (WR + OB) systems after the conservative mass-transfer stage (C). We can now use Figs. 3 and 4 for the evolutionary identification of these systems, whose main parameters are contained in Table 1.

A group of six WR + OB binaries in the domain occupied by systems that have undergone a common-envelope stage stands out in Fig. 4. The masses of their components also suggest that their origin was associated with these common envelopes (Fig. 3). Only the star B32 presents a problem (Table 1). Judging from the masses of its components (Fig. 3), it has undergone conservative mass exchange; however, its short and reliably determined orbital period rules out conservative mass transfer during the formation of the WR star (Fig. 4). To explain the position of this system in Fig. 3 as a result of evolution via a common-envelope stage, we must assume (if the extremely low mass for the WR star $\sim 5M_\odot$ is accurate) that the WR star already lost more than half its mass in the WR stage. Since this is a carbon WR star, it seems more probable than overestimation of the mass of the O component by nearly a factor of two. This would make it possible to shift the system into the domain of CE systems in Fig. 3.

It is interesting that, in the distribution of WR + OB stars in Fig. 4, 12 of 14 WR stars in systems with $P_{\rm orb} < 7$ days are nitrogen stars. Since the sample is small, it is difficult to estimate the significance of this fact; in Table 1, 25 of 36 WR stars are nitrogen stars.

Table 2 presents the evolutionary statuses of WR + OB binaries from Table 1, based on the location of these systems in Figs. 3 and 4. In principle, knowing the type of evolution a system has undergone makes it possible to estimate its initial parameters. Several systems seem peculiar from this point of view. According to Figs. 1 and 2, HD 193793 was produced by mass loss from a primary with an initial mass exceeding $\sim 60M_\odot$; however, judging from its orbital period, it is a close binary (Fig. 4). Figures 3 and 4 indicate that the WR component in the system AB6 was produced by conservative evolution in a system with initial component masses $28M_\odot + 27M_\odot$. The initial semimajor axis of this system was $\sim 14R_\odot$; i.e., it was essentially a contact system. In this connection, we should note that, in such close massive binaries, the evolution of the components does not result in the formation of hot helium WR stars [9]. In this case, an intense stellar wind must be invoked to remove the remnant of the hydrogen envelope. To obtain a WR star with the mass of the WR component in AB8, the initial mass of the progenitor must exceed $40M_\odot$. However, since the initial mass of the secondary in this system was $\sim 26M_\odot$, the evolution of this system was conservative. Judging from its current mass, the initial mass of the progenitor of the WR star in HD 190918 also exceeded $40M_\odot$. At the same time, its initial mass could not exceed $\sim 46M_\odot$, since this is a nitrogen WR star (Fig. 1). This rules out a defining role of the wind in the formation of the WR component in HD 190918. The large mass of the WR star makes a conservative scenario impossible. As a result, only a common-envelope scenario is possible for this system, with the initial component masses being $45M_\odot + 34M_\odot$ and the initial semimajor axis of the system being $\sim 10^3 R_\odot$.

Summarizing our evolutionary identifications for the WR + O systems (Table 1), we conclude that most have undergone a common-envelope stage. This is a result of the observational selection effects (Figs. 2, 3) and the comparatively small number of initial OB + OB systems with close initial component masses. This last factor is a necessary condition in order for the mass exchange to be conservative.

Once the origins of the WR stars in close binaries from Table 1 have been established, we can return to our estimation of the minimum mass of an O star that is transformed into a WR star during evolution in a

close binary. The initial mass of the progenitor of a WR star in a conservative system is half the sum of the current masses of the components. The lowest initial mass is observed for AB6 ($27M_\odot$; Table 1). In systems that have undergone a common-envelope stage, the minimum mass of the progenitor is close to the current minimum mass of the OB component of the WR star. According to Table 1, this value is ~ 23–$27M_\odot$.

The minimum masses of OB stars that are transformed into WR stars during the helium-burning stage can also be estimated from their number in the Galaxy, based on the initial star-formation function for binaries [28]:

$$d^3N = 0.2d\log a\frac{dM_{10}}{M_{10}^{2.5}}dq_0, \qquad (12)$$

where a is the semimajor orbital axis, q_0 is the initial component mass ratio, and M_{10} is the initial mass of the primary in solar units. Using expression (2) for the lifetime of WR stars and assuming $\Delta\log a = 5$ for stars with $M_{10} > 50$, we conclude that ~ 360 of ~ 1000 WR stars [7] were produced by the evolution of these most massive stars. For stars with $M_{10} < 50$, $\Delta\log a \cong 2$, since only close binaries undergo a WR stage. To provide the "missing" WR stars, we must assume that the minimum mass of an OB component in a close binary that evolves into a WR star is $24M_\odot$. Summarizing the above estimates for the minimum masses of OB stars in the Galaxy that are transformed into WR stars in close binaries, we obtain $\sim 25 \pm 2M_\odot$. A decrease in the heavy-element abundance by a factor of ten (the SMC) increases this limit to $\sim 70M_\odot$ [33], emphasizing the role of the stellar wind in the formation of WR stars.

To conclude our analysis of the minimum masses of the OB components of close binaries in the Galaxy that are transformed into WR stars and black holes, we note that these two limits are similar and equal to ~ 25–$30M_\odot$. In other words, with time, virtually all WR stars are transformed into black holes. Since the presence of a companion or a hydrogen envelope around a helium star does not affect the final product of its evolution, this conclusion remains valid for both the components of wide binaries and for single massive stars. The transformation of a WR star into a black hole is accompanied by mass loss comparable to the mass of the black hole, which is probably formed in a type Ib, Ic supernova. For example, supernova SN 2002ap (Ic) displayed evidence for a pre-supernova wind with $\dot{M}_{\rm WR} \cong 10^{-6}M_\odot/{\rm yr}$ [34], which is typical for WR stars.

3. GAMMA-RAY BURSTERS

Recently, evidence has accumulated that at least some such supernovae are accompanied by gamma-ray bursts [35–37]. Such a burst was detected during the explosion of SN I998bw and identified with the gamma-ray burst GRB 9804425 [38]. One possible explanation for the origin of gamma-ray bursts is that they are associated with the formation of rapidly rotating (Kerr) black holes [39, 40]. The condition for the formation of such a black hole is

$$\omega^2 R_{\rm BH}^3 \gtrsim GM_{\rm BH}, \qquad (13)$$

where ω is the angular velocity of rotation of the black hole, G is the gravitational constant, and $R_{\rm BH}$ and $M_{\rm BH}$ are the radius and mass of the black hole. The rotation of the cores of single pre-supernovae or of the components of wide binaries probably slows during their evolution to such small velocities that the products of the stellar collapse (radio pulsars and black holes) rotate with velocities that are far from their limiting values. The presence of a close companion of a compact helium pre-supernova restricts the angular velocity of rotation of its core—the future black hole with the orbital angular velocity of the system. Estimates indicate that, in order to obtain a rapidly rotating black hole, the iron core of the pre-supernova must have its minimum density, and the pre-supernova star must undergo a red-supergiant phase, which results in the formation of a compact final system. In other words, $M_{10} \cong 50M_\odot$, $\Delta M_{10} \cong 10M_\odot$. If the mass of the progenitor is known, the Galactic rate of supernovae that are accompanied by the formation of Kerr black holes from WR stars can be estimated from the star-formation function (12); with $dq_0 = 0.1$ and $\Delta\log a_0 = 0.3$, we obtain $\sim 3\times 10^{-6}$/yr. If we take the number of galaxies with masses on the order of the mass of the Milky Way within the horizon to be 10^9 [41, 42], the theoretical gamma-ray burst rate will be ~ 3000/yr, much higher than observed rate of ~ 300/yr, or 10^{-6}–10^{-7} per year per galaxy [22, 43]. This discrepancy obviously can be explained by invoking collimation of the gamma-rays within a narrow solid angle [45, 46]. It is interesting that, for a specified energy, collimation acts in the required direction only if there is a spatial horizon. In Euclidean space, the narrowing of the "beam" increases the rate of the corresponding events. Therefore, the formation of a Kerr black hole in a system in which the secondary has a mass of $\sim 50M_\odot$ and fills its Roche lobe, with this event being accompanied by the generation of directed gamma radiation, may serve as a model for gamma-ray bursts. The orbital period of such a system at the moment of the supernova is ~ 2.5 hours. It is interesting that the explosion of SN 2002ap (Ic) was accompanied by the ejection of a relativistic jet of gas [44].

4. CONCLUSION

We have analyzed two types of observed massive close binaries based on current concepts about their

formation and evolution. Our main result is the conclusion that the qualitative scenarios for the formation and evolution of these systems suggested about 30 years ago remain valid. A quantitative analysis of the basic parameters of WR stars and black holes in close binaries in Tables 1 and 2 can be used to find the observed analogs of these scenarios and thereby confirm the existence of three main mechanisms for the formation of WR stars: conservative mass transfer, evolution with a common envelope, and evolution with a stellar wind.

The formation of WR stars during the evolution of massive, rapidly rotating OB stars with circulation-induced total mixing remains unclear. Formally, the HR diagram for the most massive stars [15] does not contain stars to the left of the main sequence. Stars evolving with total mixing should be situated precisely in this region. However, determination of the bolometric luminosities and effective temperatures of massive stars with intense stellar winds remains difficult, and the transition stage (Of–WR) is short. Therefore, the few stars that are observed in this stage may be classified as either Of or WR stars. WR stars that have originated during evolution with total mixing should primarily be found among the most massive components of close binaries with $M_{\rm WR} \gtrsim M_{\rm OB}$. According to Table 1, such systems include HD 92740, HD 193928, and SMC WR7. However, we should keep in mind that, in the framework of our analysis, the evolution of these systems does not differ substantially from that of systems undergoing mass loss due to their stellar wind. In addition, it is evident that all massive stars rotate at close to the critical rate, and only a strengthening of the stellar wind with mass (5) rules out the formation of red supergiants from stars with masses exceeding $\sim 50 M_\odot$. The appropriate scenario can be chosen on the basis of observational and theoretical studies of variations of the chemical compositions of OB and WR stars. Circulation results in total mixing in the star, during which most of the initial carbon should be transformed into nitrogen in the core. As a result, a star evolving in the presence of total mixing should have N/C > 1, unlike nonmixed stars, in which this ratio retains its initial sense: N/C < 1. Stars with nitrogen (OBN) and carbon (OBC) excesses are known [47]. The most massive stars in the LMC and SMC are nitrogen stars (ON) and display an excess of nitrogen compared to carbon [48]. Further studies of the statistics of these stars, and especially of the correlation between the N/C ratio and the rotational velocity, are needed to establish the role of mixing in creating the observed C and N abundance anomalies in the most massive OB stars.

The conservative mass-transfer phase, which continues over the thermal timescale for the donor's evolution, is so short that the only known example of such a semidetached system is RY Sct [32]. To realize this scenario, the initial masses of the components must be close. It was shown in [32] that the massive close binary RY Sct is in the final stage of quasi-conservative mass exchange and is being transformed into a WR + OB system. The number of (WR + OB) systems in Table 1 that have undergone a conservative mass-transfer phase is small. Most WR + OB systems with known parameters have undergone a common-envelope phase. Systems in a common-envelope phase cannot be identified unambiguously. This phase is very short and should be accompanied by intense mass loss [28]. According to theoretical estimates, this mass-loss rate can reach 10^{-4}–$10^{-2} M_\odot$/yr. Unique objects with large IR excesses, such as η Car, may be such stars. Intense mass loss is manifest in the expanding ring-like shells that are visible around a considerable fraction of WR stars [49]. Since the period when such a shell can be detected is short, it is natural that nearly all WR stars with shells are nitrogen stars. The existence of such objects provides evidence in favor of the common-envelope scenario for close binaries. The system Cyg X-3, which contains the star WN3-7 and an accreting relativistic object, probably also underwent a common-envelope stage during the secondary mass transfer [50].

Numerical simulations of the evolution of massive close binaries can be used to quantitatively estimate the mass-loss rates of WR stars that are required to provide approximately equal numbers of carbon and nitrogen WR stars in the solar neighborhood. The resulting estimate is close to the observed WR mass-loss rate derived from variations of the orbital period of V444 Cyg. Further verification of the theoretical relations requires observational estimates of the mass-loss rates of other WR stars in close binaries from Table 1. When the observed mass-loss rates for WR stars and main-sequence OB stars with the same bolometric luminosities are compared, it is clear that WR stars have substantially higher mass-loss rates. The reasons for this difference remain unclear, as does the mechanism for the formation of the intense stellar winds from WR stars.

The spatial velocities of close binaries with black holes can be used to estimate the variations of the masses of the WR progenitors of black holes during the supernova explosions in which the black holes are formed. It was found that the WR star loses several solar masses during the explosion. Further reliable spatial-velocity estimates will enable refinement of this value. We also considered several methods for the estimation of the minimum masses of the main-sequence stars that are transformed at the end of their evolution into black holes or WR stars in close

binaries. This limiting mass was $\sim 25 \pm 5 M_\odot$. Within the remaining uncertainties, this value appears to be the same for black holes and WR stars.

Our analysis of X-ray close binaries with black holes and known component masses in Table 2 confirmed the validity of the previously found [28] distribution of the component mass ratio q_0 for forming close binaries ($dN \sim dq_0$) to values $q_0 \cong 0.04$. This value is comparable to the mass ratios of solar-type stars with massive planets ($\sim 0.01 M_\odot$). This may provide evidence that the massive planets around solar-type stars detected in recent years extend the family of close binaries to smaller mass ratios. Further study of this problem is needed, since the observed X-ray binaries with low-mass donors from Table 2 fill the mass interval for the companions of massive stars that is analogous to the "brown-dwarf desert" in extrasolar planetary systems.

We demonstrated the large role of observational selection effects in the analysis of the evolutionary status of WR + OB binaries and black holes in close binaries. The determining role of selection effects in many cases is widely known, but taking these into account when analyzing observational data has not become general practice.

An interesting property of WR + OB close binaries from Table 1 that have undergone either a conservative mass-transfer or a common-envelope phase is that they frequently display substantial orbital eccentricities, up to 0.6. For reasons that are currently unclear, the well-known mechanisms acting in semidetached cataclysmic and X-ray binaries, as well as in Algols with circular orbits, appear not to act in interacting massive binaries. One possible origin of this obvious difference is the short duration of the interacting phase in massive systems and the reduced viscosity of the radiative envelopes of the components, which prevent circularization of the orbits. This problem has been analyzed in [24] and deserves further study.

A comparison of the orbital periods of WR + OB stars and of WR stars in close binaries with one optical spectrum (Table 1) indicates that the average periods of the latter are substantially shorter. This is another obvious observational selection effect and testifies to the low masses of the secondaries, which are probably, as a rule, A or B components in binaries with one optical spectrum. The same is indicated by the small mass functions, which result in the estimates $M_2 \cong 2-20 M_\odot$. In other words, these systems fill the empty region in Fig. 2 with $M_V \lesssim 20 M_\odot$. Close binaries with black holes (Table 2) display even shorter orbital periods, again primarily due to observational selection effects. The lifetimes of wide X-ray binaries are close to the thermal timescales of their giant donors and are therefore short. The nuclear timescale for a massive main-sequence donor is also short. The X-ray stage is longest ($\sim 10^8$–10^9 yrs) when the donor is a solar-mass star, and the mass transfer is maintained by its magnetic stellar wind or the radiation of gravitation waves by the system [18]. It is obvious, that, as a rule, the orbital periods of these last systems are short. Consequently, the duration of the X-ray phase is a main factor determining the orbital-period distributions for X-ray binaries with accreting black holes.

The collapse of the core of a massive WR star in an extremely close system with a black-hole secondary inevitably results in the formation of a rapidly rotating Kerr black hole. This is a possible mechanism for gamma-ray bursts. The estimated rate of such events in the Galaxy is consistent with the observed rate of gamma-ray bursts, within the remaining (substantial) uncertainties in these quantities. It may be that the most likely observable progenitors of gamma-ray bursts are WO stars [35] in the closest systems, since precisely these are produced by the evolution of the most massive O stars [4]. This possibility requires further study. Note that the same path for the formation of young neutron stars with critical rotation rates is probably not possible, due to the large density of the degenerate cores of the pre-supernovae producing the neutron stars and the "large" radii of the neutron stars themselves.

5. ACKNOWLEDGMENTS

This study was supported by a Presidential Grant of the Russian Federation (00-15-96722), the "Astronomy" State Science and Technology Project, the Russian Foundation for Basic Research (project no. 02-02-17524), and the Program for Support of Leading Scientific Schools of Russia (00-15-96-553).

REFERENCES

1. E. P. J. van den Heuvel and J. Heize, Nat. Phys. Sci. **239**, 67 (1972).
2. A. V. Tutukov and L. R. Yungel'son, Nauchn. Inform. **27**, 70 (1973).
3. L. F. Smith, in *Wolf–Rayet and High Temperature Stars* (Buenos-Aires, 1971).
4. A. V. Tutukov and L. R. Yungel'son, Nauchn. Inform. **27**, 58 (1973).
5. A. M. Cherepashchuk, Astron. Zh. **78**, 145 (2001) [Astron. Rep. **45**, 120 (2001)].
6. G. E. Brown, A. Heger, N. Langer, *et al.*, New Astron. **6**, 457 (2001).
7. K. A. van der Hucht, B. Hidayat, A. G. Admiranto, *et al.*, Astron. Astrophys. **199**, 217 (1988).
8. A. E. Piatti, J. J. Claria, and M. G. Abachi, Astron. J. **110**, 2813 (1995).

9. A. V. Tutukov, L. R. Yungel'son, and A. Ya. Klyaĭman, Nauchn. Inform. **27**, 3 (1973).
10. B. Paczynski, Acta Astron. **16**, 231 (1966).
11. L. R. Yungel'son, Nauchn. Inform. **27**, 93 (1973).
12. A. V. Tutukov and L. R. Yungel'son, Acta Astron. **29**, 665 (1979).
13. P. S. Conti, Mem. Soc. R. Sci. Liege **9**, 193 (1976).
14. A. V. Tutukov and L. R. Yungel'son, Astron. Zh. **57**, 1266 (1980) [Sov. Astron. **24**, 729 (1980)].
15. P. S. Conti, in *O-stars and Wolf–Rayet Stars*, Ed. by P. Conti and A. Underhill (NASA, 1988).
16. A. Maeder, Astron. Astrophys. **173**, 247 (1987).
17. A. F. J. Moffat, in *IAU Symp. 163: Wolf–Rayet Stars: Binaries, Colliding Winds, Evolution*, Ed. by K. A. van der Hucht and P. M. Williams (Kluwer, Dordrecht, 1995), p. 213.
18. N. Langer, Astron. Astrophys. **171**, L1 (1987).
19. D. Schaerer, T. Contini, and D. Kunth, Astron. Astrophys. **341**, 399 (1999).
20. N. St-Louis, A. F. Moffat, L. Lapointe, *et al.*, Astrophys. J. **410**, 342 (1993).
21. R. Stothers, Astrophys. J. **568**, 312 (2002).
22. S. Mao and B. Paczynski, Astrophys. J. Lett. **388**, L45 (1992).
23. K. R. Lang, *Astrophysical Data: Planets and Stars* (Springer-Verlag, 1983).
24. V. G. Karetnikov and A. M. Cherepashuk, Astron. Zh. **80**, 42 (2003) [Astron. Rep. **47**, 38 (2003)].
25. A. V. Tutukov and A. V. Fedorova, Astron. Zh. **79** (2002) [Astron. Rep. **46**, 765 (2002)].
26. S. Balberg and S. Shapiro, Astrophys. J. **556**, 944 (2001).
27. T. E. Stepinski and D. C. Black, Astron. Astrophys. **356**, 903 (2000).
28. A. G. Masevich and A. V. Tutukov, *Stellar Evolution: Theory and Observation* [in Russian] (Nauka, Moscow, 1988).
29. H. J. Grimm, M. Gilfanov, and R. Sunyaev, Mon. Not. R. Astron. Soc. **339**, 793 (2003).
30. P. Massey, K. De Gioia-Eastwood, and E. Waterhouse, Astron. J. **121**, 1050 (2002).
31. L. Penny, D. Gies, T. Wise, *et al.*, Astrophys. J. **575**, 1050 (2002).
32. É. A. Antokhina and A. M. Chereashchuk, Pis'ma Astron. Zh. **14**, 252 (1988) [Sov. Astron. Lett. **14**, 105 (1988)].
33. P. Massey, E. Waterhouse, and K. De Gioia-Eastwood, Astron. J. **119**, 2214 (2000).
34. E. Berger, S. Kulkarni, and R. Chevalier, Astrophys. J. **577**, L5 (2002).
35. K. A. Postnov and A. M. Cherepashchuk, Astron. Zh. **78**, 602 (2001) [Astron. Rep. **45**, 517 (2001)].
36. S. Mc Breen, B. Mc Breen, F. Quilligan, and L. Hanlon, Astron. Astrophys. **385**, L19 (2002).
37. J. N. Reeves *et al.*, Nature **416**, 512 (2002).
38. K. Weiler, N. Panagia, and M. J. Montes, astro-ph/0205551.
39. W. Zhang, S. Woosley, and A. Mac Fadyen, Astrophys. J. **586**, 356 (2003).
40. A. Heger and S. Woosley, astro-ph/0206005.
41. M. Girardi, S. Borgani, G. Giuricin, *et al.*, Astrophys. J. **506**, 45 (1998).
42. B. F. Ronkema, G. A. Mamon, and S. Bajtlik, Astron. Astrophys. **382**, 397 (2002).
43. B. Paczynski, Astrophys. J. Lett. **494**, L45 (1998).
44. L. Wang, D. Baade, P. Hoeflich, *et al.*, astro-ph/0206386.
45. P. Meszaros and M. J. Rees, Astrophys. J. **397**, 570 (1992).
46. Y. F. Huang, Z. G. Dai, and J. Lu, Astron. Astrophys. **355**, L43 (2000).
47. N. R. Walborn, Astrophys. J. **205**, 419 (1976).
48. P. A. Crowther, D. J. Hillier, C. J. Ewans, *et al.*, Astrophys. J. **579**, 774 (2002).
49. T. A. Lozinskaya and A. V. Tutukov, Nauchn. Inform. **49**, 59 (1981).
50. A. M. Cherepashchuk and A. F. J. Moffat, Astrophys. J. Lett. **424**, L53 (1994).
51. V. S. Niemela, P. Massey, G. Testor, *et al.*, Mon. Not. R. Astron. Soc. **333**, 347 (2002).
52. M. Ribo, T. M. Paredes, G. E. Romero, *et al.*, Astron. Astrophys. **384**, 954 (2002).
53. Q. D. Wang, Astrophys. J. **453**, 783 (1995).
54. D. R. Gies, W. Huang, and M. V. McSwain, Astrophys. J. Lett. (in press); Astrophys. J. Lett. **578**, L67 (2002).
55. A. Gualandris, M. Colpi, and A. Possenti, astro-ph/0209394.
56. L. Kaper, A. Cameron, and O. Barziv, in *IAU Symp. 193: Wolf–Rayet Phenomena in Massive Stars and Starburst Galaxies*, Ed. by K. A. van der Hucht, G. Koenigsberger, and P. R. J. Eenens (Astron. Soc. Pac., San Francisco, 1999), p. 316.
57. K. A. van der Hucht, New Astron. Rev. **45**, 135 (2001).

Translated by K. Maslennikov

Astronomy Reports, Vol. 47, No. 5, 2003, pp. 401–412. Translated from Astronomicheskiĭ Zhurnal, Vol. 80, No. 5, 2003, pp. 436–448.

Population Synthesis of Rapidly Rotating Main-Sequence Stars with Companions

N. V. Raguzova

Sternberg Astronomical Institute, Moscow State University, Universitetskiĭ pr. 13, Moscow, 119992 Russia

Received May 15, 2000; in final form, November 27, 2002

Abstract—Using the "Scenario Machine" (a specialized numerical code for modeling the evolution of large ensembles of binary systems), we have studied the physical properties of rapidly rotating main-sequence binary stars (Be stars) with white-dwarf companions and their abundance in the Galaxy. The calculations are the first to take into account the cooling of the compact object and the effect of synchronization of the rotation on the evolution of Be stars in close binaries. The synchronization time scale can be shorter than the main-sequence lifetime of a Be star formed during the first mass transfer. This strongly influences the distribution of orbital periods for binary Be stars. In particular, it can explain the observed deficit of short-period Be binaries. According to our computations, the number of binary systems in the Galaxy containing a Be star and white dwarf is large: 70–80% of all Be stars in binaries should have degenerate dwarf companions. Based on our calculations, we conclude that the compact components in these systems have high surface temperatures. Despite their high surface temperatures, the detection of white dwarfs in such systems is hampered by the fact that the entire orbit of the white dwarf is embedded in the dense circumstellar envelope of the primary, and all the extreme-UV and soft X-ray emission of the compact object is absorbed by the Be star's envelope. It may be possible to detect the white dwarfs via observations of helium emission lines of Be stars of not very early spectral types. The ultraviolet continuum energies of these stars are not sufficient to produce helium line emission. We also discuss numerical results for Be stars with other evolved companions, such as helium stars and neutron stars, and suggest an explanation for the absence of Be–black-hole binaries.

1. INTRODUCTION

Be stars have attracted the attention of astronomers for many years. "Classical" Be stars are nonsupergiant stars of spectral type B that show or have sometimes shown Balmer emission lines in their spectra. Usually, these are H_α and H_β lines, while other lines are present only in absorption, probably because the excitation of hydrogen atoms to high levels occurs only in deep layers of the star. The presence of emission lines provides evidence for large regions of radiating gas with relatively or even very low optical depth at the stellar surface; these layers do not have a "base" of hot, dense gas that produces intense continuum radiation. All Be stars are rapid rotators; the H_α emission line is superimposed on a broad absorption line that indicates rotational velocities up to 500 km/s. However, Be stars with narrow absorption lines are also fairly common. It is evident that such stars are observed pole-on, and all rapid motions in the equatorial plane of the star occur in a plane perpendicular to the line of sight and therefore do not show up in the spectra. An excess of infrared (IR) radiation is also observed in Be stars and is especially prominent in the far IR. This is usually associated with free–free radiation of a hot, circumstellar envelope.

Be stars are believed to be rapidly rotating stars with circumstellar disks that tend to be strongly concentrated toward the equatorial plane. It is usually assumed that an ordinary stellar wind accelerated by radiation pressure acts in the polar region. The evolutionary status of Be stars and the mechanism for their formation remain incompletely understood. Here, we adhere to the "intrinsic" binarity hypothesis for Be stars; i.e., we suppose that these stars form in binary systems during the first mass transfer. This model for the formation of the disk-like envelopes of Be stars was suggested by Křiž and Harmanec [1] and further developed by Rappaport and van den Heuvel [2] for Be–X-ray binaries. In the model, a system containing a Be star with a helium companion is formed at the end of the mass-transfer phase. It is assumed that the initially more massive component of the system fills its Roche lobe in the hydrogen-shell burning stage; i.e., case B mass exchange in the classification of Kippenhahn and Weigert [3] is realized. Calculations of mass and angular-momentum transfer show that the formation of a rapidly rotating B star is then almost inevitable. Be stars formed in this way should have

1063-7729/03/4705-0401$24.00

an evolved companion, such as a helium star, white dwarf, neutron star, or black hole.

Thus far, only X-ray binaries containing Be stars and neutron stars have been detected. More than 50 such systems are known in our Galaxy and in the neighboring Magellanic Clouds. The ϕ Per system, which has recently been intensively studied, may be an example of a Be binary with a helium companion. It appears that the 59 Cyg system belongs to the same class. The absence of observed Be stars in pairs with white dwarfs must be explained, since the most recent computations [4] show that they should comprise almost 70% of all binaries with Be stars.

The formation of white dwarfs in pairs with Be stars, the expected number of such systems, and the possibility of their detection were discussed in [5–8]. Here, we perform population-synthesis computations of the number of binary Be stars with white-dwarf companions and their expected orbital and physical characteristics. These are the first such calculations that take into account the cooling of the compact object and the effect of tidal synchronization on the evolution of the Be star in the binary. We discuss the influence of various parameters of binary systems on the observational features of the white dwarf and possibilities for detecting this star. We also briefly discuss the properties of Be stars with other evolved companions—helium and neutron stars—and suggest an explanation for the lack of detections of Be stars in binaries with black holes.

All statistical computations were made using the "Scenario Machine" [9], a specialized numerical code developed in the Department of Relativistic Astrophysics of the Sternberg Astronomical Institute, designed to model the evolution of large ensembles of binary stars. A demonstration version of this code is available at the web site http://xray.sai.msu.ru/sciwork/scenario.html.

2. THE WHITE-DWARF COOLING PROBLEM

The problem of cooling is a key issue in studies of the evolution of white dwarfs. It is known that the dominant source of a white dwarf's luminosity is the thermal energy of ions stored in the stellar interior. In the formation and early cooling stages of the evolution of a white dwarf, an important role is played by neutrino losses. The theory of single white-dwarf cooling predicts a relation between a dwarf's luminosity and age, as is confirmed by observations. An approximate theory of white-dwarf cooling was developed independently by Kaplan [10] and Mestel [11]. In their model, a white dwarf has a radiative, nondegenerate envelope and an isothermal degenerate core. It is assumed that the pressures of the degenerate and nondegenerate electrons are equal at the interface of these regions.

We assume here that the overwhelming majority of white dwarfs were formed with hydrogen–helium envelopes [12]. It is known that the cooling times of white dwarfs are determined largely by the mass and chemical composition of their envelopes [13–15]. In our calculations, we used the time dependences of the luminosity derived by Althaus and Benvenuto [15] and Iben and Tutukov [13].

3. POPULATION-SYNTHESIS COMPUTATIONS OF THE NUMBER OF BINARY Be STARS WITH WHITE-DWARF COMPANIONS AND THEIR PHYSICAL PROPERTIES

3.1. Basic Principles of the Computations

The "Scenario Machine" code was first described by Kornilov and Lipunov [16]. Recently, a very detailed description of the code was published in the review by Lipunov *et al.* [9] and in [17]. The review [9] can also be found at http://xray.sai.msu.ru/~mystery/articles/review/. Therefore, we will describe here only the main principles of the code's operation and the parameters that are required for our computations.

The method for modeling the joint evolution of binary components is based on computing the evolution of a large number of binaries with a random set of initial parameters from the time of their formation to the present. The birth times of the binaries are assigned at random, as are the parameters of the systems, which are distributed in accordance with known empirical laws. Further, the model system evolves in accordance with the adopted evolutionary scenario. The continuous evolution of each component is considered as a sequence of a finite number of evolutionary states in which the stellar parameters become considerably different. Thus, the evolutionary stage of the binary can be defined as a combination of the states of the two components, which changes as soon as the more rapidly evolving component passes into the next stage. The stellar parameters and mass-loss rate are considered constant during each stage. Depending on the evolutionary stage, the state of the less rapidly evolving component may change or remain the same. We follow Webbink [18] in his interpretation of the regimes for the first mass exchange, since this takes into account the physical state of the star at the moment of Roche-lobe overflow in more detail than the classification introduced by Kippenhahn and Weigert [3].

As a rule, mass exchange in binary systems is not conservative, since, during the first mass exchange, the thermal time scale of the more massive star is

shorter than the thermal time scale of the secondary. In stages when one of the components overfills its Roche lobe, we allow for partially nonconservative mass exchange. We use the ratio of the mass gained by the accretor and the mass lost by the donor as a measure of this nonconservativeness.

To obtain statistically significant results, we computed the evolution of 10^6 binary systems. We considered binaries with initial primary masses from 2 to $120M_\odot$, distributed in accordance with a Salpeter initial mass function ($\alpha = 2.35$). The mass-ratio distribution was assumed to be "flat"; i.e., it was assumed that binaries with similar masses for both components occur as frequently as binaries with significantly different component masses. The initial semimajor axes of the binaries were taken from a logarithmically uniform distribution ranging from 10 to $10^7 R_\odot$. It was assumed that Be stars form in binary systems after a first mass exchange without the formation of a common envelope, with the donor transferring a large amount of angular momentum to the accretor. We took the masses of the Be stars to be in the range from 2.38 to $20M_\odot$ (in accordance with [19]). We assumed that the common-envelope stage did not occur if the initial component-mass ratio q exceeded 0.3. We took into account the various chemical compositions of white dwarfs (He, CO, or ONeMg white dwarfs). We also allowed for the fact that the masses of CO and ONeMg white dwarfs can increase to the Chandrasekhar mass in the course of their evolution, leading to the formation of a neutron star.

3.2. Computation Results: Properties of Binaries Containing Be Stars and White Dwarfs

The existence of white dwarfs in binary systems with Be stars is important for stellar-evolution theory. In contrast to single white dwarfs and similar objects in low-mass systems (cataclysmic variables, polars, etc.), white dwarfs in systems with Be stars must form from fairly massive stars. Indeed, the presence of a B component suggests that the primary was sufficiently massive to leave the main sequence earlier than its companion and evolve into a white dwarf. It is reasonable to suppose that the maximum of the distribution of masses of the white dwarfs in Be–white-dwarf systems should be strongly displaced toward larger masses, compared to the distribution for single white dwarfs and white dwarfs in low-mass binaries, where this maximum is at $0.57M_\odot$ [20]. This is confirmed by the results of our computations, shown in Fig. 1. The maximum of the distribution of white-dwarf masses is at $0.8–1.0M_\odot$. This peak is due to the large abundance of CO and ONeMg white dwarfs. A smaller peak at $0.3–0.4M_\odot$ is also visible, due to the large number of helium dwarfs in pairs with late-type Be stars. Another reason for the secondary maximum is the long lifetime of helium dwarfs.

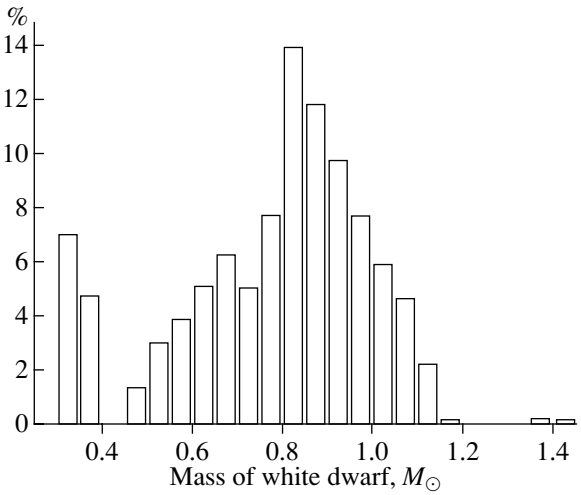

Fig. 1. Number of masses of the compact companion for Be stars with white-dwarf companions.

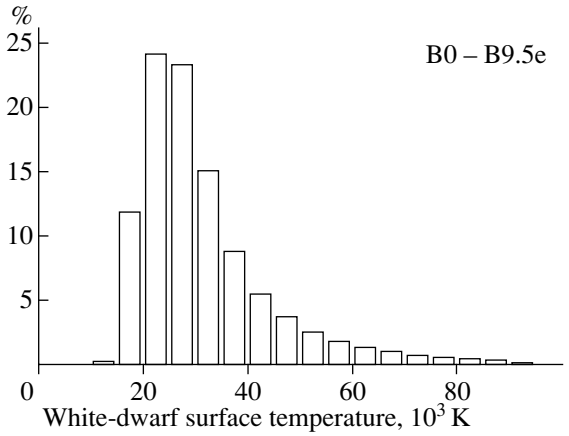

Fig. 2. Distribution of surface temperatures of the compact companion for Be stars with white-dwarf companion.

Figure 2 shows the expected distribution of white-dwarf surface temperatures for Be–white-dwarf systems. The initial temperature of the core was assumed to be 10^8 K, based on the observational estimate of the maximum surface temperatures of white dwarfs, $(9–9.5) \times 10^4$ K [16]. The computations show that, despite the large number of relatively long-lived, low-mass, late-type Be stars, the white-dwarf companions of Be stars do not cool completely during the lifetime of the Be primary. They have temperatures from 10^4 K to 9×10^4 K, with a maximum at $2–3 \times 10^4$ K. It is evident that the hottest white dwarfs should be observed in binaries with early-type Be stars. The distribution of white-dwarf surface temperatures for

early-type systems is shown in Fig. 3. Most of the white dwarfs in these systems have temperatures from 3×10^4 to 5×10^4 K. Based on these computation results, the detection of hard UV or soft X-ray emission from the hot surface of the white dwarf might represent one method for detecting these objects. However, as has already been shown, e.g., by Apparao [9], this approach is not always suitable, especially for very close systems. We shall discuss this problem below.

Let us consider the orbital parameters of the model Be binaries produced by our computations. Figure 4 shows the distributions of the orbital periods and semimajor axes. We can see that all the systems are fairly close, with periods shorter than 1–2 yrs. There is a deficit of systems with periods of 10–30 days. The absence of short-period X-ray binaries may be due to the effect of tidal synchronization of the rotation of the binary systems [21]. It is clear that the same effect is operating in the Be–white-dwarf systems. We take into account tidal synchronization following the theory of Tassoul [22], who suggested a purely hydrodynamical mechanism for the synchronization of the spin and orbital motions of the components of close binaries. This supposes a large-scale meridional flow superposed over the rotational motion of a tidally deformed binary component. These hydrodynamical flows cease to exist as soon as the motion is synchronized. The theory of Tassoul works well for binaries whose components are early-type stars with radiative envelopes. According to Tassoul [22] and Claret *et al.* [23], the synchronization time scale for low-eccentricity orbits is

$$\tau_{syn} = 5.35 \times 10^{3-N/4} \frac{1+q}{q} L^{-1/4} M^{5/4} R^{-3} P^{11/4}, \quad (1)$$

where the stellar mass M, luminosity L, and radius R are in solar units, the period P and $\tau_{\rm syn}$ are in days, and q is the component-mass ratio. The parameter N is related to various ways of transporting energy to the outer layers of the star. For stars whose envelopes are in radiative equilibrium, $N = N_r = 0$.

In the evolutionary computations, we must keep in mind that the time scale for synchronization may be shorter than the main-sequence lifetime of the Be star. This strongly influences the orbital-period distribution for binary Be stars. A critical orbital period for a Be binary can be obtained by equating the main-sequence lifetime of the Be star and the synchronization time. If the orbital period is shorter than the critical period, the Be star has enough time to synchronize its rotational and orbital motions. In this case, the Be phenomenon will disappear before the star leaves the main sequence. The deficit of short-period systems of Be stars with degenerate companions can be explained by this effect.

Note the absence of short-period systems among known binary Be stars. This remained unexplained for a long time, though the action of tidal interactions was suspected. This problem can be resolved by taking into account the effect of synchronization via the Tassoul mechanism on the evolution of Be stars in binary systems.

The semimajor orbital axes of most of the systems do not exceed $300R_\odot$. These systems have circular orbits, since the formation of a white dwarf does not require a supernova explosion. For the same reason, the equatorial plane of the Be star is coincident with the orbital plane. The observed sizes of the circumstellar disks of Be stars are from several tens to several thousands of stellar radii. Therefore, the white dwarfs are always embedded in the dense circumstellar matter surrounding the primary. As we shall show later, this seriously hampers detection of white-dwarf companions to Be stars.

Be stars can have degenerate companions with various chemical compositions. These companions are predominantly CO and ONe white dwarfs. Helium white dwarfs accompany Be stars of the latest spectral types. The evolutionary track resulting in the formation of a helium degenerate dwarf (Fig. 5) shows that, in the first mass exchange, the more massive star loses its envelope completely before helium ignition in its core. As a result, a hot naked core is exposed, which is almost entirely degenerate except for its outer layers. Nuclear reactions no longer occur in this core, and it cools and contracts, producing a helium white dwarf.

In more massive systems, the first mass transfer is interrupted when helium is ignited in the core of the Roche-lobe-filling star. These systems pass through a stage with a nondegenerate helium star and form predominantly Be stars in pairs with CO white dwarfs. The maximum initial mass of the primary, which is not able to ignite carbon in its core at the corresponding temperature, is $\sim 10M_\odot$. For initial masses exceeding this limit, carbon burning continues until the formation of a degenerate ONe core. This is the way in which systems with degenerate ONe dwarfs are formed.

As we can see from the scenario in Fig. 5, the main qualitative difference between the scenarios for the formation of He dwarfs and of more massive CO and ONe dwarfs is the absence of an intermediate stage with a nondegenerate helium star in the former case. The hot degenerate core left after the complete loss of the envelope due to mass transfer in a system that is not too massive cannot really be considered a

helium star, since nuclear reactions do not occur in its interior.

If the mass of the primary is $5.6{-}14M_\odot$, the helium star may fill its Roche lobe after the depletion of helium in its core. The relatively rare "BB" case [24] of mass exchange occurs. This can produce both CO and ONe white dwarfs.

4. BE STARS IN PAIRS WITH OTHER EVOLVED COMPANIONS

4.1. Be Stars with Helium Companions and their Possible Prototype ϕ Persei

Van der Linden [25] has suggested that Be stars can have helium companions. In the process of mass exchange in a binary system, the hydrogen envelope of the initially more massive component can be completely lost, leaving behind a hot naked core if the initial mass is $M \leq 2.5M_\odot$ or a nondegenerate helium star (Wolf–Rayet star) if $M > 10M_\odot$. The lifetime of the helium star is determined by the core helium burning time [26]. We have adopted the formulas for calculating these lifetimes from [18, 27].

The helium star can also fill its Roche lobe. This relatively rare case of mass transfer can occur only after depletion of helium in the stellar core and can begin either before or after the ignition of carbon in the core. In the case of helium stars with masses below the Chandrasekhar limit, this mass exchange produces a CO white dwarf with a companion that is still on or close to the main sequence. In relatively rare cases, for stars with initial masses $M > 10.3M_\odot$, an extended stage of carbon burning leads to the formation of a degenerate ONe core.

The distributions of the orbital parameters of Be stars with helium companions are shown in Fig. 6. We can see the same deficit of short-period systems, due to the effects of synchronization. Very long-period systems, with periods in excess of 2–3 yrs, are absent as well. This suggests that the secondaries in these systems are likewise virtually always embedded in the dense circumstellar envelope of the Be star. The distributions are similar to those for Be–white-dwarf systems. This is not a coincidence, since nothing that can significantly change the orbital period happens between the formation of the helium star and of the white dwarf. One exception may be the relatively rare occurrence of a stage in which the helium star overfills its Roche lobe, resulting in an increase in the orbital period.

One of the best candidate Be–helium-star systems is the long-period binary ϕ Per ($P_{orb} = 127$ day). The first evidence for this was provided by Poeckert [28], who obtained a radial-velocity curve for the HeII 4686 Å emission line and concluded that it is

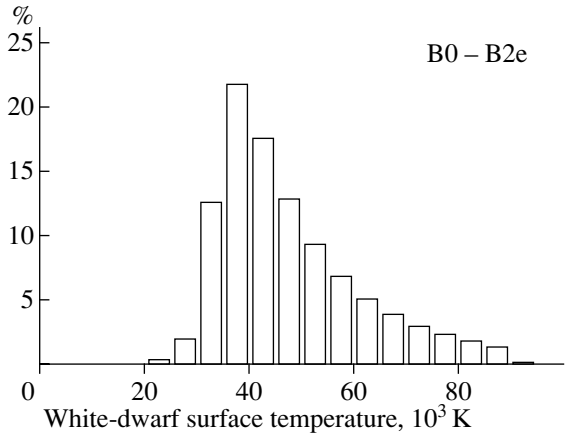

Fig. 3. Distribution of the surface temperature of the compact companion for early-type Be stars with white-dwarf companions.

formed in hot gas surrounding the companion. Since the ionization of helium requires a high temperature, Poeckert concluded that the companion must be a very hot star, possibly a remnant of the first mass exchange in the system. Gies *et al.* [29] analyzed the radial-velocity curve to derive the component masses: $9.3 \pm 0.3M_\odot$ for the Be star and $1.14 \pm 0.04M_\odot$ for the companion. The identification of this system has a large significance for stellar evolutionary theory, since it could confirm the intrinsic binarity of Be stars. It is interesting to consider the evolutionary track for a binary resulting in the formation of such a system, shown in Fig. 7; this track also includes evolutionary stages following the phase corresponding to a ϕ Per-type system. To obtain this track, we assumed completely conservative mass exchange in the system. This was necessary to obtain component masses in agreement with those determined by Gies *et al.* [29]. It is interesting that a system such as ϕ Per will never turn into a system with a Be star and white-dwarf, since the primary evolves into a giant while its companion is still a helium star.

4.2. Be Stars with Neutron-Star Companions: Massive X-ray Transient Binaries with Be Stars

We have discussed the properties of these systems in detail in [21], where we presented computations of evolutionary tracks for some observed X-ray binaries containing Be stars. A supernova explosion in a binary system will change the semimajor axis and eccentricity of the orbit, even if the explosion is spherically symmetric. If the explosion is weakly asymmetric, the nascent compact object (neutron star) obtains additional momentum, which substantially increases the eccentricity of the orbit. An anisotropic velocity ("kick") of no more than 50 km/s proved

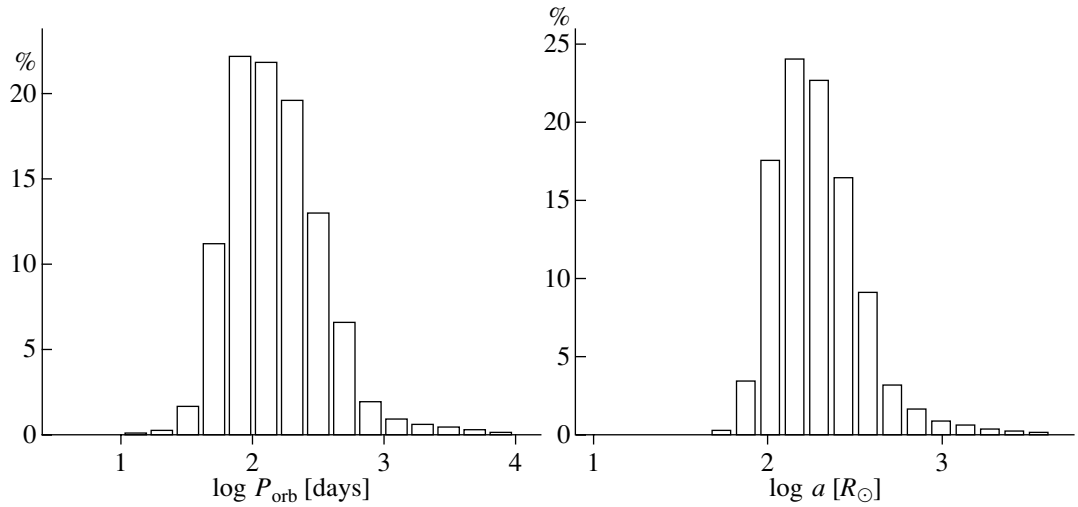

Fig. 4. Distributions of binary orbital parameters for Be stars with white dwarf-companions.

to be sufficient to obtain good agreement with the observed parameters of X-ray binaries. However, the possible anisotropy of the collapse cannot be neglected completely, since the peak of the distribution of orbital eccentricities for observed X-ray binaries containing Be stars is at 0.3–0.4, and there are some systems with $e > 0.8$ [21]. A velocity anisotropy of $w = 50$ km/s is sufficient to obtain eccentricities of 0.8–0.9 (see Fig. 8). With $w = 0$ km/s, our results are in clear disagreement with the observations. A deficit of systems with low orbital periods becomes apparent as well. Note that it was precisely the need to explain the absence of observed short-period X-ray binaries with Be stars that forced us in [21] to consider various processes influencing the parameters of binary systems and to conclude that the action of the tidal mechanism suggested by Tassoul may be the main reason for the absence of these systems.

4.3. Black Holes in Binaries with Be Stars

Thus far, no Be–black-hole binary has been detected. The Be stars in such systems must be more massive than those in Be–neutron-star binaries, since the black-hole progenitor must be a massive star itself, and the formation of a common envelope in the first mass exchange due to the large component-mass ratio may prevent the formation of a Be star. An evolutionary track resulting in the formation of a black hole in a pair with a Be star is given in [30]. In that case, the mass of the nondegenerate component was $\sim 20M_\odot$, which corresponds to spectral type O8–O9.

The absence of Be–black-hole binaries could be related, for instance, to the existence of some intermediate evolutionary stage that prevents the formation of the Be star. One candidate could be the luminous blue supergiant variable (LBV) stage, which is identified with the phase of hydrogen shell burning in a star with an initial mass greater than $\sim 50M_\odot$ [31]. The mass-loss rate via the stellar wind of such a star can be as high as 10^{-4}–$10^{-5}M_\odot$/yr. This is sufficient to prevent the further expansion of the star [32, 33]. Recently, Vanbeveren *et al.* [34] have suggested another scenario for the evolution of very massive binary stars, in which components with initial masses greater than 40–$50M_\odot$ evolving through the LBV stage have such high stellar-wind mass-loss rates that Roche-lobe overflow is prevented.

An observational lower limit for the initial masses of black-hole progenitors of $\geq 50M_\odot$ was suggested by Kaper *et al.* [35], based on new lower limits for the mass of the supergiant WRAY 977, a component of the binary X-ray pulsar GX 301-2. Since the initial mass of the black-hole progenitor certainly fits in the range of stellar masses for which the LBV stage is inevitable, the formation of a Be star in such a massive system seems impossible. For a Be star to form in a binary, the primary must fill its Roche lobe and transfer enough angular momentum to the secondary to spin it up to the critical rotation rate. In the LBV stage, the mass loss by the donor is spherically symmetric, and the secondary does not gain enough angular momentum to bring about critical rotation and the formation of a disk, so that a Be star does not form.

5. DISCUSSION

Our computations have shown that the number of binary systems with Be stars and white-dwarf companions is large: 78% of all Be stars formed in binaries should have white-dwarf companions. Nineteen

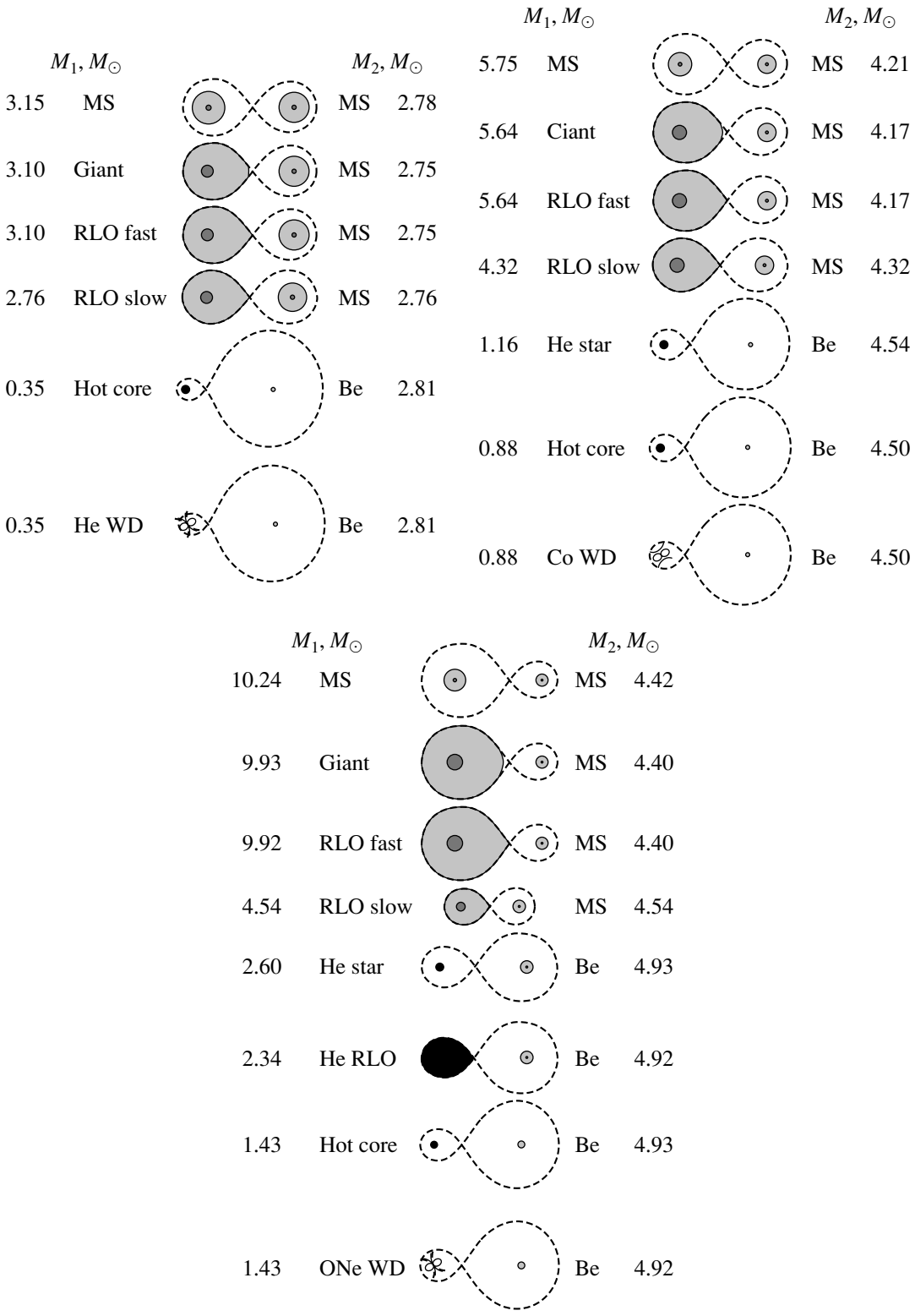

Fig. 5. Scenario for formation of Be stars with white-dwarf companions with various chemical compositions. MS refers to a main-sequence star, Be to a Be star, Giant to an evolved giant not filling its Roche lobe, RLO to a star filling its Roche lobe ("RLO fast" corresponds to mass transfer on the thermal time scale, and "RLO slow" to slow mass transfer on the nuclear-burning time scale), He star to a helium star, He RLO to a helium star filling its Roche lobe, Hot core to the naked core of a star that is a remnant of the first mass transfer, which becomes a white dwarf (WD) after it cool. All numerical data refer to the beginning of the corresponding evolutionary stage.

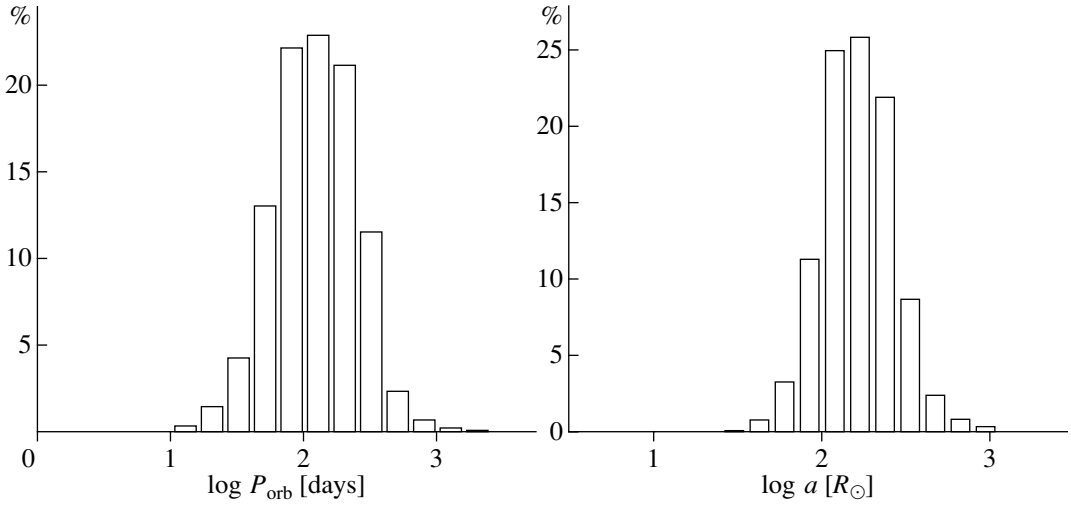

Fig. 6. Distributions of orbital parameters for Be stars with helium-star companions.

$M_1, M_\odot$			$M_2, M_\odot$	$a, R_\odot$	T, 10^6 yrs
5.56	MS	MS	5.07	33.00	0.00
5.45	Giant	MS	4.99	33.58	68.67
5.45	RLO fast	MS	4.99	33.59	68.81
5.22	RLO slow	MS	5.22	33.46	68.82
1.10	He star (Per-like system)	Be	9.34	232.40	69.15
0.87	He star	Giant	8.74	252.40	82.65
0.87	Hot core	Giant	8.72	252.50	83.58
0.87	WD	Giant	8.72	252.50	83.67

Fig. 7. Evolutionary track for the formation of a ϕ Per-like system. Notation is as in Fig. 5.

percent of Be binaries have hot subdwarf components (helium stars, in our classification), and only 3% are Be–X-ray binaries (systems with neutron-star components). Our results are quantitatively similar to those of van Bever and Vanbeveren [4], who found similar percentages of systems of various types based on statistical calculations (70, 20, and 10%, respectively). Our computations assumed that the distribution of the component-mass ratio was flat; i.e., systems whose components have similar masses occur as frequently as those whose components have appreciably unequal masses. To facilitate comparison of our results with those of Waters *et al.* [5], who were the first to consider Be stars with helium and white-dwarf companions, and to investigate the influence of the initial component-mass distribution, we made additional computations in which we assumed an initial mass-ratio distribution $f(q) \propto q^{-1}$

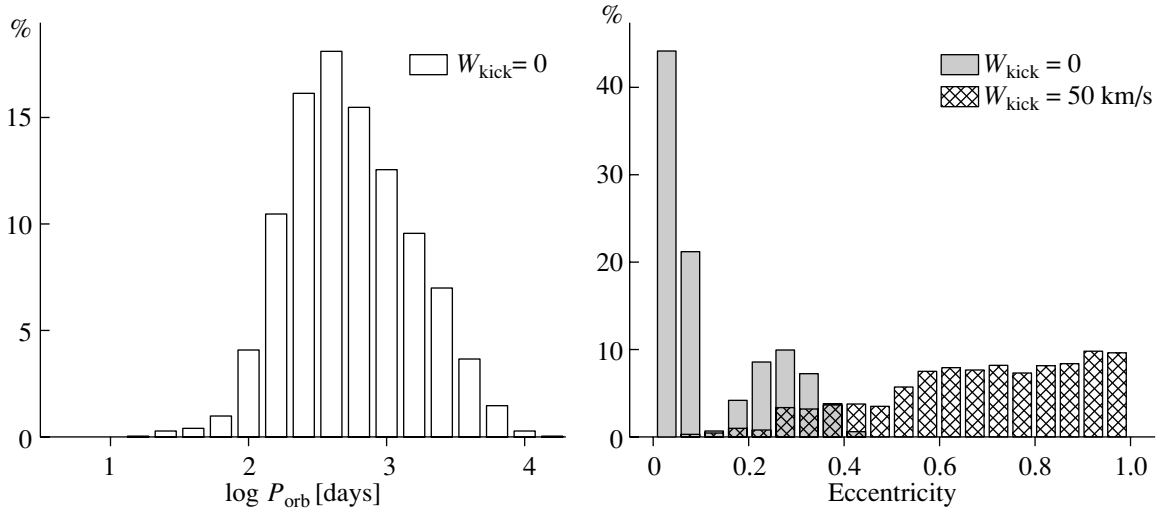

Fig. 8. Distributions of orbital parameters for Be stars with neutron-star companions.

for $q = M_2/M_1 < 1$, as in [5]. The results are listed in the table. We can see that our computations produce many fewer systems with helium components than obtained in [5], while, on the contrary, systems with white dwarfs dominate. The difference between our results and those of [5] can be explained by the following.

(1) We have used new estimates for the lifetimes of helium stars (this appears to be the dominant factor explaining the lower number of systems with helium components).

(2) Our computations took into account the fact that, as a rule, the first mass exchange is nonconservative, since the more massive star has a shorter thermal time scale. This factor can be used to compute the accretion rate and the fraction of the mass lost by the donor that is lost from the system. In their estimates of the numbers of Be stars with various types of companions, Waters *et al.* [5] considered this fraction to be constant and equal to 0.3.

(3) We took into consideration the effect of tidal synchronization on the evolution of a Be star in a close binary system.

The tabulated numbers of Be stars with various companions also show that the percentage of systems with various companions changes if the initial distribution of component-mass ratios is not flat. It is evident that comparable initial component masses are necessary for scenarios in which Be stars have white-dwarf companions. This is precisely why the fraction of Be stars with white-dwarf companions among all Be stars decreased for the distribution $f(q) \propto q^{-1}$, which has a larger fraction of stars with initial $q < 1$ than the flat mass distribution. However, our main conclusion is not changed: among binary systems with Be stars that are formed as a result of the first mass transfer, systems with high surface-temperature white dwarfs must be dominant.

Despite the theoretical predictions, no Be–white-dwarf systems have been detected thus far (the existence of a degenerate component in the γ Cas system, which is the first Be star discovered and was long considered a candidate Be–white-dwarf system, is currently strongly doubted; see, e.g., [36–39]). At the same time, more than 30 Be–X-ray binaries are known in the Galaxy, while this is the least expected type of Be system in our model! If most Be stars form in binaries (as is supported, for instance, by the existence of Be–X-ray-transient binaries), then the deficit of white dwarfs in pairs with Be stars must be explained, and the selection effects preventing the detection of these binaries must be identified.

Three systems containing a white dwarf and a massive optical component are known—y Pup, θ Hya, and 16 Dra [40–42]. The optical components of these systems do not display atmospheric activity and are not Be stars, although they have spectral type B (B5 Vp, B9.5 V, and B9.5 V, respectively). The white dwarfs in these systems were discovered in the extreme ultraviolet (from EUVE observations) via their high surface temperatures ($3–4 \times 10^4$ K). Our computations show that white-dwarf companions to Be stars must be hot (see Figs. 2, 3). This raises the question of whether such a white dwarf could be detected via its hard ultraviolet continuum, at wavelengths shorter than 1000 Å, where the main component is no longer the main source of radiation. This is how these three systems with B stars were detected. Unfortunately, the answer to this question is probably negative, as follows from a more detailed consideration of the conditions under which a white dwarf in a binary with a Be star exists. First, our

Estimates of numbers of binary Be stars

Parameter of the distribution	$\alpha_1 = 0$	$\alpha_q = -1$	Paper [5]
Be stars among all binaries with B components	6%	13%	5%
Be stars with white-dwarf companions among all binaries with Be components	78%	73.3%	22.6%
Among them:			
Be star + ONe dwarf	35%	30%	
Be star + CO dwarf	58%	59%	
Be star + He dwarf	7%	11%	
Be stars with helium-star companions among all binaries with Be components	19%	24.3%	75.1%
Be stars with neutron-star companions among all binaries with Be components	3%	2.4%	2.3%

computations show that the dwarf is essentially always embedded in the dense circumstellar disk of the main component. Therefore, in addition to being hot, it will accrete material. X-ray observations of cataclysmic variables with accreting white dwarfs show that their spectra have a black-body component with a temperature of about 40 eV and a harder component with a kT of several keV. The bulk of the energy is radiated by the black-body component. The presence of a massive optical star with an equatorial disk fundamentally changes the conditions for the manifestation of a white dwarf in a close binary. The reason for this is that all hard ultraviolet and soft X-ray photons are absorbed in the gaseous envelope of the Be star. Calculations for the disk of a Be star with a radial size of 10^{12}–10^{13} cm and a density of 10^{10}–10^{12} atoms/cm^2 carried out by Apparao [8] led him to conclude that the hydrogen column density was sufficient to absorb all hard photons. The orbital periods of the systems we are considering are certainly within the range of the calculations of Apparao [8]. Therefore, the possibility of observing the hard ultraviolet continuum emission of a white dwarf in a pair with a Be star is of little practical use.

Some optimism may be warranted about the idea that a region of ionized hydrogen (HII zone) should arise due to the absorption of the hard radiation of the companion; this zone would radiate both optical line and continuum emission. It is known that Be stars ionize their own circumstellar disks, which contain mainly hydrogen. The Lyman continuum of the star can ionize hydrogen and, after recombination, cascade transitions producing the observed spectral line occur. In such a system, the white dwarf would act as an additional source of ionization of the circumstellar disk of the Be star. Apparao [8] showed that, if the hard ultraviolet luminosity of the white dwarf is 4×10^{36} erg/s, this forms an HII zone with a luminosity of $L = 1.6 \times 10^{35}$ erg/s in the H_α line and $L = 2.7 \times 10^{34}$ erg/s in the continuum. Apparao [8] calculated the change in the stellar magnitude of the Be-star binary due to the presence of the accreting white dwarf and concluded that the increased luminosity in the H_α line and the continuum will exceed the luminosity variations due to ionization by the Lyman continuum only for stars of spectral types later than B1. If a white dwarf is accreting from the stellar wind of a Be star, its X-ray luminosity should be in the range 10^{32}–10^{36} erg/s. Therefore, the calculations of Apparao [8] give only the maximum variation of the optical luminosity of the Be star due to the presence of the compact companion. In practice, these variations may be much smaller than those calculated for $L_{uv} = 4 \times 10^{36}$ erg/s; the detection of such fluctuations will be much more difficult, especially since the nonstationarity of the Be-star envelope also contributes to the star's variability.

The strongest evidence for the possible presence of hot, compact companions (and nondegenerate helium stars) in the systems considered is the discovery of λ5876 and λ10 830 HeI emission lines in the spectra of some Be stars. Apparao and Tarafdar [43] have shown that the energy emitted by these stars in the hard ultraviolet continuum above the ionization potential for HeI is not sufficient to give rise to these lines, which can form only in stars earlier than B1. An additional source of ionization energy

is required to explain the observed emission in later-type stars. Apparao and Tarafdar [43] have shown that the HeI emission can be explained by the formation of a Strömgren zone by the X-ray and hard ultraviolet emission of the compact accreting component. Be stars sometimes throw off their disklike envelopes, becoming transformed into ordinary main-sequence B stars. The newly formed envelope will expand, but, during some time, helium emission lines will be not observed, while H_α emission will already be present. The helium lines will appear when the envelope reaches the compact component. Simultaneously, increased emission in the H_α line and continuum should be observed. This provides a means for detecting a hot degenerate companion to a Be star. However, Be stars do not throw off their envelopes frequently, and this effect is not observed in all Be stars.

The study of helium emission lines seems to be the most promising means of spectroscopic detection of nondegenerate helium-star and white-dwarf companions to Be stars (recall ϕ Persei). The component-mass ratios in post-first-mass-transfer Be binaries are small (~ 0.1–0.3), while their orbital periods exceed 30 days. This results in very small radial-velocity variations in Be spectra. For example, a $5M_\odot$ Be star with a 0.5–$1.0M_\odot$ companion would have a radial-velocity semiamplitude of $K/\sin i < 10$–20 km/s for orbital periods greater than 30 days. It is difficult to detect such small radial-velocity variations in the spectra of Be stars, since the stars have strong intrinsic variability and broadened spectral lines, which limits the effective spectral resolution to $\simeq 10$ km/s. However, the presence of helium emission could enable the detection of a hot white dwarf or helium companion. Radial-velocity variations of the helium lines could, indeed, be observable. For instance, the helium-line radial-velocity semiamplitude expected for a $5M_\odot$ Be star with a $1.0M_\odot$ companion is $K/\sin i > 70$ km/s for orbital periods < 100 days.

6. CONCLUSION

In spite of our conclusion that there should be a large number of Be stars with white-dwarf companions, selection effects limit possibilities for their detection. The loss of a Be star's disklike envelope is a rare event that is observed in far from all Be stars. Therefore, the detection of the white dwarf via its hard radiation during the transient absence of the circumstellar disk surrounding the main component is difficult. A good opportunity for detecting white-dwarf and helium-star companions may be provided by studies of helium emission lines of Be stars of not too early spectral types; the energy radiated by these stars in the hard ultraviolet continuum above the ionization potential of helium is not sufficient to form helium emission lines. The companions in such systems must have a high surface temperature. Our computations show that the white dwarfs in such systems do not have enough time to cool appreciably during the lifetime of the Be star. This gives rise to some optimism for the detection of Be stars with compact companions in the future.

7. ACKNOWLEDGMENTS

The author is grateful to V.M. Lipunov, K.A. Postnov, M.E. Prokhorov, A.V. Tutukov, and S.N. Nazin for useful discussions and remarks. This work was partially supported by the Russian Foundation for Basic Research (project no. 00-02-17164) and "Universities of Russia" (grant no. 5559). The author thanks the anonymous referee for valuable comments that helped to significantly improve the manuscript.

REFERENCES

1. S. Kříž and P. Harmanec, Bull. Astron. Inst. Czech. **26**, 65 (1975).
2. S. A. Rappaport and E. P. G. van den Heuvel, in *IAU Symp. 98: Be stars*, Ed. by M. Jaschek and H. G. Groth (D. Reidel, Dordrecht, 1982), p. 327.
3. R. Kippenhahn and A. Weigert, Z. Astrophys. **67**, 251 (1967).
4. J. van Bever and D. Vanbeveren, Astron. Astrophys. **322**, 116 (1997).
5. L. B. F. M. Waters, O. R. Pols, S. J. Mogeveen, *et al.*, Astron. Astrophys. **220**, L1 (1989).
6. O. R. Pols, J. Cote, L. B. F. M. Waters, *et al.*, Astron. Astrophys. **241**, 419 (1991).
7. S. F. Portegies Zwart, Astron. Astrophys. **296**, 691 (1995).
8. K. M. V. Apparao, Astron. Astrophys. **248**, 139 (1991).
9. V. M. Lipunov, K. A. Postnov, and M. E. Prokhorov, Astrophys. Space Sci. Rev. **17**, 1 (1996).
10. S. A. Kaplan, Astron. Zh. **27**, 31 (1950).
11. L. Mestel, Mon. Not. R. Astron. Soc. **112**, 583 (1952).
12. T. Driebe, D. Schönberner, T. Blöcker, *et al.*, Astron. Astrophys. **339**, 123 (1998).
13. I. Jr. Iben and A. V. Tutukov, Astrophys. J. **282**, 615 (1984).
14. B. M. S. Hansen and E. S. Phinney, Mon. Not. R. Astron. Soc. **294**, 557 (1998).
15. L. G. Althaus and O. G. Benvenuto, Astrophys. J. **477**, 313 (1997).
16. V. T. Kornilov and V. M. Lipunov, Astron. Zh. **60**, 284 (1983) [Sov. Astron. **27**, 163 (1983)].
17. V. M. Lipunov, K. A. Postnov, and M. E. Prokhorov, Astron. Astrophys. **310**, 489 (1996).
18. R. F. Webbink, in *IAU Symp. 53: White Dwarfs and Variable Degenerate Stars*, Ed. by H. M. van Horn and V. Weidemann (Cambridge Univ. Press, Cambridge, 1979), p. 426.

19. P. Harmanec, Bull. Astron. Inst. Czech. **39**, 329 (1988).
20. D. S. Finley, D. Koester, and G. Basri, Astrophys. J. **488**, 375 (1997).
21. N. V. Raguzova and V. M. Lipunov, Astron. Astrophys. **340**, 85 (1998).
22. J. L. Tassoul, Astrophys. J. **322**, 856 (1987).
23. A. Claret, A. Gimenez, and N. C. S. Cunha, Astron. Astrophys. **299**, 724 (1995).
24. A. J. Delgado and H.-C. Thomas, Astron. Astrophys. **96**, 142 (1981).
25. T. J. van der Linden, Astron. Astrophys. **178**, 170 (1987).
26. I. Iben, Jr. and A. V. Tutukov, Astrophys. J., Suppl. Ser. **58**, 661 (1985).
27. I. Iben, Jr. and A. V. Tutukov, Astrophys. J. **313**, 727 (1987).
28. R. Poeckert, Publ. Astron. Soc. Pac. **93**, 297 (1981).
29. D. R. Gies, W. G. Bagnuolo, E. C. Ferrara, *et al.*, Astrophys. J. **493**, 440 (1998).
30. N. V. Raguzova and V. M. Lipunov, Astron. Astrophys. **349**, 505 (1999).
31. R. Humphreys, in *IAU Symp. 143: WR Stars and Interrelations With Other Massive Stars in Galaxies*, Ed. by K. A. van der Hucht and B. Hidayat (Kluwer Acad., Dordrecht, 1991), p. 485.
32. A. Maeder, Astron. Astrophys. **120**, 113 (1983).
33. D. Vanbeveren, Astron. Astrophys. **182**, 207 (1987).
34. D. Vanbeveren, E. de Donder, J. van Bever, *et al.*, New Astron. **3**, 443 (1998).
35. L. Kaper, Astron. Astrophys. **300**, 446 (1995).
36. M. A. Smith, R. D. Robinson, and R. H. D. Corbet, Astrophys. J. **503**, 877 (1998).
37. M. A. Smith, R. D. Robinson, and A. P. Hatzes, Astrophys. J. **507**, 945 (1998).
38. M. A. Smith and R. D. Robinson, Astrophys. J. **517**, 866 (1999).
39. R. D. Robinson and M. A. Smith, Astrophys. J. **540**, 474 (2000).
40. M. R. Burleigh and M. A. Barstow, Mon. Not. R. Astron. Soc. **295**, 15 (1998).
41. M. R. Burleigh and M. A. Barstow, Astron. Astrophys. **341**, 795 (1999).
42. M. R. Burleigh and M. A. Barstow, Astron. Astrophys. **359**, 977 (2000).
43. K. M. V. Apparao and S. P. Tarafdar, Astrophys. J. **420**, 803 (1994).

Translated by L. Yungel'son

Astronomy Reports, Vol. 47, No. 5, 2003, pp. 413–421. Translated from Astronomicheskiĭ Zhurnal, Vol. 80, No. 5, 2003, pp. 449–457.

The Radio Pulsar J0205+6449 in the Supernova Remnant 3C 58

V. M. Malofeev, I. F. Malov, O. I. Malov, and A. P. Glushak

Pushchino Radio Astronomy Observatory, Astro Space Center, Lebedev Physical Institute, Russian Academy of Sciences, Pushchino, Moscow oblast, 142290 Russia

Received February 19, 2002; in final form, November 27, 2002

Abstract—The detection of pulsed radio emission from the recently discovered X-ray pulsar J0205+6449 in the young supernova remnant 3C 58 is reported together with the results of first studies of this emission. The observations were carried out at 111 and 88 MHz on radio telescopes of the Pushchino Observatory. The pulsar period, 65.68 ms, and period derivative, $\dot{P} = 1.9 \times 10^{-13}$, have been confirmed. The integrated pulse profile at 111 MHz has been obtained and the flux density and spectral index $\alpha = 2.8$ measured. The pulsar dispersion measure DM = 141 pc cm^{-3} has been confirmed. This dispersion measure yields a distance to the pulsar of $d = 6.4$ kpc, a factor of two or more greater than the previously favored distance to the supernova remnant 3C 58 (2.6 kpc). The problem of the age and distance of the pulsar–SNR system is discussed. If the age of the pulsar J0205+6449 is equal to that of the SNR (820 years), this pulsar is the youngest known radio pulsar. The synchrotron mechanism for the radio and X-ray emission is proposed to explain the lower radio and X-ray luminosity of this new pulsar compared to the Crab pulsar, which is similar to it in many ways. Optical emission with luminosity $L_{opt} = 10^{31}$ erg/s and gamma-ray emission with $L_\gamma = 7 \times 10^{35}$ erg/s are predicted, and the steep radio spectrum ($\alpha \approx 3$) can be explained.

1. INTRODUCTION

The search for pulsars in known supernova remnants (SNRs) began almost immediately after their discovery and became especially intense after the detection of a pulsar with the very short period of 33 ms at the center of the Crab Nebula [1]. In spite of the fact that modern scenarios for the formation of pulsars from low-mass supernova precursors predict the appearance of short-period pulsars in SNRs, until recently, only a few pulsars could confidently be associated with SNRs [2, 3]. In recent years, two groups of pulsars have been detected in hard X-rays (see, for example, [4]): Anomalous X-ray Pulsars (AXPs) and Soft Gamma-ray Repeaters (SGRs), almost half of which are in SNRs [4]. Although these objects may be young, they have long rotational periods (from 5 to 11 s) and therefore do not fit into a picture in which short-period pulsars are formed in young systems such as the Crab Nebula. It is possible that a different energy source operates in them, such as a superstrong magnetic field; Thompson and Duncan [5] have even proposed the special term "magnetar" for such objects. With the launch of the RXTE and Chandra X-ray observatories, it is now becoming possible to detect more radiating objects at the centers of SNRs. For instance, the youngest known pulsar, with an age of 700 years, has recently been detected in the SNR Kes 75 [6]. Counting AXPs, SGRs, and new pulsars, the number of candidates for genetically related SNR–pulsar systems has grown to more than 40 in the last two years [7].

Even so, any new object detected in a SNR is of special interest, since it provides opportunities for studies of the evolution of young neutron stars and for obtaining independent estimates of the object's age and distance, based on the time of the supernova and methods for determination the distances of SNRs.

At the end of August 2001, Murray *et al.* [8] reported the detection of an X-ray pulsar with a period of 65.68 ms in the SNR 3C 58, in the direction toward its central X-ray source, which was discovered in 1982 [9]. 3C 58 is classified as a plerion SNR and is similar to the Crab Nebula in many ways. Estimates of the distance to the SNR based on observations of two HI absorption features range from 1.5–3 kpc [10] to more than 6.5 kpc [11] for a distance to the center of the Galaxy of 8.5 kpc. At present, the distance 2.6 kpc [12] is used most frequently in the literature. The distance to the Crab pulsar (PSR B0531+21) is 2 kpc [13]. It is supposed that 3C 58 originated from SN 1181 CE 820 years ago [14]. This age is close to that of the Crab Nebula, 948 years. The angular sizes of the two remnants in the radio are similar, and, taking into account their distances, their physical sizes are also nearly equal. An important distinction between the two systems (SNR + pulsar) is the large difference in the X-ray luminosities of the two nebulas

1063-7729/03/4705-0413$24.00

and pulsars. The X-ray luminosities of the Crab Nebula and pulsar are 1000 times and 6000 times higher than those of 3C 58 and PSR J0205+6449. The radio luminosity of the Crab Nebula is a factor of ten higher than the radio luminosity of 3C 58. Interest in the new pulsar in 3C 58 will be especially high if it proves to be a strange, rather than a neutron, star [15].

Supposing that young pulsars in SNRs could have steep radio spectra (for PSR B0531+21 $\alpha = 2.8$ [16]), we have included a number of SNRs in our pulsar-search program using the sensitive Pushchino Large Phased Array (LPA) at 111 MHz. Application of the FFT-based search program [17] yielded no source detection toward 3C 58, except for a few suspected cases of a faint periodic signal at several Fourier frequencies.

With the detection of the X-ray pulsar PSR J0205+6449 in 3C 58 [8], the period, period derivative, and precise position of the pulsar were measured: $P = 0.06567895(1)$ s, $\dot{P} = 1.935(2) \times 10^{-13}$ s/s (MJD = 51901.330), RA = $02^{\rm h}05^{\rm m}37.^{\rm s}8$, DEC = $+64°49'41''$ (2000). Using these data and our well-established technique for detecting pulsed signals (applied, for example, to measure the fluxes of 235 northern pulsars [18]), we were able to detect faint periodic emission from PSR J0205+6449 at 111 MHz and later at 88 MHz [19]. More recently (in January 2002) Ranson [20] confirmed the presence of an X-ray pulsar with a period of 65.6 ms in 3C 58. While our paper was in preparation, Camilo *et al.* [21], knowing about our results, detected PSR J0205+6449 at 820 and 1375 MHz, enabling us to estimate its spectral index, $\alpha = 2.8$. Here, we present the results of our observations and discuss the age, distance, and emission mechanism of the pulsar J0205+6449 (PSR J0205).

2. OBSERVATIONS

We began a standard program of observations for the integration of a signal with a known period on September 10, 2001, and they have continued since then in sessions of one or two weeks per month. We present here data obtained up until August 11, 2002 (a total of 80 days). The main observations were carried out on the LPA in Pushchino (Lebedev Institute of Physics, Russian Academy of Sciences), which operates at 110.6 ± 1.3 MHz and has an effective area of $\sim 20\,000$ m^2. On eight days, observations were carried out in parallel on the LPA and at 87.746 MHz on the east–west track of the DKR-1000 radio telescope, which has an effective area of 5000–8000 m^2. Both radio telescopes are meridian instruments, and the observation durations were 7.5 min for the LPA and 22.1 min for the DKR-1000.

At both frequencies, the receiver was a filter-bank spectrum analyzer with a channel bandwidth of 20 kHz and either 32 or 64 channels. The sampling interval was 2.5600 or 2.2016 ms, and the receiver time constant was 3 ms. To ensure reliable recording of the pulsar pulses, all observations were carried out over six (LPA) or ten (DKR-1000) pulsar periods (i.e., $P_{\rm obs} = 0.066$ s $\times$ 6 or $P_{\rm obs} = 0.066$ s $\times$ 10). We developed this group-recording technique during observations of millisecond pulsars oriented at flux measurements at 102.5 and 111 MHz [18], as well as studies of the Geminga-pulsar profile [22]. This approach yields an additional criterion for the detection of a weak periodic signal when the integrated recording contains up to six (ten) pulses separated in time by the pulsar period. The observation and data-reduction techniques are described in more detail in our paper on flux-density measurements for 235 pulsars at 102.5 MHz [18]. We add here only that some of the observations were carried out with a calibration signal to enable referencing to discrete sources with known fluxes. Our pulsar complex enables the synchronous recording and storage of pulsar pulses with the computed period together with the start time, while preserving the pulse arrival phase, thanks to the high-precision time service of the Pushchino Radio Astronomy Observatory [23]. When processing the data, in addition to the standard procedures (baseline subtraction, equalization of the amplification in individual channels, summation over channels applying a dedispersion delay), we used an original method for rejecting channels with interference based on two criteria: the noise variance and the ratio of the calibration signals in the current and reference channels [18].

3. RESULTS

The first days of observations taking into account the known period and period derivative already showed a weak periodic pulsed radio signal. Figure 1 presents examples of the integrated profile of PSR J0205 at 111.23 MHz from observations of the best four days, which have signal-to-noise ratios from 5 to 10 and fluxes a factor of a few higher than the mean level. In addition to the integrated profile, we were able to detect a sequence of five pulses in a group with a duration equal to four periods when the signals for 4580 such groups were summed over four days (Fig. 2a). The phase tie during the summations for individual days was realized using the precomputed period and period derivative based on the X-ray data [8] and the observing epoch. Figure 2b shows the integrated profile for the same four days, obtained by summing 18 320 pulsar periods. In all the figures, we increased the signal-to-noise ratio by averaging

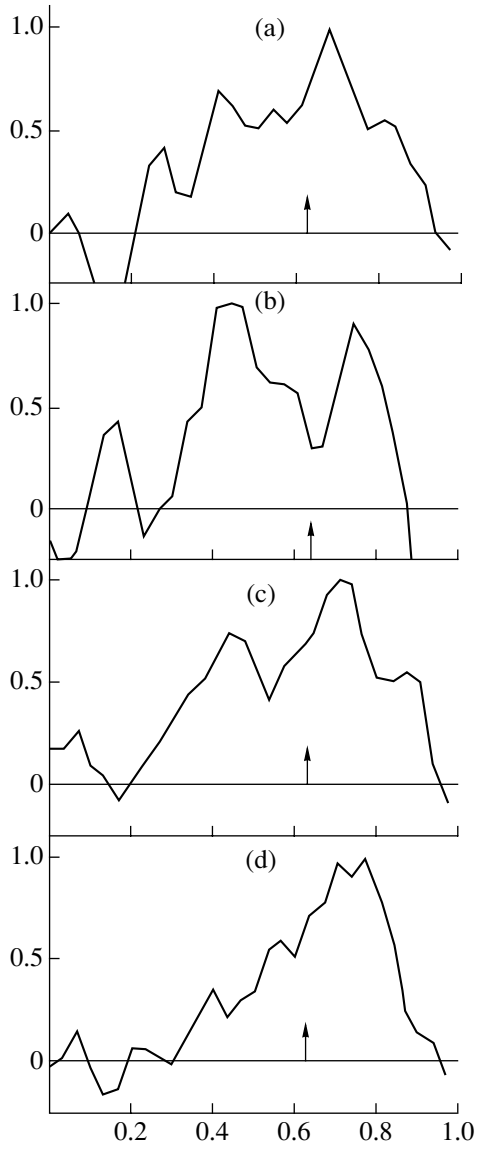

Fig. 1. Sample integrated profiles of PSR J0205+6449 for four days of observations: (a) August 1, 2002; (b) August 2, 2002; (c) August 3, 2002; and (d) August 5, 2002. On all four days, the observations were carried out at 111.23 MHz, and 4580 periods were added. The arrows show the center of gravity of the arrival of the pulses integrated over the four days of observations, shown in Fig. 2b.

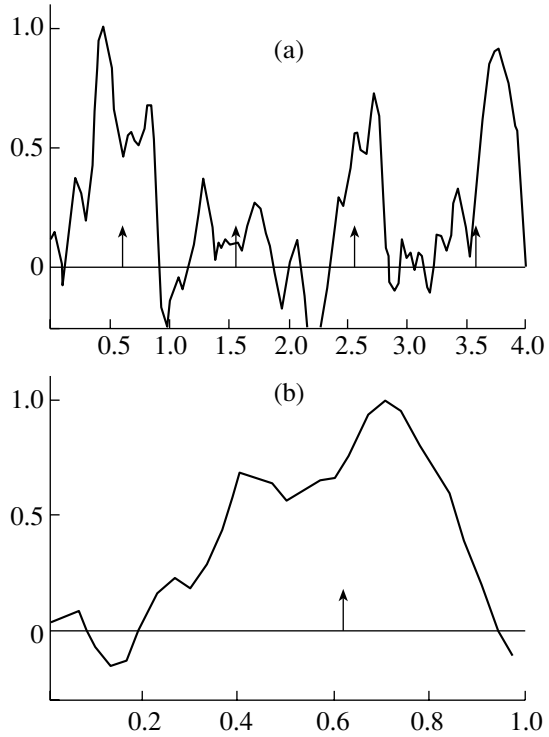

Fig. 2. Sum of four days of observations at 111.23 MHz: (a) group containing a segment equal to the observation interval $P_H = 4P$ (integrated over 4580 P_H), (b) integrated profile of the same group (the sum of 18 320 periods), obtained by convolving the data with the pulsar period. The arrows show the pulse arrival phases.

over three readings. An interpulse is probably present on two of the three days in Fig. 1, whose amplitude becomes 50% of the main pulse in the profile of September 15, 2001 (Fig. 1b). A comparison of the integrated profile duration at 111.23 MHz and in the X-ray [8] shows a striking broadening of the radio pulse (up to 25 ms at halfpower, as compared to ∼2 ms in the X-ray). Given the large dispersion measure (see below), which yields a pulse broadening of 17 ms in a single channel at 111 MHz, the true pulse shape and duration at low frequencies remain unknown. The mean estimate 25 ms was obtained taking into account the effect of the integration constant (3 ms) but neglecting broadening due to dispersion and scattering in the interstellar medium. In spite of the approximate nature of the estimated profile at 111.23 MHz, we observe a composite mean profile that probably consists of two components separated by approximately 19 ms ($\sim 0.29P$) in both the signals for individual days (Figs. 1a–1d) and in the integrated pulse (Fig. 2b).

To confirm the existence of periodic pulsed emission, we carried out observations on the DKR-1000 radio telescope at 88 MHz. Though this antenna has a smaller effective area, the duration of the pulsar observations could be increased by almost a factor of three thanks to its scanning system, leading us to hope that we could detect the pulsar at this frequency as well. Indeed, the pulse amplitude had a signal-to-noise ratio of about 4–5 on four of eight days of observations.

A very important criterion for the presence of the pulsar signal is its dispersion drift across the frequency channels. When summing a signal with the correct dispersion measure (DM), we obtain a

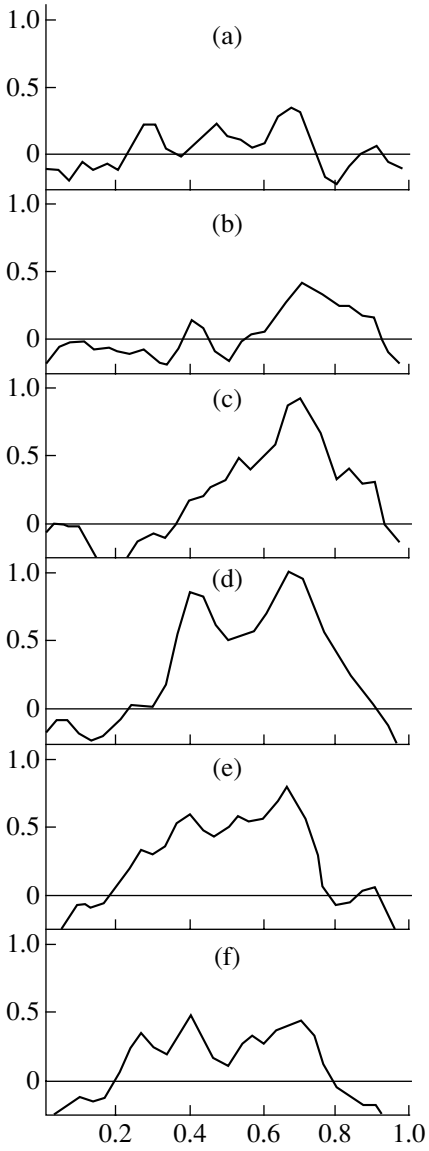

Fig. 3. Sample integrated pulsar profile at 111.23 MHz for August 1, 2002, obtained by summing over 32 frequency channels using various dispersion measures: DM = (a) 111, (b) 121, (c) 131, (d) 141, (e) 151, (f) 161 pc cm^{-3}.

pulse with the maximum amplitude and minimum duration. In the case of J0205, the DM was unknown, but, judging from the most commonly used distance to 3C 58 of 2.6 kpc [12], we expected it might be about 70 pc cm^{-3}. We searched for the DM over a wide range from 5–220 pc cm^{-3}. When observing a pulsar with a small period at meter wavelengths, the pulsar signal drifts quickly in phase due to dispersion, and the shift across several channels can exceed the period if the DM is large. We therefore had to observe over a time that covered six to ten rotational periods of the neutron star. For a long time we were unable to find the optimal DM, although we had four or five DMs for which the pulsar signal displayed the highest signal-to-noise ratios. We adopted the value DM = 24 pc cm^{-3}, which was the smallest of these values of the dispersion measure [19]. After the submission of this paper, Camilo *et al.* [21] reported that they had measured the value DM = 140.7 ± 0.3 pc cm^{-3} based on observations at 800 and 1400 MHz. Reprocessing our data with this new DM, we found that, in most cases, this value yields the best signal-to-noise ratio; therefore, we derived all the pulse profiles (Figs. 1, 2) using the dispersion measure DM = 140.7 pc cm^{-3}. Figure 3 shows an example of a summation over 32 channels at 111.23–110.58 MHz using six different DMs for data obtained on August 1, 2002. The amplitude maximum and duration minimum at DM = 141 ± 10 pc cm^{-3} are readily visible. The same picture is observed on the other best days, including those for the observations at 88 MHz. Using the model for the electron-density distribution in the Galaxy [24], we obtain a distance to the pulsar of 6.4 kpc. This is somewhat unexpected, since the distance to 3C 58 is usually taken to be 2.6 kpc [12].

Over 25 days, observations were obtained at both frequencies with flux-calibration information, enabling us to measure the flux density at 111.23 MHz, $S = 88$ mJy, with the variance roughly equal to this value, and to obtain an upper limit for the flux at 88 MHz, $S < 150$ mJy. Since the pulse was certainly visible at a level of ≈40 mJy on 34 of the 80 days of observations (this follows from an analysis of the calibrated flux measurements for 25 days), while the flux was apparently much lower on other days, we estimate the mean flux for all 80 days of observations to be 88 mJy × 34/80 ≈ 40 mJy, with a variance of ≈40 mJy. Our flux densities at 111 MHz ($S \approx 40$ mJy) and 88 MHz ($S < 150$ mJy), the recent measurements $S \approx 0.13$ mJy and $S \approx 0.045$ mJy at 820 and 1375 MHz [21], and the estimates $S < 3$ mJy at 400 MHz [25], $S < 1.1$ mJy at 606 MHz [26], and $S < 0.15$ mJy at 1400 MHz [27] yield the spectral index $\alpha = 2.8$, which is large and equal to the spectral index of the Crab pulsar.

In spite of the fairly short interval of our observations, we attempted to measure the period and period derivative and compare them with the X-ray data. In the 28-day interval from September 10 to October 7, 2001, we found $P = 0.0656789\,(1)$ s and $\dot{P} = 1.9\,(1) \times 10^{-13}$ for the same epoch as in [8], MJD = 51901.330. Our measurements are in good agreement with the data of [8], while the accuracy of our data is an order of magnitude poorer for the period and two orders of magnitude poorer for the period derivative. This is quite natural, since Murray

et al. [8] used measurements obtained over three years to derive the period and period derivative.

4. DISCUSSION

The detection of radio emission from the pulsar J0205 not only yields information in a new region of the electromagnetic spectrum but also enables us to measure an important new parameter—the dispersion measure—and thus to obtain an independent estimate of the distance to this object. Unfortunately, our new data have not resolved the three main questions concerning the SNR–pulsar system and have even raised new questions. These questions are the age of the system, the distance of the system, and the nature of the emission mechanism, for example, compared to the similar Crab Nebula system.

As is noted above, the SNR 3C 58 is considered an historical remnant, formed 820 years ago [14]. The characteristic age of the pulsar, defined as

$$T_x = \frac{P}{2\dot{P}}, \qquad (1)$$

is 5.4×10^3 yrs. A similar age (5×10^3 yrs) was obtained from the expansion velocity of the radio nebula [28]. Our values of P and $\dot{P}$ also confirm the value $\sim 5 \times 10^3$ yrs. There seems to be a clear discrepancy between the pulsar and SNR data. In fact, this problem can be removed almost entirely if we use the complete formula for the age based on the magnetodipole emission of the pulsar:

$$T_x = \frac{P}{(n-1)\dot{P}}\left[1 - \left(\frac{P_0}{P}\right)^{n-1}\right], \qquad (2)$$

where P_0 is the initial rotational period of the pulsar and n is the braking index. The age 5.4×10^3 yrs is obtained from (1) if we adopt $P_0 \ll P$ and $n = 3$ in (2). However, as correctly noted by Murray *et al.* [8], if we adopt an age for the pulsar of $T = 820$ years and take $n = 3$, we obtain $P_0 = 60.57$ ms from (2). This value depends only weakly on n; in particular, $P_0 = 60.86$ ms for $n = 1.5$. Thus, the most critical parameter for determination of the pulsar age is the unknown value of P_0; this means that the age estimate of 5.3×10^3 yrs for the pulsar could be incorrect, and its true age could be 820 years.

The second uncertainty is connected with the "everlasting" astronomical problem of distance determinations. As we indicated above, observations of two HI absorption features yielded distances to 3C 58 of from 2 to >6 kpc; the value of 2.6 kpc [12] is used most frequently in the literature. The dispersion measure found by Camilo *et al.* [21] yields a distance to PSR J0205 of 6.4 kpc, more than twice than the former preferred value. The distance of 6.4 kpc was

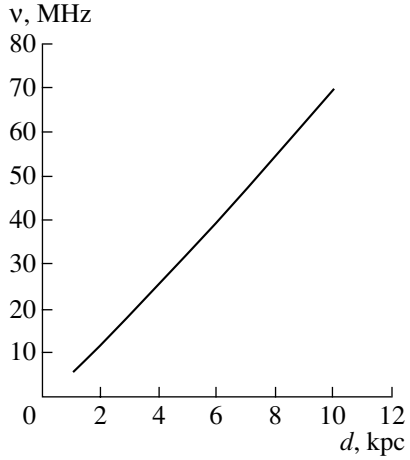

Fig. 4. Frequency of the low-frequency cutoff in the spectrum *versus* distance to the pulsar for a given radio luminosity.

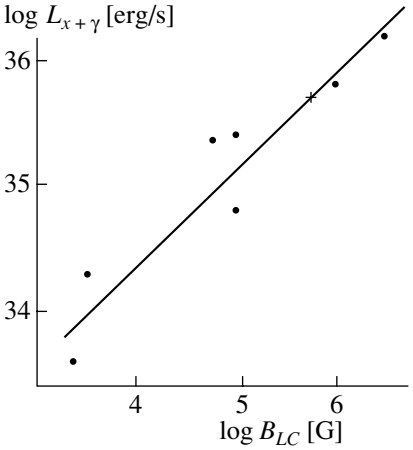

Fig. 5. Observed hard luminosity *versus* magnetic-field strength at the light cylinder. The cross shows the expected position of PSR J0205.

obtained using the model for the interstellar medium proposed by Taylor and Cordes [24], which takes into account large-scale variations of the Galactic electron density. If the electron density in the direction toward 3C 58 is higher than the mean model density, a different distance estimate can be obtained. Moreover, as noted in the Introduction, some radio measurements suggest a distance to 3C 58 >6 kpc (see, for example, the references in [10]). Thus, the value in 6.4 kpc we have obtained is near the high end of the overall range of distance estimates.

The third problem, also noted in [8], is the large difference in the X-ray luminosities of the 3C 58 and Crab Nebula systems, whose other parameters are similar, for both the supernova remnants and the pulsars in them. The radio flux of PSR B0531+21 is also much greater than that of PSR J0205,

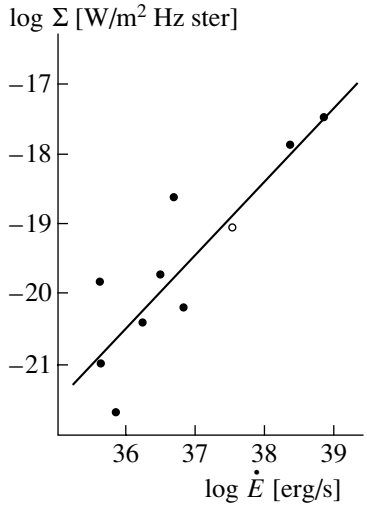

Fig. 6. Surface brightness of a plerion at 1 GHz (W/m^2/Hz/ster) *versus* the rate of loss of the pulsar's rotational energy. The open circle shows the position of the PSR J0205−3C58 system.

though their periods (33 and 66 ms), period derivatives (4.2×10^{-13} and 1.93×10^{-13} s/s), and magnetic fields calculated using a magnetodipole model (7.6×10^{12} and 7.2×10^{12} G) are similar. We obtain for the flux ratio at 111 MHz $21\,000/40 \approx 530$, if we use the mean flux of the Crab pulsar measured from the compiled spectrum [16]. The next section considers a possible explanation of this large difference in the fluxes of these two similar objects in various regions of the electromagnetic spectrum.

5. INTERPRETATION

The pulsar J0205 has a period of $P = 66$ ms. Due to the small size of their magnetospheres, the emission of such pulsars is generated near the light cylinder ($r \sim r_{LC} = \frac{cP}{2\pi}$) [30]. In this case, the correlation of the radio luminosity L_r [31] and optical luminosity L_{opt} [32] with the magnetic-field strength at the light cylinder B_{LC} provides nearly unambiguous evidence that the dominant mechanism for the generation of the observed emission is synchrotron radiation. The main features of the emission of PSR J0205 can be explained in this framework.

First and foremost, the magnetic field strength at the surface of the neutron star derived from the power of the magnetodipole emission for this pulsar, $B_s = 7.2 \times 10^{12}$ G, is approximately equal to the corresponding quantity for PSR B0531, $B_s = 7.6 \times 10^{12}$ G (we have taken into account the correction of the catalog value by a factor of two; see, for example, [33]). However, the period of PSR J0205 is approximately twice as long (to simplify the calculations, we will take the period ratio to be exactly two); therefore, if its magnetic field has a dipole structure, the field strength at the light cylinder is a factor of eight weaker. In addition, the density of relativistic particles, which is determined by the density of Goldreich and Julian [34]

$$n = \frac{B}{Pce} = \frac{8\pi^3 R_*^3 B_s}{c^4 e P^4}, \qquad (3)$$

where R_* is the neutron-star radius, will be a factor of 16 lower in this region. The radio luminosities of short-period pulsars are approximately proportional to B [31]. Since the radio emission should be coherent, so that $L \propto Bn^2$, we expect the flux of PSR J0205 to be a factor of 2000 weaker than the flux of PSR B0531+21 (for identical conditions for the generation of the coherent emission and equal Lorentz factors and pitch angles ψ for the radiating particles). In the previous section, we showed that the flux of the Crab pulsar exceeds the flux of PSR J0205 at 111 MHz by a factor of 530; in view of the assumptions made, this is in good agreement with the above estimate.

When calculating the X-ray flux, we should keep in mind that the X-ray emission is not coherent; therefore, its intensity I_ν should be proportional to the first power of the density n. However, the dependence of I_ν on the magnetic field is also determined by the electron distribution function, and for the power-law distribution $I_\nu \propto B^{\frac{\alpha+1}{2}}$ [36]. For the spectral index $\alpha \sim 2.8$ (see above) the ratio of the X-ray luminosities L_x of the Crab pulsar and of PSR J0205 should be ~ 1000, also in agreement with the observational data: the X-ray luminosity of the pointlike source in 3C 58 identified with PSR J0205 is $L_x = 2 \times 10^{32}$ erg/s [8], whereas the value for PSR B0531+21 is $L_x \approx 4 \times 10^{35}$ erg/s [37].

The $L_r(B_{LC})$ and $L_{opt}(B_{LC})$ correlations noted above can be represented as

$$\log L_r = (1.08 \pm 0.17) \log B_{LC} + (24.25 \pm 0.72), \qquad (4)$$
$$\rho = 0.89 \pm 0.14, \quad N = 13$$

and

$$\log L_{opt} = (1.85 \pm 0.47) \log B_{LC} + (21.00 \pm 2.32), \qquad (5)$$
$$\rho = 0.91 \pm 0.23, \quad N = 5,$$

where ρ is the corresponding correlation coefficient and N is the number of objects in the sample.

It follows from these relationships that the optical bolometric luminosity of PSR J0205 is $L_{opt} \approx 10^{31}$ erg/s, so that it should be possible to detect pulsed optical emission from this object; and its integrated radio luminosity L_r should be

$\approx 10^{30}$ erg/s. Using this value of L_r together with our 111-MHz data, we can estimate the expected radio spectral index of the pulsar radiation. The formula for calculating the luminosity can be written

$$L_r = \frac{\pi^3 d^2}{P} \int_{\nu_*}^{\infty} S_\nu w_\nu d\nu, \qquad (6)$$

where d is the distance to the pulsar, w_ν is the pulse width at ν, and ν_* is the frequency of the low-frequency cutoff in the spectrum.

We can use the values of L_r, d, and ν_* and the measured values of S_{111} and w_ν to determine the expected spectral index:

$$2\log\left(\frac{1.11\times 10^8}{\nu_*}\right) = \log(\alpha-1) + \log\frac{PL_r}{S_{111} w_\nu \pi^3 d^2 \nu_*}. \qquad (7)$$

For further estimates, we assumed that the ratio $\frac{w_\nu}{P} = 0.6$ does not depend on frequency, $S_\nu = S_{111}\left(\frac{111}{\nu_{\rm MHz}}\right)^\alpha$, $\nu_* = 10$ MHz, $d = 2.6$ kpc [12]. In this case, we obtain

$$\alpha = 0.96\log(\alpha-1) + 3.16. \qquad (8)$$

The solution of (8) yields $\alpha = 3.55$, indicating that the spectrum should be very steep. This estimate was made before the publication of [21], reporting the observed value of $\alpha = 2.8$. Using $\alpha = 2.8$ for the calculated value, the given L_r and d values, and the measured values of S_{111} and w_{111}, we can determine the expected cutoff frequency in the spectrum:

$$\nu_* = \left\{\frac{\pi^3 d^2 w S_{111}(1.11\times 10^8)^{2.7}}{1.7 P L_r}\right\}^{1/1.7}. \qquad (9)$$

Substituting numerical values for the parameters, we obtain $\nu_* = 13.4$ MHz. It follows from (9) that the values of ν_* and d are related (Fig. 4). If the cutoff frequency can be measured, an independent estimate of the distance to the pulsar can be obtained.

The total synchrotron luminosity at all frequencies can be calculated using the formulas derived in [31, 38], which result in the expression

$$L_s = \frac{\pi^{7/2} 3^{1/2} e I \gamma_b^{3/2} \dot{P}}{32 m^{1/2} c^{3/2} P^{7/2} \gamma_p^2}, \qquad (10)$$

where γ_b is the Lorentz factor of the primary beam and γ_p is the Lorentz factor of the secondary electron–positron plasma. For $\gamma_b = 10^6$, $\gamma_p = 3$, $I = 10^{45}\,\mathrm{g\,cm^2}$, and the P and $\dot{P}$ of PSR J0205, we obtain $L_s = 2.75\times 10^{33}$ erg/s, which coincides with the observed luminosity of the central source in 3C 58 at 0.08–10 keV [8].

Table

P	0.0656789(1) s
$\dot{P}$	$1.9(1)\times 10^{-13}$
MJD	51901.330
DM	141 ± 10 pc cm^{-3}
S_{111}	40 mJy
S_{88}	<150 mJy
w_{50}(111 MHz)	~25 ms
w_{10}(111 MHz)	~40 ms

We can derive the same relationship $L(B_{LC})$ as in the radio and optical for the hard radiation (X-rays and γ rays). This is shown in Fig. 5 and can be written

$$\log L_{X+\gamma} = (0.83\pm 0.14)\log B_{LC} + (31.20\pm 0.70), \qquad (11)$$

$$\rho = 0.93 \pm 0.36, \qquad N = 7.$$

The luminosities $L_{X+\gamma}$ are taken from [37]. It follows from this relationship that $L_{X+\gamma}$ is also strongly correlated with B_{LC}, again testifying to the generation of the radiation at the pulsar's periphery. Moreover, the $L_{X+\gamma}(B_{LC})$ dependence enables us to predict the luminosity of PSR J0205 from the known B_{LC}; this is $L_{X+\gamma} = 7\times 10^{35}$ erg/s, making searches for gamma rays from this pulsar promising. Note that this estimate of $L_{X+\gamma}$ is higher than the total synchrotron luminosity L_s indicated above. This probably implies the need to invoke inverse Compton scattering to describe the gamma-ray emission of radio pulsars, in addition to the synchrotron mechanism.

There is currently no fully adequate theory describing the interaction of a plerion SNR with a young pulsar and its evolution. The difficulties of modern plerion models and, in particular, problems connected with 3C 58 have been considered in [39, 40]. A description of the characteristics of 3C 58 as an individual object is the subject of a dedicated paper. However, in light of what we have said about the magnetic-field strength and the density of relativistic particles at the periphery of the magnetosphere, we expect weaker emission from 3C 58 compared to the Crab Nebula at all frequencies. Furthermore, the possibly similar period and period derivative at the birth epoch of PSR J0205 [8] make the rate of loss of its rotational energy $|\dot{E}_0| = 4\pi^2 I \dot{P}_0/P_0^3$ close to its present value, 2.7×10^{37} erg/s, considerably lower than $\dot{E}_{\rm Crab} = 4.6\times 10^{38}$ erg/s. On a $\log\Sigma(\log\dot{E})$

plot (Fig. 6), 3C 58 + PSR J0205 lie very close to the statistical dependence

$$\log \Sigma = (1.11 \pm 0.24) \log |\dot{E}| - (60.37 \pm 8.95), \quad (12)$$
$$\rho = 0.87 \pm 0.19, \qquad N = 9,$$

derived for nine known plerions [41]. Therefore, this system appears to be typical of the class of plerions.

6. CONCLUSIONS

(1) Using observations carried out on the Pushchino Radio Astronomy Observatory LPA (111 MHz) and DKR-1000 (88 MHz) telescopes, we have detected pulsed radio emission from the X-ray pulsar J0205+6449 in the supernova remnant 3C 58. Its parameters are listed in the table.

(2) We estimate the distance to the pulsar to be 6.4 kpc, consistent with the maximum estimates of the distance to the SNR based on other methods ($\geq$6 kpc).

(3) The model of synchrotron emission near the light cylinder can explain the difference between the luminosities of PSR J0205 and PSR B0531+21 in the radio and X-ray.

(4) We have predicted the optical and gamma-ray luminosities of this object, which are sufficiently high to offer hope for successful searches for pulsed emission in these ranges.

(5) For a distance to PSR J0205 of 2.6 kpc, we predict the low-frequency cutoff in the spectrum should be at $\nu_* = 13$ MHz. The dependence of ν_* on the distance d to the pulsar can be used to obtain an independent estimate of d, and *vice versa*: if the distance is known, we can estimate the cutoff frequency. In particular, if the distance exceeds 6 kpc, the spectrum should peak at $\sim$50 MHz, which can in principle be detected with existing or planned large radio telescopes.

ACKNOWLEDGMENTS

The authors are grateful to S.M. Kutuzov, A.S. Aleksandrov, V.V. Ivanova, and K.A. Lapaev for help with the observations, to M.V. Popov and R.D. Dagkesamanskiĭ for useful discussions, and to L.B. Potapova for help in preparing the manuscript. This work was supported by the National Science Foundation (project 00-98685) and INTAS (grant 00-849) as well as the Russian Foundation for Basic Research (project no. 00-02-17850).

REFERENCES

1. D. H. Staelin and E. C. Reifenstein, Science **162**, 1481 (1968).
2. V. M. Kaspi, in *IAU Colloq. 160: Pulsars: Problems and Progress,* ASP Conf. Ser. **105**, Ed. by S. Johnston, M. A. Walker, and M. Bailes (Astronomical Society of the Pacific, San Francisco, 1996), p. 375.
3. V. M. Kaspi, in *IAU Colloq. 177: Pulsar Astronomy - 2000 and Beyond,* ASP Conf. Ser. **202**, Ed. by M. Kramer, N. Wex, and N. Wielebinski (Astronomical Society of the Pacific, San Francisco, 2000), p. 485.
4. B. M. Gaensler, O. P. Slane, E. V. Gotthelf, and C. A. Vashish, Astrophys. J. **559**, 963 (2001).
5. C. Thompson and R. C. Duncan, Astrophys. J. Lett. **392**, L9 (1992).
6. E. V. Gotthelf, C. A. Vasish, M. Boylan-Kolchin, and K. Torri, Astrophys. J. Lett. **542**, L37 (2000).
7. V. B. Kaspi and D. J. Helfand, *Neutron Stars in Supernova Remnants,* ASP Conf. Ser. **271**, Ed. by P. O. Slane and B. M. Gaensler (Astronomical Society of the Pacific, San Francisco, 2002), p. 3.
8. S. Murray, P. Slane, F. Seward, *et al.*, Astrophys. J. **568**, 226 (2002).
9. R. H. Becker, D. J. Helfand, and A. E. Szymkowiak, Astrophys. J. **255**, 557 (1982).
10. T. A. Lozinskaya, *Supernovae and Stellar Wind. Interaction with Galactic Gas* [in Russian] (Nauka, Moscow, 1986).
11. D. R. W. Williams, Astron. Astrophys. **28**, 309 (1973).
12. D. A. Green and S. F. Gull, Nature **299**, 606 (1982).
13. J. H. Taylor, R. N. Manchester, A. J. Lyne, and F. Camilo, unpublished work (1995).
14. D. H. Clark and F. R. Stephenson, *The Historical Supernova* (Pergamon, Oxford, 1977).
15. P. O. Slane, D. J. Helfand, and S. S. Murray, Astrophys. J. Lett. **571**, L45 (2002).
16. V. M. Malofeev, *Catalog of Pulsar Radio Spectra* [in Russian] (Nauchn. Izd. Pushchino, 1999).
17. S. A. Tyul'bashev and O. I. Malov, Astron. Zh. **77**, 737 (2000) [Astron. Rep. **44**, 654 (2000)].
18. V. M. Malofeev, O. I. Malov, and N. V. Shchegoleva, Astron. Zh. **77**, 499 (2000) [Astron. Rep. **44**, 436 (2000)].
19. V. M. Malofeev, O. I. Malov, and A. P. Glushak, IAU Circ. No. 7775 (2001).
20. S. M. Ranson, *Proceedings of the 199th AAS Meeting, Washington, 2002,* p. 709.
21. F. Camilo, I. Stairs, D. Lorimer, *et al.*, Astrophys. J. Lett. **571**, L41 (2002).
22. V. M. Malofeev and O. I. Malov, Astron. Zh. **77**, 52 (2000) [Astron. Rep. **44**, 45 (2000)].
23. Yu. A. Fedorov, Yu. P. Il'yasov, A. S. Vdovin, and V. V. Oreshko, Izmer. Tekh. **4**, 27 (1989).
24. J. H. Taylor and J. Cordes, Astrophys. J. **411**, 674 (1993).
25. R. Dewey, Astrophys. J. Lett. **294**, L25 (1985).
26. D. R. Lorimer, A. G. Lyne, and F. Camilo, Astron. Astrophys. **321**, 1002 (1998).
27. D. A. Frail and D. A. Moffett, Astrophys. J. **408**, 637 (1993).

28. M. F. Bietenholf, N. E. Kassim, and K. W. Weiler, Astrophys. J. **560**, 772 (2001).
29. R. N. Manchester, G. R. Huguenin, and J. H. Taylor, Astrophys. J. Lett. **174**, L19 (1972).
30. I. F. Malov, Astron. Zh. **74**, 697 (1997) [Astron. Rep. **41**, 617 (1997)].
31. I. F. Malov, Astron. Zh. **76**, 825 (1999) [Astron. Rep. **43**, 727 (1999)].
32. A. Shearer, A. Golden, and J. Beskin, *IAU Colloq. 177: Pulsar Astronomy—2000 and Beyond,* ASP Conf. Ser. **202**, Ed. by M. Kramer, N. Wex, and N. Wielebinski (Astronomical Society of the Pacific, San Francisco, 2000), p. 307.
33. S. L. Shapiro and S. A. Teukolsky, *Black Holes, White Dwarfs, and Neutron Stars* (Wiley-Intersci., New York, 1983; Mir, Moscow, 1985), Vol. 2.
34. P. Goldreich and W. H. Julian, Astrophys. J. **157**, 869 (1969).
35. I. F. Malov and O. I. Malov, Astron. Zh. **72**, 567 (1995) [Astron. Rep. **39**, 503 (1995)].
36. A. G. Pacholczyk, *Radio Astrophysics* (Freeman, San Francisco, 1970; Mir, Moscow, 1973).
37. D. J. Thompson, *IAU Colloq. 160: Pulsars: Problems and Progress,* ASP Conf. Ser. **105**, Ed. by S. Johnston, M. A. Walker, and M. Bailes (Astronomical Society of the Pacific, San Francisco, 1996), p. 307.
38. I. F. Malov and G. Z. Machabeli, Astron. Zh. **79** (2003) (in press) [Astron. Rep. **46** (2003) (in press)].
39. D. A. Green and P. A. G. Scheuer, Mon. Not. R. Astron. Soc. **258**, 833 (1992).
40. L. Woltjer, M. Salvati, F. Pacini, and R. Bandiera, Astron. Astrophys. **325**, 295 (1997).
41. R. Kothes, Mem. SAI **69**, 971 (1998).

Translated by G. Rudnitskiĭ

Astronomy Reports, Vol. 47, No. 5, 2003, pp. 422–429. Translated from Astronomicheskiĭ Zhurnal, Vol. 80, No. 5, 2003, pp. 458–466.

Sodium Abundances in Stellar Atmospheres with Differing Metallicities

T. V. Mishenina[1], V. V. Kovtyukh[1], S. A. Korotin[1], and C. Soubiran[2]

[1] *Astronomical Observatory, Odessa State University, Odessa, Ukraine*

[2] *Observatoire de Bordeaux, Floirac, France*

Received March 24, 2002; in final form, November 27, 2002

Abstract—The non-LTE sodium abundances of 100 stars with metallicities $-3 < [Fe/H] < 0.3$ are determined using high-dispersion spectra with high signal-to-noise ratios. The sodium abundances [Na/Fe] obtained are close to the solar abundance and display a smaller scatter than values published previously. Giants ($\log g < 3.8$) with $[Fe/H] < -1$ do not display overabundances of sodium, and their sodium abundances do not show an anticorrelation with the oxygen abundance, in contrast to globular-cluster giants. They likewise do not show sodium-abundance variations with motion along the giant branch. No appreciable decrease in the sodium abundance was detected for dwarfs ($\log g > 3.8$) with metallicities $-2 < [Fe/H] < -1$. The observed relation between [Na/Fe] and [Fe/H] is in satisfactory agreement with the theoretical computations of Samland, which take into account the metallicity dependence of the sodium yield and a number of other factors affecting the distribution of elements in the Galaxy during the course of its evolution. © *2003 MAIK "Nauka/Interperiodica"*.

1. INTRODUCTION

The sodium abundances in the atmospheres of stars with various metallicities can be used to test theories of the chemical evolution of the Galaxy, nucleosynthesis, and stellar evolution. According to our current understanding of nucleosynthesis theory, sodium is primarily a product of the hydrostatic burning of carbon and neon in massive stars [1], in contrast to iron, which is the product of explosive nucleosynthesis in massive supernovae (SN II) and in white dwarfs in binary systems (SN Ia). Additional sodium can be synthesized during hydrogen burning via the NeNa cycle in moderate-mass stars [2], after which it can be carried to atmospheric layers due to the inward expansion of the convective envelope and its penetration into the layers in which the NeNa cycle occurs. During the subsequent evolution of the star, material enriched in sodium can be ejected with the stellar wind, enhancing the interstellar medium in sodium.

The production or yield of an element can be calculated quantitatively and estimated by comparing the observed abundance of the element and the predictions of chemical-evolution models. Here, we come up against a many-parameter problem, since the yield of an element depends on many preconditions and components of the theories of nucleosynthesis and chemical evolution. For example, the yield of elements that form during phases of hydrostatic burning depends most strongly on the model for the presupernova star (the criteria for convection, mixing processes, mass loss, and the cross sections for nuclear reactions). The sodium yield is also sensitive to the neutron excess [1] and consequently depends on the metallicity [3]. However, the total yield of an element examined in the framework of theories of the chemical evolution of the Galaxy also depends on the initial mass function, the inflow of gas, mixing processes in the interstellar medium, the production of energy by supernovae, etc.

Observational data play a key role in such comparisons. The observational situation with regard to sodium in stars is currently not entirely clear and unambiguous, especially in the case of metal-poor stars. For example, supergiants and giants with solar metallicity show appreciable overabundances of sodium [4], which are not fully removed when the sodium lines are subject to a non-LTE analysis [5, 6]. The mechanism for forming sodium in the NeNa cycle was proposed precisely to explain such overabundances [2]. In their study of halo giants and subgiants, Pilachowski *et al.* [7] did not detect sodium excesses and instead found a small sodium deficit $[Na/Fe] = -0.17 \pm 0.22$, with some increase in [Na/Fe] with progression through this evolutionary stage, and an overall scatter of [Na/Fe] values from -0.6 to $+0.3$. Sodium abundances were also determined by Carretta *et al.* [8], who found the mean value $[Na/Fe] = -0.09 \pm 0.19$ for stars with $[Fe/H] < -0.6$. In their estimates of [Na/Fe] for metal-poor stars on the giant branch, Gratton *et al.* [9] found $[Na/Fe] >= -0.09 \pm 0.15$ for

1063-7729/03/4705-0422$24.00

stars on the lower part of the branch and [Na/Fe] >= -0.02 ± 0.15 for stars on the upper part. The results are in agreement within the errors and also do not differ significantly from the mean value for halo giants. In contrast to halo stars, metal-poor giants in globular clusters ([Fe/H] ≈ -1.5) display appreciable Na overabundances and an anticorrelation between the abundances of Na and O (or the abundances of Al and O) [10–12]. The Na abundances in these stars can be explained in part by the synthesis of sodium in the NeNa cycle in main-sequence stars [13, 14] and the subsequent carrying of material enriched in Na (and depleted in O) to the stellar surface during the giant stage. The observed scatter of the Na abundances could also be due to inhomogeneity of the initial chemical composition of the stellar material, since a scatter of the CH- and CN-band intensities and an Na–O anticorrelation have also been detected among dwarfs in globular clusters [15]. Note that giants in metal-rich globular clusters such as M71 ([Fe/H] $= -0.8$) have [Na/Fe] ratios that are close to solar.

The picture observed for disk and halo dwarfs is the following. Disk dwarfs display solar sodium abundances with a moderate tendency for this abundance to increase with metallicity [16, 17]. The situation is different for stars that are deficient in metals: the [Na/Fe] values are scattered over two orders of magnitude, with a general tendency for values [Na/Fe] ~ 0 to be obtained by some authors [18, 19] and a decrease in the sodium abundance with decreasing metallicity to be obtained by others [20]. In particular, studies of the Na abundances of halo stars in extreme orbits [20] indicate an appreciable decrease in [Na/Fe] (to -0.7 dex) as [Fe/H] decreases from -1 to -2. Note that the abundances of other elements display behavior that is typical for halo stars. Studies of thick-disk stars ([Fe/H] > -1.2) yield the mean value [Na/Fe] $= 0.101 \pm 0.017$ and a moderate growth in the sodium abundance with decreasing metallicity [21]. Thus, the metallicity range $-2 <$ [Fe/H] < -1 is crucial when determining sodium abundances. High-resolution spectroscopy presents new opportunities for studying previously obtained results in more detail, based on high-dispersion spectral material of high quality for large samples of stars with a wide range of metallicities and to compare the new results with modern theories of chemical evolution with the aim to elucidate the main suppliers of sodium to the interstellar medium.

2. THE OBSERVATIONAL MATERIAL

We addressed the problem at hand by selecting 100 dwarf, giant, and subgiant stars with metallicities $-3 <$ [Fe/H] < 0.3, listed in Table 1. Spectra of these stars were obtained on the 1.93-m telescope of the Haute Provence Observatory equipped with the ELODIE echelle spectrometer [22]. The resolution of the spectrometer was 42 000, the wavelength range observed was $\lambda\lambda 4400$–6800 Å, and the resulting signal-to-noise ratios were 130–230. The preliminary reduction of the spectra (extraction of the images, removal of cosmic rays, flat-fielding, etc.) had been performed earlier [23]. We carried out the further reduction of the spectra (fitting the continuum level, measuring the line equivalent widths EW, etc.) using the DECH20 package [24]. The equivalent widths were measured by fitting the line profiles with Gaussians. A comparison of the line EW values for our spectra with those obtained in other studies is presented in [25]. There is good agreement between the EW's obtained in the different systems.

3. ATMOSPHERIC PARAMETERS

The main characteristics of the studied stars are presented in Table 1. We took values for the V magnitude and $B - V$ color index from the SIMBAD database. We calculated the bolometric magnitudes $M_{\rm bol}$ using the bolometric corrections of Alonso *et al.* [26] and took the parallaxes π from HIPPARCOS observations.

The use of direct methods to determine the effective temperature $T_{\rm eff}$ is possible only for a limited number of stars, since this requires knowledge of their radii and distances. The application of photometric and spectral methods is subject to a number of additional errors. Photometric methods rely on theoretical or empirical spectral calibrations and require corrections for interstellar reddening, while spectral methods require reliable extinction coefficients and corrections for possible departures from local thermodynamic equilibrium (non-LTE corrections). We accordingly used the following iterative procedure to determine $T_{\rm eff}$. As a first approximation for $T_{\rm eff}$, we used the data of Soubiran *et al.* [22], which are based on a statistical method that makes use of a large number of spectral lines, and values for $T_{\rm eff}$ taken from various sources with corresponding weights. We then refined $T_{\rm eff}$ based on the condition that the iron abundance derived from a given line be independent of the excitation energy of the lower level of that line E_{low}. As a check on the resulting $T_{\rm eff}$, we calculated theoretical H_α profiles using the STARSP program [27] and compared these with the observed profiles. A good agreement was obtained for all the studied stars.

The gravity $\log g$ was determined from the condition of ionization equilibrium for the iron lines and

Table 1. Main atmospheric parameters, NaI equivalent widths, and relative abundances of oxygen [O/Fe] and sodium [Na/Fe]

Star	Atmospheric parameters						Chemical composition			EW, mÅ (NaI lines)		
	V	$B-V$	M_{bol}	T_{eff}, K	$\log g$	V_t, km/s	[Fe/H]	[O/Fe]	[Na/Fe]	5682	6154	6160
HD 245	8.41	0.65	4.29	5400	3.4	0.50	−0.78		0.14	62.0	16.2	27.0
HD 2796	8.48	0.75	−0.27	4900	1.6	1.50	−2.21		−0.06	5.0		
HD 3546	4.34	0.87	0.51	4950	2.1	1.50	−0.63	0.18	0.02		32.2	47.0
HD 3567	9.25	0.46	4.04	5950	3.8	0.50	−1.20		0.02			6.3
HD 5395	4.62	0.96	0.30	4800	2.5	1.00	−0.19	0.05	−0.11	121.0	50.3	71.0
HD 5916	6.86	0.90	0.63	4863	1.7	1.20	−0.51	−0.04	−0.12		32.5	50.0
HD 6582	5.17	0.69	5.60	5240	4.2	0.20	−0.89		0.10	67.0	15.0	27.0
HD 6755	7.72	0.72	1.94	5100	2.7	1.20	−1.47		−0.18	13.0		6.0
HD 6833	6.75	1.18	−0.52	4400	1.0	1.50	−0.89		−0.19		28.3	38.0
HD 8724	8.30	0.96	0.34	4600	1.5	1.50	−1.65	0.41	−0.05	21.0	4.6	7.0
HD 10700	3.49	0.72	5.51	5270	4.2	0.50	−0.56		0.05	84.0	27.0	47.0
HD 13530	5.31	0.92	1.05	4750	2.5	1.00	−0.48	0.07	0.38	130.0	70.0	93.0
HD 13783	8.30	0.68	5.21	5350	4.1	0.50	−0.61		0.06	76.0	20.8	40.1
HD 15596	6.21	0.90	0.96	4750	2.5	1.00	−0.67	0.23	0.04		35.0	56.0
HD 18768	6.72	0.59	3.30	5700	3.5	1.00	−0.51		0.08		19.6	30.5
HD 19445	8.04	0.46	4.96	6000	4.0	1.50	−1.89		0.19	5.6		
HD 22879*	6.74	0.54	4.75	5900	4.0	0.50	−0.77		0.04	42.0	8.0	15.0
HD 23439	7.67	0.78	5.51	5100	4.3	1.00	−1.14		0.20		15.0	23.0
HD 25329	8.51	0.88	6.87	4850	4.3	1.50	−1.73		0.24	30.6		11.1
HD 26297	7.46		−0.26	4300	0.5	1.70	−1.91	0.28	−0.15	20.0	3.3	6.0
HD 29150*	7.60		4.88	5734	4.4	0.90	−0.07		0.10	119.0	42.2	64.0
HD 30562*	5.77	0.63	3.58	5864	4.1	1.30	0.13		0.05	119.0	47.0	70.0
HD 37828	6.86	1.14	−0.66	4350	1.0	1.50	−1.58	0.28	0.09	44.0	17.0	19.0
HD 43318*	5.63	0.49	2.86	6287	4.1	1.50	−0.13		0.05	78.0	20.4	38.0
HD 43856*	7.95	0.51	3.43	6247	4.0	0.90	−0.10		0.00	75.0	19.3	34.8
HD 44007	8.05	0.84	1.36	4950	2.3	1.50	−1.49	0.38	0.07	26.0	6.0	10.0
HD 45282	8.00	0.66	2.15	5350	3.4	1.30	−1.28	0.62	−0.16			6.0
HD 45654	6.86		2.45	6375	4.0	1.20	−0.17		−0.05	59.0	15.0	28.0
HD 46480	5.94	0.89	1.98	4800	2.7	0.80	−0.49	0.22	0.07		47.0	68.0
HD 49932*	6.97		1.70	6375	4.0	1.50	−0.16		−0.03		16.0	30.0
HD 51419*	6.94		4.93	5714	4.0	0.75	−0.35		−0.08	70.0	18.0	30.0
HD 51530	6.20	0.45	2.76	6100	3.8	0.80	−0.39	0.20	0.08	62.0	16.0	29.0
HD 57006*	5.90	0.53	2.02	6248	3.6	1.45	0.01		0.02	86.0	27.0	42.0
HD 58595*	7.40		5.03	5750	4.1	0.80	−0.22		−0.03	83.7	24.0	
HD 62613*	6.56		5.26	5450	4.0	1.30	−0.17		0.05	110.0	42.9	66.0
HD 63791	7.89		0.37	4625	1.8	1.20	−1.67		0.00	27.0	7.3	6.0
HD 64090	8.27	0.61	5.83	5400	4.3	1.50	−1.69		0.08			3.7
HD 64606	7.43	0.83	5.82	5250	4.0	0.50	−0.82		0.10	67.0	17.0	31.0
HD 64815*	7.80		3.24	5850	4.0	0.80	−0.30		0.05	77.0	22.0	37.0
HD 73344*	6.89		4.14	6130	4.1	0.80	0.17		0.03	102.0	40.0	58.0
HD 76932	5.80	0.53	4.06	5840	4.0	1.00	−0.90	0.36	0.11	39.0	6.8	15.0
HD 84937	8.33	0.40	3.68	6250	3.8	1.50	−2.00		0.33	5.1		
HD 87140	8.97	0.70	1.95	5100	2.5	1.50	−1.71		0.05			5.0
HD 88609	8.59	0.93	0.91	4600	1.0	1.50	−2.66		0.15	4.0		
HD 88725	7.75	0.60	4.85	5650	4.3	1.00	−0.65		0.09	74.0	15.0	24.0
HD 94028	8.21	0.47	4.51	5950	4.0	1.50	−1.43		0.02			3.6
HD 95128*	5.10	0.61	4.29	5885	4.1	0.80	0.07		0.00		40.2	60.0
HD 103095*	6.42	0.75	6.37	5000	4.4	0.30	−1.39	0.57	−0.10	25.0		8.0
HD 105755	8.59		4.01	5800	3.9	1.50	−0.65	0.26	0.00	51.0	15.0	15.0
HD 108076	8.03	0.56	5.07	5700	4.4	0.70	−0.85	0.57	0.21	51.0	14.0	21.1

Table 1. (Contd.)

Star	Atmospheric parameters						Chemical composition			EW, mÅ (NaI lines)		
	V	$B-V$	M_{bol}	T_{eff}, K	$\log g$	V_t, km/s	[Fe/H]	[O/Fe]	[Na/Fe]	5682	6154	6160
HD 108954*	6.15	0.55	4.46	6040	4.4	1.30	−0.14		0.02	87.0	26.0	40.0
HD 110184	8.27	1.17	−0.48	4380	0.6	1.90	−2.27	0.30	0.16	13.0		
HD 114762	7.30	0.53	4.16	5800	4.0	1.00	−0.72	0.39	0.14		14.0	20.0
HD 117876	6.11	0.96	−0.01	4750	2.3	1.40	−0.47	0.17	0.22		63.0	88.0
HD 122563	6.18	0.90	−1.30	4570	1.1	1.20	−2.42	0.49	0.06	6.6		
HD 122956	7.22	1.01	−0.54	4635	1.5	1.50	−1.60		−0.19	21.0		6.0
HD 124897	−0.05	1.23	−0.83	4350	1.6	1.60	−0.58	0.31	0.14		75.0	102.0
HD 127243	5.58	0.83	0.45	5000	2.3	1.40	−0.65	0.15	0.06	91.0	31.0	43.0
HD 132142	7.77	0.79	5.67	5100	4.0	1.00	−0.51	0.18	0.08	110.0	43.0	57.5
HD 134169	7.67	0.55	3.69	5800	3.9	1.10	−0.72		0.10	45.0	14.9	19.0
HD 150177	6.33	0.48	3.07	6025	3.8	1.10	−0.64		0.10	48.0	12.0	19.0
HD 150680*	2.81	0.64	2.56	5850	3.8	1.50	0.01		0.11	115.0	44.7	63.8
HD 157089	6.95	0.60	3.92	5785	3.8	1.00	−0.56	0.21	−0.01		14.0	23.0
HD 159222*	6.56	0.64	4.60	5763	4.3	1.30	0.00		0.04	114.0	45.0	64.0
HD 159482	8.37	0.57	4.84	5620	4.0	0.80	−0.86		0.16		12.0	20.3
HD 160693	8.39	0.58	4.61	5750	4.0	1.00	−0.46		0.08	70.0	23.0	31.0
HD 161797*	3.42	0.75	3.68	5650	4.0	1.30	0.25		0.11	145.0	71.0	93.0
HD 165195	7.31	1.29	−0.47	4470	1.1	1.90	−2.03	0.50	0.03	17.5		5.0
HD 165908	5.05	0.52	4.00	5925	4.1	1.10	−0.61	0.25	0.13	55.0	15.0	25.0
HD 166161	8.12	0.97	1.89	5250	2.0	1.70	−1.20	0.40	0.00	31.4	5.4	12.9
HD 175305	7.18	0.75	0.86	5050	2.3	1.40	−1.42	0.45	−0.05		4.0	8.5
HD 184499	6.62	0.58	4.00	5750	4.0	1.50	−0.64	0.33	0.16		17.4	28.0
HD 187111	7.71	1.22	−0.60	4250	0.7	1.70	−1.74		−0.14	26.0	6.0	11.0
HD 188510	8.83	0.58	5.68	5500	4.4	1.50	−1.48		0.15			6.0
HD 189558	7.72	0.57	3.45	5785	3.9	1.50	−1.00		−0.09	27.0	3.5	9.0
HD 191026*	5.38	0.85	3.33	5300	3.8	1.40	−0.05		0.10	136.0	62.0	87.0
HD 194598	8.33	0.49	4.49	5890	4.0	1.50	−1.16		0.00		4.2	5.0
HD 195633	8.54	0.53	3.14	6000	3.8	1.10	−0.55	0.23	0.01	53.0	11.0	20.0
HD 196755*	5.07	0.70	2.59	5680	3.7	1.50	0.01		0.00	112.0	40.0	65.0
HD 197076*	6.45	0.62	4.77	5770	4.0	1.30	−0.19		0.01	91.0	28.0	43.0
HD 198149*	3.41	0.91	2.39	5150	3.4	1.20	−0.06		0.01	125.0		81.0
HD 201889	8.06	0.58	4.21	5600	4.1	1.20	−0.85		0.18	52.6	13.4	22.0
HD 201891	7.37	0.51	4.52	5850	4.5	1.00	−0.99	0.51	0.07	29.0	5.0	13.0
HD 204155	8.49	0.58	3.94	5600	3.8	1.00	−0.78		0.17	59.0	15.0	24.5
HD 204543	8.28		−0.43	4620	1.1	1.70	−1.79	0.40	−0.06			6.0
HD 208906	6.95	0.51	4.53	5965	4.2	1.70	−0.71	0.26	0.10	49.0	11.0	18.0
HD 215648*	4.20	0.51	3.12	6160	4.0	1.30	−0.28		0.09	73.0	20.0	31.0
HD 216143	7.80		−0.07	4500	1.0	1.60	−2.11	0.52	0.09	14.0		
HD 216174	5.43	1.18	−0.36	4400	1.9	1.50	−0.56	0.16	0.11	137.0	68.0	91.0
HD 216385	5.16	0.47	2.96	6400	4.0	1.40	−0.12		0.03	73.0	18.3	32.0
HD 219617	8.16	0.49	3.45	5870	4.0	1.50	−1.43		−0.21	7.0		
HD 221170	7.67	1.08	−0.87	4500	1.0	1.50	−2.05	0.30	−0.07	14.0		3.0
HD 221377	7.56	0.39	2.67	6000	3.4	1.20	−0.88	0.29	0.10	37.0	6.0	14.0
HD 224930	5.80	0.67	5.17	5300	4.1	0.20	−0.85		0.16		16.7	32.0
HD 345957	8.89	0.51	−1.51	5800	3.7	1.00	−1.33		−0.11			3.9
BD+174708	9.46	0.44	3.97	6000	4.0	0.70	−1.56		0.09	9.0		
BD+290366	8.76	0.58	4.87	5600	4.2	0.90	−1.01		0.18	43.0	9.8	15.4
BD+292091	10.26	0.50	5.23	5850	4.2	1.60	−1.93		0.15	5.3		
BD+302611	9.13	1.24	−0.64	4300	0.7	1.60	−1.41	0.19	−0.26		10.0	14.0
BD+413931	10.28		5.88	5450	4.6	1.00	−1.68		0.26			5.2

was refined for a number of stars using the standard formula

$$\log g = 4\log T_{\rm eff} + 0.4M_{\rm bol} + \log(M/M_\odot) - 12.5,$$

where we adopted $T_{\rm eff} = 5770$ K and $\log g = 4.40$ for the Sun. The values of $\log g$ derived in these two ways were in agreement within the errors.

We determined the microturbulence velocity $V_{\rm t}$ from the condition that the neutral-iron abundance derived from a given line be independent of the line's equivalent width.

As an estimate of the metallicity [Fe/H], we adopted the iron abundance derived using the oscillator strengths of Gurtovenko and Kostyk [28] and the WIDTH9 program of Kurucz.

The accuracies of these various parameters were $\Delta T_{\rm eff} = \pm 100$ K for the effective temperature, $\Delta \log g = \pm 0.3$ dex for the gravity, $\Delta V_{\rm t} = \pm 0.2$ km/s for the microturbulence velocity, and Δ[Fe/H] = ± 0.1 dex for the metallicity.

The values of the atmospheric parameters are presented in Table 1. Determination of the atmospheric parameters for most of the studied stars and a comparison with the results of other studies was done by us earlier in [25]. The stars whose parameters we have determined here are denoted in Table 1 by asterisks. There is good consistency between the atmospheric parameters determined by us and by other authors, and the values are generally in agreement within the errors [25]. Discrepancies are primarily due to the use of different methods for determining the parameters by some other authors.

4. DETERMINING THE SODIUM AND OXYGEN ABUNDANCES

We derived the elemental abundances using the model-atmosphere grid of Kurucz [29]. We selected the models via a standard interpolation of the model grid in $T_{\rm eff}$ and $\log g$. We selected the λ6154 Å, 6160 Å doublet lines and the λ5682 Å line for use in determining the sodium abundance (the other component of this doublet is subject to blending by telluric lines). While non-LTE corrections for the λ6154 Å, 6160 Å lines are not significant, these corrections become very important for the λ5682 Å line, as was shown earlier for various types of stars [6, 30–32].

For this reason, we increased the reliability of our estimates by taking into account departures from LTE when deriving the sodium abundance for each star. The non-LTE computations were carried out using the MULTI program [33] and the model sodium atom of [6]. The oscillator strengths were taken from [34]. We minimized the possible influence of errors in the oscillator strengths using the solar sodium abundance determined using the same method and the lines indicated above, whose equivalent widths we measured using the solar atlas [35]. We obtained for the Sun $\log A({\rm Na}) = 6.24 \pm 0.02$ on the scale $\log A({\rm H}) = 12$, in good agreement with the non-LTE estimates of [30, 33].

We carried out non-LTE calculations for all the studied stars. The resulting [Na/Fe] values are presented in Table 1, which also gives the measured equivalent widths EW (mÅ) of the sodium lines. The equivalent widths of a number of stars with strong metal deficits are very small and have large uncertainties. We estimate the error in an abundance derived from a line with $EW = 5$–10 mÅ to be about 0.15–0.20 dex, and this probably explains much of the scatter in the [Na/Fe] values for [Fe/H] < -1.5. However, several sodium lines were used for most of the stars, so that the mean error in the sodium abundances is no more than 0.05 dex.

Our [Na/Fe] values are in reasonable agreement with those of Gratton *et al.* [9], which were also obtained using a non-LTE approximation, $\Delta([{\rm Na/Fe}]_{\rm our} - [{\rm Na/Fe}]_{[8]}) = 0.02 \pm 0.13$ dex (25 common stars). Gratton *et al.* [9] used both their own EW measurements and values taken from the literature. A comparison of our [Na/Fe] values with those of [31], in which a non-LTE analysis was applied to derive the sodium abundances, primarily using resonance lines (the NaI D lines), indicates $\Delta([{\rm Na/Fe}]_{\rm our} - [{\rm Na/Fe}]_{[31]}) = 0.12 \pm 0.19$ dex (6 common stars). A detailed comparison of the results for each common star indicates that a large discrepancy (0.5 dex) exceeding the statistical errors was obtained for HD 19445. A comparison of the two data sets excluding the results for this star yields a good agreement, $\Delta([{\rm Na/Fe}]_{our} - [{\rm Na/Fe}]_{[31]}) = 0.05 \pm 0.09$ dex (5 common stars). This small offset (0.05 dex) lies within the scatter of the individual values. The sodium abundance of HD 19445 was also derived in [9] ([Na/Fe] = 0.04), and that value is in agreement with our own result within the errors ([Na/Fe] = 0.19). The equivalent widths of the λ5682 Å sodium line used to estimate the sodium abundances in our work and in [9] are 5.6 mÅ and 4.1 mÅ, respectively. This difference in the equivalent widths is apparently due to some small discrepancy between our data and those of [9]. Unfortunately, the Na abundance was derived in [31] using the NaI D-line profiles, so that we are not able to carry out a similar comparison with those data.

In order to test for the presence of a Na–O anticorrelation, we also determined the oxygen abundances using the [OI] λ6300, 6363 Å and OI λ6156, 6158 Å lines. These lines are reliable indicators of the oxygen

Table 2. Influence of uncertainty in parameters on the O and Na abundances (in dex)

Element	HD51530			HD15596			HD219617			HD122563		
	$T_{\rm eff}/\log g/V_t$/[Fe/H]											
	6100/3.8/0.8/−0.39			4750/2.5/1.0/−0.67			5870/4.0/1.5/−1.43			4570/1.1/1.2/−2.5		
	Variable parameter (see comment below)											
	1	2	3	1	2	3	1	2	3	1	2	3
O	−0.02	0.10	0.00	0.02	0.14	0.00	0.05	0.12	0.00	0.12	0.14	0.00
Na	0.05	0.02	−0.01	0.08	0.01	−0.02	0.04	0.00	0.00	0.18	0.09	0.00

Note: Columns 1–3 correspond to the variations (1) $\Delta T_{\rm eff} = +100$ K, (2) $\Delta \log g = +0.3$, (3) $\Delta V_t = +0.2$ km/s.

abundance in the range of temperatures and metallicities considered, since they are subject to only weak non-LTE effects [36]. The oxygen abundance we derived in an LTE approximation using the WIDTH9 code of Kurucz is given in Table 1.

A summary of the influence of various uncertainties in the parameters on the resulting sodium and oxygen abundances is presented in Table 2. We can see from Table 2 that the accuracy of the sodium abundances is, on average, 0.04–0.09 dex, and decreases to 0.20 dex for metal-poor cool giants. A similar situation is observed for the oxygen abundance: the mean error is 0.10–0.15 dex and increases (to 0.18 dex) as [Fe/H], the temperature, and the gravity decrease.

5. DISCUSSION

Our sodium abundances show a smaller scatter ($-0.3 <$ [Na/Fe] < 0.3) than in the earlier studies [18, 19]. The mean [Na/Fe] we obtained for 75 stars with metallicities from −3 to −0.45 is 0.06 ± 0.13. This is close to the solar value and is slightly higher than the values obtained in [7, 8]. In the critical metallicity range $-2 <$ [Fe/H] < -1, our data show only a moderate decrease of [Na/Fe] (to −0.3 dex) and do not show the appreciable decrease obtained in [20] (to −0.7 dex). The mean [Na/Fe] for 29 dwarfs with metallicities characteristic of the thick disk $-1.2 <$ [Fe/H] < -0.45 is 0.09 ± 0.07. This nearly coincides with the mean [Na/Fe] value obtained in [21] for thick-disk dwarfs.

We investigated the possibility that sodium was carried to spectroscopically detectable atmospheric layers in metal-poor giants ($\log g < 3.8$, [Fe/H] < -1) by comparing [Na/Fe] and [O/Fe] and also by comparing the Na abundances for stars in the upper and lower parts of the giant branch. Figure 1 shows that the giants we have selected do not display a Na–O anticorrelation, in contrast to metal-poor giants in globular clusters. Our estimates thus confirm the existence of differences in the behavior of the Na abundances of field giants with [Fe/H] < -1 and of metal-poor globular-cluster giants. We distinguished giants on the upper and lower giant branches using the $M_{\rm bol} - (b-y)$ relation (Fig. 2), which was applied for this same purpose in [9]. We adopted the $b-y$ values for the studied stars, presented in [25], from the SIMBAD database. The mean [Na/Fe] for the five giants with [Fe/H] < -1 located on the lower giant branch is $\langle$[Na/Fe]$\rangle = -0.05 \pm 0.11$, while the mean for the 15 stars on the upper giant branch is $\langle$[Na/Fe]$\rangle = -0.03 \pm 0.12$. This is in good agreement with the results of [9] for metal-deficient giants and testifies to an absence of any significant increase in the sodium abundance along the giant branch. Overall, the data for the giants in our sample suggest that only a negligible amount of sodium is carried to atmospheric layers in metal-poor giants.

Let us consider the behavior of [Na/Fe] for dwarfs with various metallicities [Fe/H] and compare this with the predictions of models for the chemical evolution of the Galaxy [37–39] (Fig. 3). In all these models, massive stars are the main producers of sodium and the sodium yield is determined from nucleosynthesis calculations [1]. These authors indicate that a moderate additional source of sodium is possible at [Fe/H] > -1—moderate-mass stars that synthesize sodium in the NeNa cycle—but this source is not included in the calculations. An important question that arises in calculations of models of the chemical evolution of the Galaxy and analyses of sources enriching the abundance of some element is whether the given element is a primary or secondary nuclear product. Sodium is produced as a primary element directly in the burning of carbon, and the associated sodium yield does not depend on metallicity. When sodium is formed via neutron or proton capture, the yield depends on the neutron excess, and consequently also on the metallicity. In this case, the sodium abundance

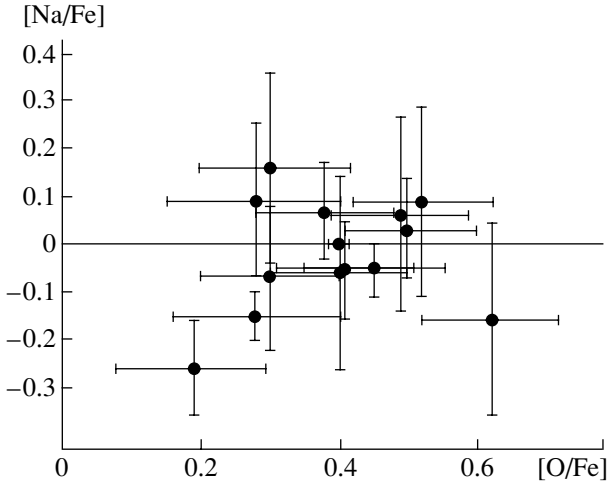

Fig. 1. Relation between [Na/Fe] and [O/Fe] for metal-poor giants ($\log g < 3.8$, [Fe/H] < -1).

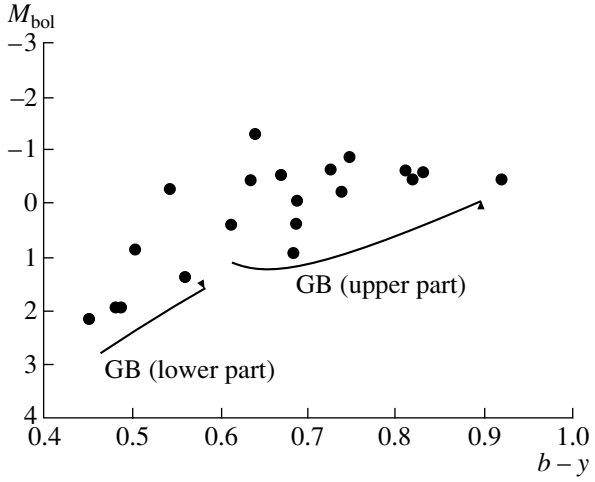

Fig. 2. Position of metal-poor giants ($\log g < 3.8$, [Fe/H] < -1) on the lower and upper parts of the giant branch (GB) in the $M_{bol}-(b-y)$ diagram.

should demonstrate a deficit relative to iron in metal-poor stars.

As we can see in Fig. 3, the calculations of [37] (dotted curve) and [38] (dashed curve) do not reproduce the observed run of [Na/Fe] with metallicity [Fe/H]. Timmes *et al.* [37] consider the sodium yield to be independent of metallicity and treat the halo and disk as parts of a single system differing only in their ages, while Gosvami and Prantzos [38] allow for metallicity dependence of the sodium yield and treat the halo and disk as two independent systems. It is curious that, when the sodium yield is taken to be independent of metallicity (upper dashed curve in Fig. 3), the sodium behavior in the model of [38] is similar to that of α elements (Mg, Si); however, this case was considered by Gosvami and Prantzos [38] to be unrealistic. The best fit to the metallicity trend of the sodium abundances we have derived is provided by the model of Samland [3] (solid curve in Fig. 3), which allows for metallicity dependence in the sodium yield and takes into account a large number of other parameters that appreciably affect the distribution of elements in the Galaxy, including sodium.

The origin of the smaller scatter of [Na/Fe] for stars with [Fe/H] > -1, for which the mean [Na/Fe] for 63 stars is 0.06 ± 0.09, than for stars with [Fe/H] < -1, for which the mean for 37 stars is [Na/Fe] $= -0.03 \pm 0.14$, remains unclear. Non-LTE corrections lower the total scatter but do not remove the larger scatter for stars with lower metallicities. The behavior of the Na abundance when [Fe/H] < -2 also remains an open question. Although a nearly solar [Na/Fe] ratio was obtained for giants with these metallicities in [7, 9] and in our own analysis, the two stars with [Fe/H] < -2 studied in [31] displayed lower values (to -0.7 dex). Does this provide evidence for inhomogeneity in the enrichment of the interstellar medium in sodium in the case of low metallicities or for different behaviors for [Na/Fe] and [Fe/H] (and hence for other sources of sodium)? The resolution of this question requires additional data, theoretical nucleosynthesis computations, and the construction of improved models for the chemical evolution of the Galaxy.

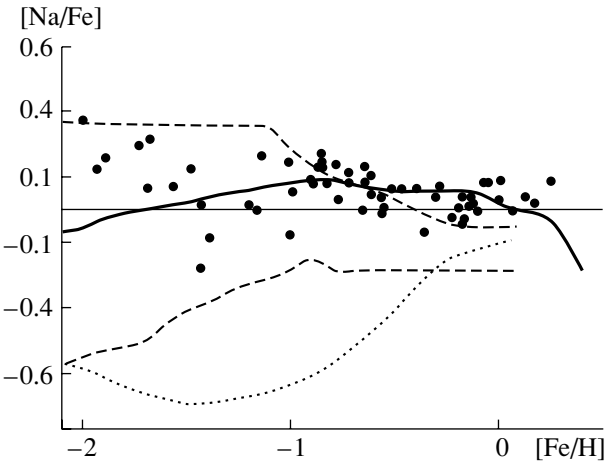

Fig. 3. Comparison of non-LTE values of [Na/Fe] obtained for dwarfs with theoretical chemical-evolution computations. The dotted curve shows the model of Timmes *et al.* [37], the dashed curve the model of Gosvami and Prantzos [38], and the solid curve, the model of Samland [3].

6. MAIN RESULTS AND CONCLUSIONS

(1) We have determined the non-LTE sodium abundances of 100 stars with a wide range of metallicities.

(2) The sodium abundances [Na/Fe] we have derived are close to the solar value and display a smaller scatter than in previous studies. However, the scatter of [Na/Fe] for stars with $[Fe/H] < -1$ is higher than for stars with $[Fe/H] > -1$.

(3) Giants with $[Fe/H] < -1$ do not display sodium overabundances and an anticorrelation between their sodium and oxygen abundances, in contrast to globular-cluster giants with $[Fe/H] < -1$. We also find no significant variations of the Na abundance along the giant branch.

(4) Our analysis does not confirm the appreciable (to -0.7 dex) decrease in the Na abundance for metallicities $-2 < [Fe/H] < -1$ reported in [20].

(5) The observed trend of [Na/Fe] with [Fe/H] is satisfactorily fit by the theoretical calculations of Samland [3], which take into account the metallicity dependence of the sodium yield and a number of other factors (inflowing gas, mixing processes in the interstellar medium, the production of energy by supernovae, etc.) when constructing models for the chemical evolution of the Galaxy.

REFERENCES

1. S. E. Woosley and T. A. Weaver, Astrophys. J., Suppl. Ser. **101**, 181 (1995).
2. P. A. Denisenkov, Astrofizika **31**, 223 (1989).
3. M. Samland, Astrophys. J. **496**, 155 (1998).
4. A. A. Boyarchuk and L. S. Lyubimkov, Izv. Krym. Astrofiz. Obs. **66**, 130 (1983).
5. A. A. Boyarchuk, I. Gubeny, I. Kurbat, *et al.*, Astrofizika **28**, 343 (1988).
6. S. A. Korotin and T. V. Mishenina, Astron. Zh. **76**, 611 (1999) [Astron. Rep. **43**, 533 (1999)].
7. C. A. Pilachowski, C. Sneden, and R. P. Kraft, Astron. J. **111**, 1689 (1996).
8. E. Carretta, R. G. Gratton, and C. Sneden, Astron. Astrophys. **356**, 238 (2000).
9. R. G. Gratton, C. Sneden, E. Carretta, and A. Bragaglia, Astron. Astrophys. **354**, 169 (2000).
10. C. Sneden, R. P. Kraft, G. E. Langer, *et al.*, Astron. J. **107**, 1773 (1994).
11. R. P. Kraft, C. Sneden, G. E. Langer, and M. D. Shetrone, Astron. J. **106**, 1490 (1993).
12. R. P. Kraft, C. Sneden, G. E. Langer, *et al.*, Astron. J. **109**, 2586 (1995).
13. G. E. Langer, R. Hoffman, and C. Sneden, Publ. Astron. Soc. Pac. **105**, 301 (1993).
14. P. A. Denissenkov, G. C. Da Costa, J. E. Norris, and A. Weiss, Astron. Astrophys. **333**, 926 (1998).
15. J. J. Cohen, Astron. J. **117**, 2434 (1999).
16. B. Edvardsson, J. Andersen, B. Gustafsson, *et al.*, Astron. Astrophys. **275**, 101 (1993).
17. Y. Q. Chen, P. E. Nissen, G. Zhao, *et al.*, Astron. Astrophys., Suppl. Ser. **141**, 491 (2000).
18. R. C. Peterson, Astrophys. J. **244**, 989 (1981).
19. A. McWilliam, G. W. Preston, C. Sneden, and S. Shectman, Astron. J. **109**, 2736 (1995).
20. A. Stephens, Astron. J. **117**, 1771 (1999).
21. J. X. Prochaska, S. O. Naumov, B. W. Carney, *et al.*, Astron. J. **120**, 2513 (2000).
22. C. Soubiran, D. Katz, and R. Cayrel, Astron. Astrophys., Suppl. Ser. **133**, 221 (1998).
23. D. Katz, C. Soubiran, R. Cayrel, *et al.*, Astron. Astrophys. **338**, 151 (1998).
24. G. A. Galazutdinov, Preprint No. 92, 52, Spec. Astrophys. Obs. (Nizhniĭ Arkhyz, 1992).
25. T. V. Mishenina and V. V. Kovtyukh, Astron. Astrophys. **370**, 951 (2001).
26. A. Alonso, S. Arribas, and C. Martinez-Roger, Astron. Astrophys. **297**, 197 (1995).
27. V. V. Tsymbol, *Model Atmospheres and Spectrum Synthesis*, ASP Conf. Ser. **108**, Ed. by S. J. Adelman, F. Kupka, and W. W. Weiss (Astronomical Society of the Pacific, San Francisco, 1996), p. 198.
28. E. A. Gurtovenko and R. I. Kostyk, *Fraunhofer Lines and the System of Solar Oscillator Strengths* [in Russian] (Naukova Dumka, Kiev, 1989).
29. R. L. Rurucz, CD-ROM 13 (1993).
30. L. I. Mashonkina, V. B. Shimanskiĭ, and N. A. Sakhibullin, Astron. Zh. **77**, 1 (2000) [Astron. Rep. **44**, 790 (2000)].
31. D. Baumuller, K. Butler, and T. Gehren, Astron. Astrophys. **338**, 637 (1998).
32. R. G. Gratton, E. Carretta, K. Eriksson, and B. Gustafsson, Astron. Astrophys. **350**, 955 (1999).
33. M. Carlsson, Uppsala Obs. Report No. 33 (1986).
34. W. L. Wiese and G. A. Martin, *Atomic Transition Probabilities. NSRDS-NBS 69*, Part II.
35. R. L. Kurucz, I. Furenlid, J. Brault, and L. Testerman, *Solar Flux Atlas from 296 to 1300 nm* (Nat. Solar. Obs. Sunspot, New Mexico, 1984).
36. T. V. Mishenina, S. A. Korotin, V. G. Klochkova, and V. E. Panchuk, Astron. Astrophys. **353**, 978 (2000).
37. F. X. Timmes, S. E. Woosley, and T. A. Weaver, Astrophys. J., Suppl. Ser. **98**, 617 (1995).
38. A. Gosvami and N. Prantzos, Astron. Astrophys. **359**, 191 (2000).

Translated by D. Gabuzda

Astronomy Reports, Vol. 47, No. 5, 2003, pp. 430–442. Translated from Astronomicheskiĭ Zhurnal, Vol. 80, No. 5, 2003, pp. 467–480.

Broad-band Multicolor Photometry and Polarimetry of Spotted Stars

I. Yu. Alekseev

Crimean Astrophysical Observatory, National Academy of Sciences of Ukraine, p/o Nauchnyĭ, Crimea, 334413 Ukraine

Received April 25, 2002; in final form, November 27, 2002

Abstract—We have confirmed the BY Dra-type variability of the active spotted stars MS Ser, LQ Hya, VY Ari, and EK Dra using simultaneous $UBVRI$ photometric and polarimetric observations. We have also reliably detected the intrinsic linear polarization of their radiation and its rotational modulation in U due to the inhomogeneous distribution of active magnetized regions over the surfaces of the stars. Modeling of the linear polarization based on the Zeeman effect indicates that all the stars display strong local magnetic fields (about 2 kG, similar to those in sunspots), with filling factors of up to 40% of the total stellar surface. The magnetized regions coincide with cool photospheric spots detected in photoelectric observations. © *2003 MAIK "Nauka/Interperiodica"*.

1. INTRODUCTION

Spottedness occurs very frequently in cool, low-luminosity stars. The axial rotation of an inhomogeneously spotted star and the slow (on characteristic time scales of the order of several months) variations in the configuration of the spots result in a rotational modulation of the brightness and slow variations of the average brightness of the star. This is known as BY Dra-type photometric variability (see, for example, the review [1]).

Like sunspots, spotted regions on red dwarfs display rather strong (on the order of 1–2 kG) magnetic fields, which result in Zeeman splitting and polarization of the absorption lines in the stellar spectrum. In broadband photometric observations, the stellar radiation appears weakly polarized due to the superposition of this effect for lines located near the band's edge.

In the late 1950s and early 1960s, broadband linear polarization was detected in solar active regions [2, 3]. Later, various attempts were made to observe the same effect in red dwarfs. Piirola [4] detected variable intrinsic linear polarization in the F8 dwarf HD 142373; from observations of the nearest stars, he also found that the degree of polarization tends to increase toward later spectral types. A similar conclusion was reached by Tinbergen and Zwaan [5]. Koch and Pfeiffer [6] considered the linear polarization of the well-known spotted star BY Dra and detected variability of the polarization in the R band, which did not correlate with the orbital rotation. Pettersen and Hsu [7] studied the polarization of 19 flare and spotted stars; their attempts to detect rotational modulation of the polarization of BY Dra and EV Lac were unsuccessful. Pettersen *et al.* [8] detected rotational modulation of the V-band polarization of HK Aqr, with the same period as that of the brightness variations. The times of maximum polarization were shifted relative to those of minimum brightness by 0.29 and 0.58 of the period. Huovelin *et al.* [9–11] studied the rotational modulation of the polarization of ten solar-type stars, including the well-known spotted star BE Cet, and compared this modulation with the variability of the CaII H and K emission lines.

Here, we study variability of the brightness and linear polarization of four stars with active chromospheres, related to spotted regions on their surfaces: MS Ser, LQ Hya, EK Dra, and VY Ari. Table 1 presents the basic parameters of these stars.

MS Ser (HD 143313) is a spectral binary consisting of K2Ve and K6Ve components [12] (or, according to other data, K2IV and G8V [13]). The earliest photometric data for this star were presented by Eggen [14]. Photometric variability was detected by Rucinski [15] and Bopp *et al.* [16], who also determined the period $P_{\rm rot} = 9\overset{\rm d}{.}60$, which is slightly different from the orbital period ($9\overset{\rm d}{.}01$). The shape of the light curve sometimes varied dramatically, with the total disappearance of the rotational modulation [17]. Alekseev and Shakhovskaya [18] confirmed the variability of MS Ser with the above period. The first polarization observations of MS Ser were made by Alekseev [19].

LQ Hya (Gl 355 = HD 82558 = BD − 10°2857) is a single young K0Ve star that has recently reached the main sequence. Observations of the LiI 6707.8 Å line indicate that the age of the star is 7.5×10^7 years

Table 1. Basic parameters of the studied stars

Star	Sp	V_{max}	ΔV	$\Delta\langle V\rangle$	$U-B$	$B-V$	$V-R$	$V-I$	P, days	$V\sin i$, km/s
MS Ser	K2IVe + G8V	8.11^m	0.15^m	0.18^m	0.61^m	0.97^m	0.69^m	1.19^m	9.60	16.0
LQ Hya	K0Ve	7.77	0.19	0.10	0.52	0.90	0.76	1.32	1.60	25
VY Ari	K(3–4)(IV–Ve)	6.68	0.30	0.27	0.60	0.92	0.72	1.33	16.4	10.2
EK Dra	G(1–2)Ve	7.48	0.11	0.06	0.03	0.60	0.54	0.95	2.70	17.3

Table 2. Comparison and standard stars

Star	Comparison star	V	$U-B$	$B-V$	$V-R$	$V-I$	Reference
MS Ser	BD+26°2762	8.08^m	0.73^m	1.08^m	0.65^m	1.28^m	Present study
	BD+26°2723	10.71	1.30	1.29	1.01	1.86	[54]
	HD 143455	7.79	1.70	1.48	1.13	1.94	[15]
LQ Hya	HD 82508	7.58	0.35	0.71	0.59	1.03	[25]
	HD 82447	6.13	0.49	1.18	0.89	1.52	[25]
VY Ari	SAO 55886	7.93	0.31	0.74	0.58	1.05	Present study
	Gl 112.0	7.88	0.48	0.83	0.63	1.13	[54]
EK Dra	HD 129380	7.53	−0.16	0.40	0.38	0.64	[55]
	HD 129798	6.23	−0.16	0.40	0.38	0.63	[55]

[20]. Its variability was discovered by Eggen [21] and Fekel *et al.* [20], from observations made in 1982. Later, the variable was observed by Strassmeier and Hall [22] and Boyd *et al.* [23]. Long-term series of observations were obtained by Jetsu [24], Cutispoto [25–29], and Strassmeier *et al.* [30, 31].

VY Ari (Gl 113.1 = HD 17433 = BD + 30°448) is the bright K(3–4)IVe component of a SB1-type spectral binary [32]. It displays a high lithium abundance and a substantial IR excess and is probably a PMS rather than a BY Dra-type variable. Photometric variability of VY Ari was detected by Chugainov [33]. Later, the star was observed by Eaton and Poe [34], Bopp *et al.* [35], Strassmeier and Bopp [36], Alekseev [37], and Strassmeier *et al.* [30, 38]. The first polarimetric observations of LQ Hya and VY Ari are our own.

EK Dra (Gl 559.1 = HD 129333 = BD + 64°1017) is a young G1Ve single star with an age of about 7×10^7 years that belongs to the Pleiades moving group. The star displays strong variable chromospheric emission lines [39], flare activity in lines of the transition region [40], strong nonthermal radio emission [41], and variable X-ray radiation from the hot corona [42–44]. Photometric activity was detected independently by Dorren and Guinan [39] and Chugainov *et al.* [45]. The long-term variability of the star has been studied by Lockwood *et al.* [46], Radick *et al.* [47], Strassmeier *et al.* [30, 38], Dorren *et al.* [48], and Scheible and Guinan [49]. Cyclic variations of the average brightness with a characteristic time scale of about 13 yrs were suspected [48]. The polarization of EK Dra has been observed by Huovelin and Piirola [50] (linear) and Elias and Dorren [51, 52] (elliptical).

2. OBSERVATIONS AND RESULTS

All of our observations were carried out with the 1.25-m telescope of the Crimean Astrophysical Observatory, equipped with Piirola's *UBVRI* photometer–polarimeter [53]. On each night, three to five observational cycles were carried out, during which observations were made of the comparison star, the variable, a standard star, and the comparison star. Each pointing at the comparison and standard stars yielded a set of eight values, corresponding to different positions of the analyzer. We obtained four such sets from each pointing at the program stars. The integration time for each reading was 10 s. The sky background was measured separately before each pointing. Thus, we obtained simultaneously the brightness and color indices of the star, as well as the Stokes parameters in all five bands. With this procedure, the errors in the brightness and color indices

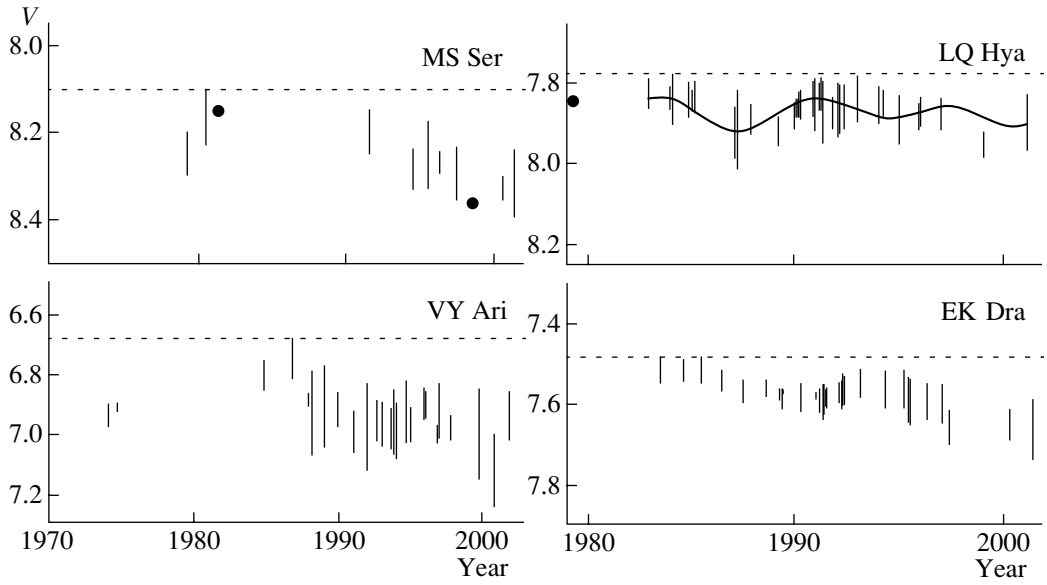

Fig. 1. Master V light curves of the studied stars.

do not exceed $0^m.01$, while the errors in the Stokes parameters P_x and P_y do not exceed 0.02% in the U band and 0.01% in the other bands. Table 2 presents the parameters of the comparison and standard stars.

2.1. Photometry

Figure 1 presents the master V light curves for the studied stars derived from our observations and published data.

Photometric observations of **MS Ser** were carried out regularly, starting from 1991 [18, 19, 56]. Over the total time of the observations (both new and previously published), the amplitude of the rotational modulation ΔV varied from $0^m.05$ to $0^m.15$, while the average brightness of the star varied by $0^m.18$. According to our observations, $\Delta V = 0^m.06$ in 2000, with the average brightness of the star being $8^m.33$, while $\Delta V = 0^m.14$ in 2001, with $\langle V \rangle = 8^m.32$. The variable reached its maximum brightness $V_{\max} = 8^m.11$ in 1980 [16]. In all our calculations for this star, we will adopt this value for the unperturbed photospheric brightness. The corresponding absolute brightness of the unspotted star is $M_V = 3^m.69$ for the primary component. The color indices of MS Ser derived from our observations and taken from the literature do not vary significantly. The entire set of photometric observations of the star indicate that the variations of its $UBRI$ brightness depend linearly on the V brightness, as is characteristic of all BY Dra stars [56]. The corresponding linear-regression coefficients for MS Ser are $dU/dV = 1.08 \pm 0.03$, $dB/dV = 1.08 \pm 0.01$, $dR/dV = 0.84 \pm 0.03$, and $dI/dV = 0.67 \pm 0.02$. Based on this linearity and $V_{\max}$, we can easily estimate the color indices of the unspotted star: $U - B = 0^m.61$, $B - V = 0^m.97$, $V - R = 0^m.69$, and $V - I = 1^m.19$ for the primary. The color indices and absolute magnitude M_V confirm the spectral type K2IV determined by Osten and Saar [13]; thus, MS Ser is an RS CVn rather than a BY Dra star.

LQ Hya was observed by us in 1994, 1995, 1996, 1999, and 2001 [56, 57]. Over the entire time it has been observed, the amplitude of its rotational modulation has ranged from $0^m.04$ in 1990 to $0^m.19$ in 1987, with small variations of the average brightness (by $0^m.10$). The variation amplitude was $\Delta V = 0^m.14$ in 2001, with the average brightness being $\langle V \rangle = 7^m.90$. A maximum brightness of $V_{\max} = 7^m.77$ was reached in 1984 and 1991 [20, 31]; the corresponding absolute magnitude of the unspotted photosphere is $M_V = 6^m.44$. Cyclicity of the brightness variations of LQ Hya was suspected in [24, 30], described by two characteristic time scales 6.75 and 11.4 yrs [58] (solid curve in Fig. 1). The linear-regression coefficients $dU/dV = 1.29 \pm 0.15$, $dB/dV = 1.10 \pm 0.11$, $dR/dV = 0.74 \pm 0.01$, and $dI/dV = 0.67 \pm 0.01$ yield color indices for the quiescent photosphere $U - B = 0^m.52$, $B - V = 0^m.90$, $V - R = 0^m.76$, and $V - I = 1^m.32$, corresponding to spectral type $K2V$.

VY Ari was regularly observed from 1991 to 2001 [37, 56, 59]. The amplitude of the rotational modulation ranged from $0^m.02$ in 1974 and 1987 [33, 36] to $0^m.28$–$0^m.30$ in 1988–1989 and 1999 [36, 56, 59], with strong variations of the average brightness by $0^m.27$. In 2001, the variation amplitude was $\Delta V = 0^m.16$, with the average brightness being $\langle V \rangle = 6^m.94$. Photometrically, VY Ari is one of the most active stars

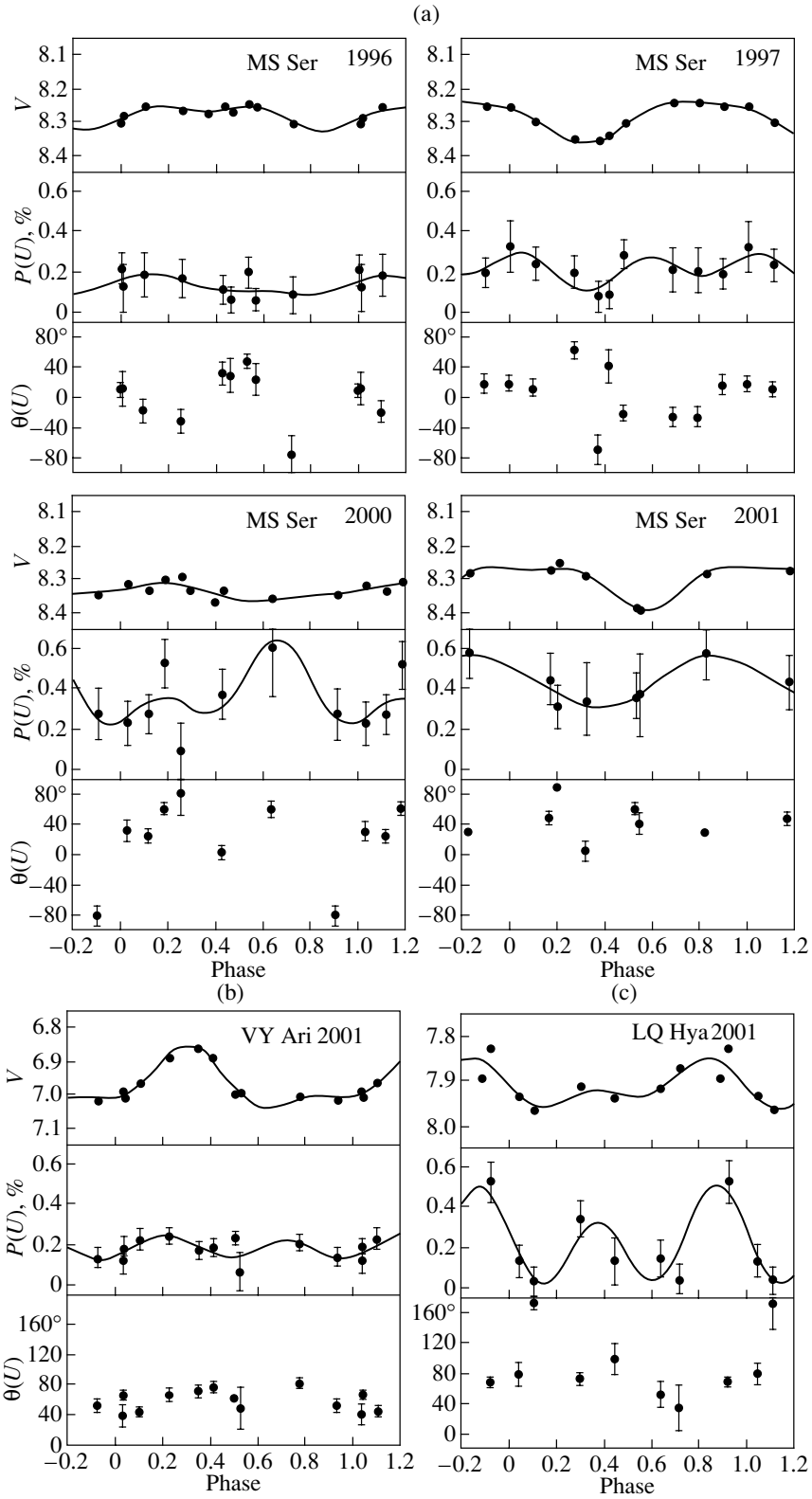

Fig. 2. V Brightness and the degree and position angle of the linear polarization in the U band as functions of the phase of the axial rotation of the stars. (a) MS Ser, (b) VY Ari, (c) LQ Hya.

Table 3. Linear polarization of the studied stars in the U band

Star, epoch	$\langle P_x \rangle$	$F_{\rm var}$, %	ΔP_x, %	$\langle P_y \rangle$	$F_{\rm var}$, %	ΔP_y, %	P_s	$\Delta\phi$
MS Ser, 1996	0.064	28.2	0.22	0.023	63.1	0.33	0.170 ± 0.016	0.25
MS Ser, 1997	0.077	99.6	0.48	0.046	87.4	0.48	0.241 ± 0.018	0.28
MS Ser, 2000	0.033	>99	0.74	0.192	88	0.60	0.380 ± 0.062	0.07
MS Ser, 2001	0.016	>99	0.67	0.279	>99	0.47	0.399 ± 0.039	0.25
LQ Hya, 2001	−0.150	99.7	0.30	0.157	99.6	0.23	0.284 ± 0.093	0.25
VY Ari, 2001	−0.089	>99	0.15	0.128	71	0.11	0.185 ± 0.014	0.45
EK Dra, 2001	−0.105	89		0.116	96		0.203 ± 0.015	

Table 4. Models for the spottedness of MS Ser

Epoch	$\Delta V_{\max}$	ΔV	ϕ_0	$\Delta\phi$	$f_{\min}$	β_V	$S_{\max}$, %	$S_{\min}$, %	Reference
1980.5	0.00^m	0.13^m	41°	17°	0.00	0.11	11.0	3.7	[16]
1991.5	0.01	0.15	38	18	0.00	0.11	12.2	4.1	[18]
1994.5	0.06	0.18	24	18	0.05	0.11	12.1	4.5	[19]
1995.5	0.08	0.15	20	16	0.17	0.11	10.8	5.2	[19]
1996.3	0.13	0.05	19	11	0.63	0.13	8.8	7.0	[19]
1997.3	0.13	0.12	17	16	0.38	0.12	11.5	7.3	[19]
2000.3	0.19	0.06	16	15	0.68	0.12	11.6	9.6	Present study
2001.5	0.14	0.14	15	17	0.36	0.11	12.4	7.7	Present study

known [1]. It has been suspected of cyclic variability on a characteristic time scale $P_{\rm cyc} \approx 14$–15 yrs [30, 40, 58]. The maximum brightness $V_{\max} = 6^m\!.68$ was reached in 1986 [35], and the corresponding absolute magnitude of the unspotted star is $M_V = 6^m\!.68$. The linear-regression coefficients for VY Ari $dU/dV = 1.27 \pm 0.04$, $dB/dV = 1.11 \pm 0.02$, $dR/dV = 0.79 \pm 0.03$, and $dI/dV = 0.64 \pm 0.01$ yield the color indices for the unspotted photosphere $U - B = 0^m\!.60$, $B - V = 0^m\!.92$, $V - R = 0^m\!.72$, and $V - I = 1^m\!.33$. The absolute magnitude M_V and the color indices correspond to spectral type K3V.

For **EK Dra**, we obtained only scattered brightness measurements in 2000 and 2001. The amplitudes of the rotational modulation in these seasons were $0^m\!.08$ and $0^m\!.15$, respectively, with the average brightness being $\langle V \rangle = 7^m\!.65$–$7^m\!.66$ (Fig. 1). Over the entire time the star has been observed, the amplitude of its rotational modulation has ranged from $0^m\!.02$ in 1989 [39] to $0^m\!.12$ in 1995 [46], accompanied by variations of the average brightness by $0^m\!.15$. The maximum brightness $V_{\max} = 7^m\!.48$ was observed in 1985 [39]. The corresponding absolute magnitude of the quiescent photosphere is $M_V = 4^m\!.89$. The linear-regression coefficients $dU/dV = 1.33 \pm 0.07$, $dB/dV = 1.31 \pm 0.05$, $dR/dV = 0.88 \pm 0.07$, and $dI/dV = 0.79 \pm 0.05$ yield the color indices for the unspotted photosphere $U - B = 0^m\!.03$, $B - V = 0^m\!.60$, $V - R = 0^m\!.54$, and $V - I = 0^m\!.95$. The absolute magnitude M_V and the color indices correspond to spectral type G(2–3)Ve.

2.2. Linear Polarimetry

We carried out polarimetric observations of **MS Ser** regularly in 1996 (nine nights), 1997 (nine nights), 2000 (seven nights), and 2001 (six nights). The results of the 1996 and 1997 observations were published in [19]. In all seasons, the radiation of MS Ser was weakly polarized in all bands. Variability of the polarization was reliably detected in all bands in 2000, and in the UBV bands in 2001. The maximum variability of the polarization was observed in the U band. The variations of the Stokes parameters in this band were 0.22% for P_x and 0.33% for P_y in 1996, 0.48% for P_x and 0.48% for P_y in 1997, 0.74% for P_x and 0.60% for P_y in 2000, and 0.67% for P_x and 0.47% for P_y in 2001. Figure 2 presents

Table 5. Models for the spottedness of LQ Hya

Epoch	$\Delta V_{\max}$	ΔV	ϕ_0	$\Delta\phi$	$f_{\min}$	β_V	$S_{\max}$, %	$S_{\min}$, %	Reference
1983.00	0.014^m	0.075^m	33°	12°	0.00	0.37	7.6	2.5	[20]
1984.05	0.020	0.076	32	12	0.00	0.36	7.8	2.6	[21]
1984.07	0.000	0.119	32	16	0.00	0.35	10.4	3.5	[20]
1984.95	0.020	0.088	31	13	0.00	0.36	8.6	2.9	[22]
1985.10	0.034	0.055	31	10	0.20	0.37	7.1	3.6	[22]
1985.23	0.022	0.072	32	12	0.03	0.37	7.7	2.8	[22]
1987.12	0.078	0.120	25	20	0.23	0.33	13.7	7.1	[24]
1987.27	0.053	0.189	24	25	0.03	0.31	16.1	5.8	[24]
1987.95	0.083	0.066	27	15	0.41	0.35	11.0	7.2	[25]
1989.20	0.110	0.080	25	18	0.45	0.34	13.4	9.1	[26]
1990.03	0.065	0.075	28	15	0.30	0.35	10.6	6.1	[24]
1990.16	0.056	0.047	30	11	0.39	0.37	8.3	5.3	[24]
1990.2	0.05	0.04	30	10	0.41	0.37	7.1	4.6	[27]
1990.29	0.042	0.063	31	12	0.22	0.37	8.6	4.4	[24]
1990.87	0.011	0.099	32	15	0.00	0.36	9.8	3.3	[24]
1990.96	0.012	0.114	31	16	0.00	0.35	10.5	3.5	[24]
1991.10	0.010	0.090	32	13	0.00	0.35	8.4	2.8	[31]
1991.15	0.010	0.060	34	9	0.00	0.37	6.1	2.0	[31]
1991.3	0.04	0.08	30	14	0.15	0.36	9.5	4.3	[28]
1991.36	0.014	0.154	29	21	0.00	0.34	13.5	4.5	[24]
1991.83	0.056	0.085	28	15	0.22	0.35	10.6	5.5	[24]
1992.05	0.029	0.133	28	19	0.00	0.34	12.0	4.0	[24]
1992.18	0.034	0.125	28	18	0.02	0.34	11.8	4.1	[24, 29]
1992.30	0.027	0.113	30	17	0.00	0.35	11.1	3.7	[24]
1993.0	0.03	0.10	30	16	0.03	0.35	10.2	3.7	[30]
1993.02	0.01	0.07	34	11	0.00	0.37	7.4	2.5	[70]
1994.0	0.01	0.12	31	17	0.00	0.35	10.9	3.6	[30]
1994.30	0.03	0.09	31	15	0.05	0.36	9.8	3.7	[30, 56, 57]
1995.0	0.08	0.08	27	17	0.35	0.35	11.9	7.2	[30]
1996.0	0.08	0.02	30	10	0.72	0.37	8.2	7.0	[30]
1997.0	0.06	0.06	29	13	0.34	0.36	9.3	5.6	[38]
1999.2	0.15	0.05	24	17	0.67	0.33	13.7	11.2	[57]
2001.1	0.06	0.14	26	21	0.12	0.33	14.3	6.2	[57]

the dependence of the degree of polarization P and the polarization position angle θ on the phase of the axial rotation of the star, together with its light curve. The phase shift between the minimum brightness and maximum degree of polarization was 0.25 in 1996 and 2001, 0.28 in 1997, and 0.07 in 2000, in fractions of the period. Table 3 presents the polarimetric observations. For each epoch, we indicate the average Stokes parameters P_x and P_y, the probability $F_{\rm var}$ that a given parameter was variable, and the amplitude of its variations. Table 3 also contains the value P_s introduced by Houvelin (the degree of polarization averaged over all values differing from zero by more than 2σ), which can be considered an estimate for the maximum observed degree of polarization, and the phase difference between the minimum brightness and maximum degree of polarization.

The linear polarization of **LQ Hya** was measured in 2001. The star's radiation is weakly polarized in all bands. The Stokes parameters were confidently found to be variable, with amplitudes of 0.30% for P_x and 0.23% for P_y. Figure 2c presents the dependence of the degree and position angle of the linear polarization of LQ Hya on the rotational phase, together with the light curve. The rotational modulation of the polarization is evident; the phase shift between the maximum degree of polarization and the minimum brightness is 0.25 of the period.

We carried out isolated measurements of the polarization of **VY Ari** in 1996–2000 (six nights) and regular observations in 2001 (ten nights). Variability was firmly detected in all bands, both season-to-season variations for the isolated observations and the rotational modulation of the Stokes parameters in 2001. The amplitude of the rotational modulation was 0.15% for P_x and 0.11% for P_y. The phase shift between the maximum degree of polarization and minimum brightness is about 0.45 of the period. Note that, in all cases, the phase shift is consistent with that expected for magnetized spots [60].

Measurements of the linear polarization of **EK Dra** were obtained during seven nights in 2001. The radiation of EK Dra is polarized in all bands; variability of the Stokes parameters was also firmly detected. The degree of the linear polarization is consistent with the results of [51, 52] and substantially exceeds the values obtained for the UBV observations of [50].

3. THE MODELING

Doppler mapping is currently considered the most promising technique for mapping stellar surfaces. However, this method has some shortcomings. It is highly sensitive to errors in the rotational velocity $v\sin\iota$ and to the set of spectral lines used. In addition, it requires spectroscopic observations of rapidly rotating ($v\sin\iota > 15$ km/s) stars with high spectral resolution and large signal-to-noise ratio. Therefore, unlike photometric techniques, Doppler mapping imposes tight restrictions on the detectors used and the selection of the program stars.

A cool spotted region on the surface of a binary gives rise to a deficit of the radiation flux at the wavelength λ in accordance with the formula

$$\Delta m_\lambda = -2.5lg((1-(a_\lambda I + b_\lambda J)/(1-u^{ph}/3)) \times (1-X_\lambda)+X_\lambda), \quad (1)$$

where

$$X_\lambda = L_2/(L_1+L_2), \quad (2)$$

and L_1 and L_2 are the luminosities of the system's components at the given wavelength [61]. This relation contains two temperature parameters

$$a_\lambda = 1 - u_\lambda^{ph} - (1-u_\lambda^{sp})\beta_\lambda, \quad (3)$$

$$b_\lambda = u_\lambda^{ph} - u_\lambda^{sp}\beta_\lambda, \quad (4)$$

and two geometrical parameters: the area of the spots projected onto the plane of the sky in fractions of the visible disk of the star

$$I = \frac{1}{\pi}\int \cos\alpha \sin\theta d\theta d\phi \quad (5)$$

and the average cosine of the angular distance α between the geometrical center of gravity of the spot and the center of the stellar disk

$$J = \frac{1}{\pi}\int \cos^2\alpha \sin\theta d\theta d\phi. \quad (6)$$

In (5) and (6), we integrate over the visible part of the spotted surface (θ and ϕ are the polar angle and latitude of a point on this surface); u_λ are the limb-darkening coefficients and β_λ is the ratio of the brightnesses of the spot and the quiescent photosphere. The difference Δm_λ is measured relative to the brightness of the unspotted photosphere.

To determine the area and temperature of the spotted region, the brightness of the unspotted photosphere and the relations between the brightness differences Δm at various wavelengths (derived from observations) must be known; in addition, we must initially assume a configuration for the spotted regions.

3.1. The Zonal Model

Traditional algorithms inevitably yield large, high-latitude spots in all stars, independent of their spectral type and luminosity, in sharp contradiction of the pattern displayed by sunspots. On the other hand, Eker [62, 63] showed that the photometric effect of

Table 6. Models for the spottedness of EK Dra

Epoch	$\Delta V_{\max}$	ΔV	ϕ_0	$\Delta\phi$	$f_{\min}$	β_V	$S_{\max}$, %	$S_{\min}$, %	Reference
1983.5	0.005^m	0.058^m	53°	12°	0.00	0.07	7.9	2.6	[39,51]
1984.6	0.009	0.043	53	9	0.00	0.07	6.0	2.0	[39]
1985.5	0.000	0.062	55	14	0.00	0.07	9.4	3.1	[39]
1986.5	0.030	0.041	45	8	0.17	0.08	5.9	2.8	[39]
1987.5	0.053	0.048	45	12	0.29	0.07	8.7	4.9	[39]
1988.6	0.056	0.042	45	12	0.35	0.07	8.4	5.1	[39]
1989.29	0.079	0.030	44	12	0.57	0.07	9.1	6.9	[39]
1989.38	0.082	0.040	43	13	0.49	0.07	10.0	7.1	[39]
1989.45	0.085	0.020	44	11	0.69	0.07	8.7	7.3	[39]
1990.29	0.066	0.060	43	15	0.29	0.07	10.4	5.9	[39]
1991.08	0.087	0.020	43	11	0.70	0.07	8.6	7.2	[39]
1991.16	0.078	0.055	43	15	0.37	0.07	11.1	7.0	[39]
1991.28	0.082	0.060	42	16	0.37	0.07	11.5	7.2	[39]
1991.30	0.065	0.054	44	14	0.32	0.07	10.1	5.9	[39]
1991.35	0.063	0.084	43	18	0.17	0.07	12.6	5.9	[39]
1991.39	0.071	0.063	43	16	0.30	0.07	11.2	6.4	[39]
1991.44	0.077	0.040	43	13	0.48	0.07	9.6	6.7	[39]
1991.5	0.072	0.050	43	14	0.38	0.07	10.0	6.4	[45]
1992.12	0.063	0.055	44	14	0.30	0.07	10.0	5.8	[39]
1992.21	0.058	0.062	44	15	0.20	0.07	10.2	5.4	[39]
1992.29	0.042	0.080	45	17	0.05	0.07	10.9	4.2	[39]
1992.36	0.047	0.070	45	15	0.13	0.07	10.4	4.6	[39]
1993.09	0.030	0.069	47	14	0.00	0.07	9.3	3.1	[39]
1994.3	0.032	0.090	45	17	0.00	0.07	11.1	3.7	[30]
1995.2	0.027	0.100	45	19	0.00	0.07	12.0	4.0	[30]
1995.4	0.047	0.120	42	23	0.00	0.07	14.3	4.8	[30]
1995.5	0.057	0.110	41	21	0.07	0.07	13.6	5.3	[30]
1996.3	0.077	0.080	42	19	0.25	0.07	13.0	7.0	[30]
1997.0	0.067	0.100	41	20	0.14	0.07	13.5	6.1	[55]
1997.4	0.127	0.100	37	23	0.36	0.06	16.6	10.3	[55]
2000.4	0.13	0.08	38	22	0.44	0.05	15.7	10.6	Present study
2001.4	0.10	0.15	35	26	0.17	0.06	17.4	8.3	Present study

a circular polar spot is the same as that of a chain of small spots homogeneously distributed in latitude. Eaton *et al*. [64] demonstrated that the photometric behavior of any star can be described using a large number (5–40) of small, low-latitude spots.

Alekseev and Gershberg [1, 65, 66] showed that a collection of spotted regions on a star can be represented by two belts of spots symmetrically placed relative to the equator, occupying regions with latitudes from $\pm\phi_0$ to $\pm(\phi_0 + \Delta\phi)$. Within the belts,

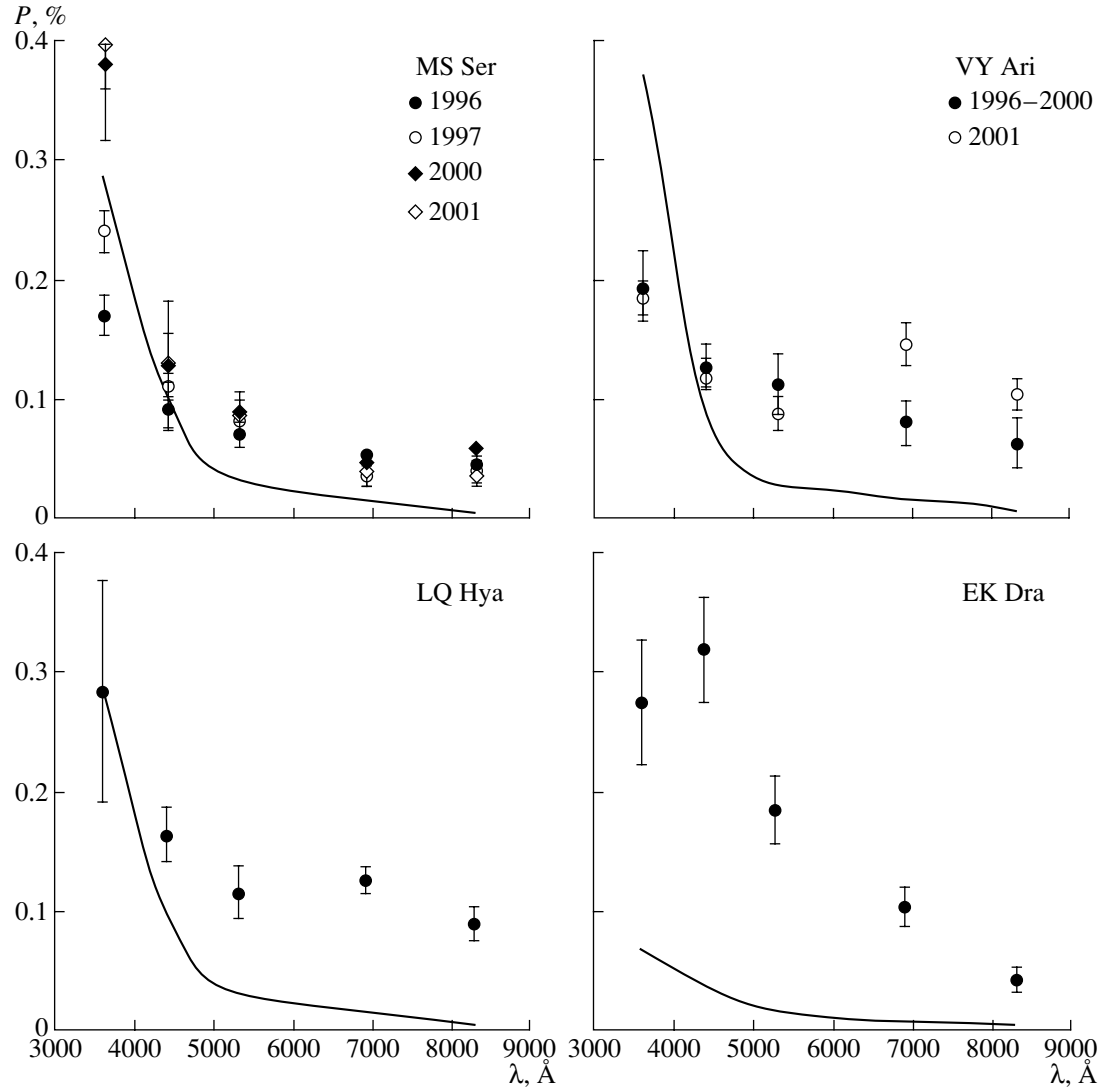

Fig. 3. Wavelength dependence of the degree of linear polarization. The points represent the observed estimates for the maximum polarization P_s, and the solid line shows the expected theoretical dependence.

the filling factor varies with longitude from unity (at the phase of minimum brightness of the star) to $f_{\min}$ ($0 < f_{\min} < 1$) at the phase of maximum brightness. We applied this zonal model to 25 active dwarfs with various spectral types (G1Ve–M4.5Ve), rotational velocities (4–25 km/s), and luminosities ($M_V = 4^m.80$–$12^m.24$) [19, 56, 57, 59], and, in all cases, obtained qualitative consistency with the pattern of sunspots.

Tables 4–6 present the results of our zonal-spottedness model calculations for the program stars. The input variables for these models are the difference between the seasonal brightness maximum and the maximum brightness over the entire observation time $\Delta V_{\max}$ and the amplitude of the rotational modulation of the brightness ΔV (the second and third columns of the Tables). To take into account brightness variations in the other bands, we used the coefficients dB/dV, dR/dV, dI/dV as input parameters. The other two parameters were the temperature of the stellar photosphere T_{phot} and the inclination of the rotational axis ι. The results of the model calculations—ϕ_0, $\Delta\phi$, $f_{\min}$, and β_V—are presented in columns 4–7. These are used to derive the areas of the spots in the darkest and brightest hemispheres $S_{\max}$ and $S_{\min}$ (columns 8, 9), as percents of the total stellar surface.

In the modeling for **MS Ser**, we assumed the inclination of the rotational axis to be $i \approx 60°$ [19]. This estimate was obtained from the star's rotational velocity $v \sin i = 15$ km/s [13], radius $R = 3.50 R_\odot$ [13], and rotational period. The photospheric temperature $T_{\text{phot}} = 4600$ K was derived from the $V-R$ and $V-I$ color indices of the unperturbed photosphere and coincides with the temperature determined in [13]. We

used a four-parameter model to describe the photometric variability of the star, in which the distance from the belts of spots to the equator ϕ_0 varied from 15° to 41°, the width of the belts $\Delta\phi$ from 11° to 18°, and the parameter $f_{\min}$ from 0.00 to 0.68. This yields areas for the spotted regions that do not exceed 21% of the total stellar surface. The spotted regions are rather cool: their contrast β_V is 0.11, which corresponds to a difference between the temperatures of the photosphere and spots of 1300 K.

To estimate the inclination i for **LQ Hya**, we used the parameters of the star presented by Jetsu [24]—$R = 0.79R_\odot$, $v \sin i = 25 \pm 2$ km/s, $P_{\rm rot} = 1\overset{\rm d}{.}601136$—and estimated $T_{\rm phot}$ using the color indices. The resulting values $i = 70°$, $T_{\rm phot} = 5000$ K correspond to the values used for Doppler mapping in other studies [31, 67–71]. We were able to refine the coefficients dB/dV, dR/dV, dI/dV using our 1996–2001 observations and the data published in [29, 30, 38]; as a result, the latitude distribution of the spots differs from that presented in [56].

Our model has four parameters, with the distance ϕ_0 from the equator to the belt of spots ranging from 24° to 34°, the width of the belt $\Delta\phi$ from 9° to 25°, and the inhomogeneity parameter $f_{\min}$ from 0.00 to 0.67. These geometrical parameters yield a total area for the spotted regions of $S_{\max} + S_{\min}$, which reaches 22.5% of the total stellar surface. The spot contrast β_V ranges from 0.31 to 0.37, corresponding to spots that are 800 K cooler than the photosphere [57]. The combined areas of the spots are consistent with the results obtained from light-curve modeling [31] and Doppler mapping [31, 67–71]. The consistency for the temperature difference between the spots and quiescent photosphere is worse. The light-curve modeling of [31] and Doppler mapping of [67–70] predict spots that are 200 K warmer than ours, while the Doppler mapping carried out by Berdyugina *et al.* [71] and observations of the TiO band [72] yield spot temperatures that are consistent with our estimates. Our latitude distribution for the spots is in reasonable agreement with the results of Doppler mapping, which predicts middle- and low-latitude spots. However, the Doppler mapping also yields circumpolar spots, which are not seen in our results. We compared the average latitudes of our spots $\langle\phi\rangle = \phi_0 + \Delta\phi/2$ with the photometric periods determined by Jetsu [24] and Strassmeier *et al.* [30, 31, 38]. This indicated an increase of $P_{\rm phot}$ with increasing $\langle\phi\rangle$, due to the differential rotation of LQ Hya with $D_r = 0.09$.

The inclination ι and photospheric temperature of **VY Ari** are presented by Strassmeier and Bopp [36]. Here, we continue the modeling of the spottedness of the star carried out in [59], supplemented with data obtained during the 2001.9 season. The best fit to the photometric variability is provided by a model in which ϕ_0 ranges from 6° to 22° (in 2001, $\phi_0 = 9°$), the width of the belt of the spots $\Delta\phi$ from 11° to 37° (in 2001, $\Delta\phi = 21°$), and the parameter $f_{\min}$ from 0.00 to 0.91 (in 2001, $f_{\min} = 0.41$). The maximum degree of spottedness reaches 40.6% of the total surface of the star. The spot contrast $\beta_V = 0.09$–0.16 corresponds to a temperature difference of 1260–1410 K [59]. The temperature and combined areas of the spots are consistent with the results of light-curve modeling by Strassmeier and Bopp [36]. A comparison of the average latitudes of the spots $\langle\phi\rangle$ and the photometric periods $P_{\rm phot}$ determined by Strassmeier *et al.* [30, 36, 38] reveals solar-type differential rotation with $D_r = 0.05$.

When modeling the spottedness of **EK Dra**, we used the axis inclination and temperature presented by Strassmeier and Rice [55]. The photometric behavior of the star is also described by a four-parameter model in which the distance from the equator to the belt of spots is $\phi_0 = 37°$–$55°$, the width of the belt is $\Delta\phi = 8°$–$23°$, and the inhomogeneity parameter is $f_{\min} = 0.00$–0.70 [56]. These values correspond to the total area of the spots reaching 27% of the stellar surface. The relative brightness of the spots β_V is 0.07 of the photospheric brightness, which is close

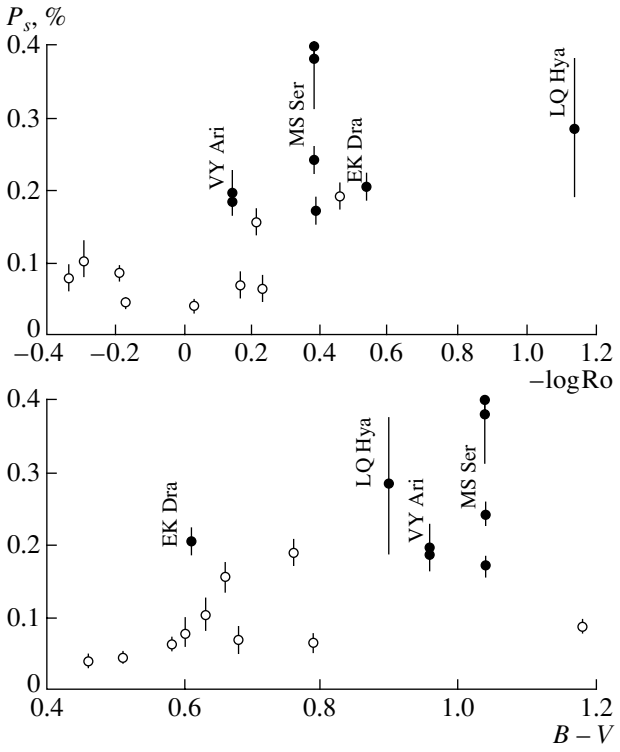

Fig. 4. Dependence of the degree of polarization P_s on the color index $B - V$ and Rossby number. The points represent our data, and the hollow circles, the data of Huovelin *et al.* [10].

to the solar value. This corresponds to spots that are $\Delta T = 2200$ K cooler than the adjacent photosphere (also close to the effective temperatures of sunspots). The latitude distribution of the spots is in poor agreement with the Doppler mapping of [55], which, as for LQ Hya, predicts the presence of circumpolar features.

3.2. Polarimetry

Here, we will consider primarily the magnetic mechanism for the creation of linear polarization, since the effects of binarity and Thomson scattering can be neglected for spotted red dwarfs. The first calculations were carried out in [74–77], which assumed that the degree of polarization depends linearly on the size of the magnetized region. However, Huovelin and Saar [60, 78] demonstrated that this dependence becomes nonlinear for large regions. For example, for a single circular region, the degree of linear polarization is proportional to a factor A, which depends on the area of the region roughly as

$$A(S) = -2.128 \times 10^{-4} + 1.076S - 4.812S^2 + 9.058S^3 - 6.26S^4. \quad (7)$$

They also calculated a grid of expected degrees of polarization in the $UBVRI$ bands for stars with temperatures from 4000 to 5000 K and log g from 2.0 to 4.5. We used these results to estimate the parameters of the magnetized regions.

Figure 3 presents the degree of polarization P_s for the program stars in the $UBVRI$ bands averaged over all cases when it differs from zero by more than 2σ. The maximum possible degree of polarization for a total spot area of $S \approx 24\%$ is also plotted, derived from the calculations of [78] for stars with the corresponding spectral types and characteristic magnetic fields of 2–4 kG. For MS Ser, LQ Hya, and VY Ari, the observed degree of linear polarization in the VRI bands is higher than expected theoretically. This suggests the presence of a supplementary source of polarization, most likely the remnant of a circumstellar disk. The observed B-band degrees of polarization for all three stars are consistent with the maximum theoretical value for $S = 24\%$. For MS Ser, the U-band degree of polarization in 1996 corresponds to a filling factor for the magnetized regions of $S = 6\%$, for an area of dark spots roughly equal to 16%. In 1997, the magnetic field occupied approximately 11% of the stellar surface, while cool spots covered about 19% of the surface; in 2000 and 2001, the magnetic-field filling factor was $S \approx 24\%$ and the total areas of cool spots were 21% and 20% of the surface, respectively. For LQ Hya, the U-band degree of polarization corresponded to a filling factor of $S = 17\%$, for a total area of the spots of 20%. For VY Ari, $S = 63\%$, with the area of the spots ranging from 20 to 40% of the total stellar surface.

The observed degree of linear polarization of EK Dra drastically exceeds the expected values. However, Elias and Dorren [51, 52] noted that the detected polarization is not associated with the photometric behavior of the variable and cannot be due to the magnetic mechanism. One possible additional source of polarization is the presence of circumstellar matter.

Thus, our polarization observations are consistent with our estimates for the area of the spotted regions on the surfaces of the studied stars: the magnetic-field filling factors are roughly equal to the total areas occupied by the spots.

4. CONCLUSIONS

We have presented the results of simultaneous photoelectric and polarimetric $UBVRI$ observations of the four active spotted stars MS Ser, LQ Hya, VY Ari, and EK Dra.

(1) Our photometric observations substantially add to previously existing data on the long-term variability of these stars. Our observations of LQ Hya, EK Dra, and VY Ari are consistent with the previously suspected cycles of activity in these stars. We have estimated the absolute magnitudes of all the studied stars and the color indices of their unspotted photospheres, which we identify with the brightest state of the stars. We have also refined the position of the stars in the color–luminosity diagram. The classification of MS Ser suggested by Osten and Saar [13] has been confirmed.

(2) We have modeled the spottedness of the stars based on all previously published and our new photometric observations. Our four-parameter zonal model describes the photometric variability of the stars with sufficient accuracy. The total area of the spots on MS Ser, LQ Hya, VY Ari, and EK Dra reaches 21, 22, 41, and 27% of the total stellar surfaces, with the difference between the temperatures of the quiescent photosphere and the spots being 1300, 800, 1300, and 2200 K, respectively. These results are consistent with those obtained by other authors from light-curve modeling, Doppler mapping, and observations of the TiO band.

(3) The spots on all the stars are located at middle latitudes. For LQ Hya and EK Dra, this is consistent with the results of Doppler mapping, which predict the presence of middle- and low-latitude spots. However, circumpolar spots can yield the same results for these stars, in contradiction with both our calculations and the pattern displayed by sunspots. Our latitude distributions for the spots on these stars

are in good agreement with theoretical modeling of ascending magnetic flux tubes [79, 80]. The agreement between the Doppler-mapping results and our calculations is much poorer [55].

(4) A comparison of the average latitudes of spots on LQ Hya and VY Ari with their photometric periods indicates that both stars display solar-type differential rotation with $D_r = 0.09$ and $D_r = 0.05$, respectively (for the Sun, this factor is approximately 0.19).

(5) We have reliably detected weak linear polarization and rotational modulation of the Stokes parameters for three stars—MS Ser, LQ Hya, and VY Ari—for the first time, presumably due to the magnetic fields associated with the spotted regions. Our estimates of the magnetic-field filling factors indicate that the areas occupied by magnetized regions are in agreement with those covered by dark spots in the same seasons. Note, however, that the magnetic-field filling factors may be underestimated. We used estimates obtained for a single circular spot, whereas the zonal distribution of the magnetic field may yield a substantially different result. In addition, the magnetometric observations of Saar [35, 81] yield substantially larger filling factors for LQ Hya and VY Ari (50–70%).

(6) The maximum observed VRI polarization of MS Ser, LQ Hya, and VY Ari and the observed $UBVRI$ polarization of EK Dra exceed the theoretical values expected for Zeeman polarization models. This is probably due to the presence of a supplementary source of linear polarization, such as the remnant of a circumstellar disk.

(7) We have compared our estimates for the maximum observed degree of polarization P_s in the U band for MS Ser, LQ Hya, and VY Ari with observations of ten solar-type red dwarfs carried out using the same equipment and a similar technique by Huovelin *et al.* [10]. Our results are consistent with the dependences of the degree of polarization on spectral type and Rossby number (Fig.4) derived in [10]. The observed degree of linear polarization P_s tends to increase toward cooler stars, in agreement with the analogous dependences found by Piirola [4] and Tinbergen and Zwaan [5]. An increase of P_s with decreasing Ro (i.e., with increasing magnetic activity) is also observed. In the Zeeman polarization model, these dependences apparently reflect the well-known relations between the strength and filling factor of local magnetic fields and the global parameters of stars.

5. ACKNOWLEDGMENTS

The author thanks Dr. K.G. Strassmeier and Dr. G. Cutispoto, who kindly presented their photometric data for LQ Hya, VY Ari, and EK Dra. This work was partially supported by the Ukraine State Foundation for Fundamental Development (grant no. 02.07/00300).

REFERENCES

1. I. Yu. Alekseev and R. E. Gershberg, Astron. Zh. **73**, 589 (1996) [Astron. Rep. **40**, 538 (1996)].
2. A. Dollfus, Compt. Rend. **246**, 3590 (1958).
3. J. L. Leroy, Ann. Astrophys. **25**, 127 (1962).
4. V. Piirola, Astron. Astrophys., Suppl. Ser. **30**, 213 (1977).
5. J. Tinbergen and C. Zwaan, Astron. Astrophys. **101**, 223 (1981).
6. R. H. Koch and R. J. Pfeiffer, Astrophys. J. Lett. **204**, L47 (1976).
7. B. R. Pettersen and J. Hsu, Astrophys. J. **247**, 1013 (1981).
8. C. De Jager, J. Heise, S. Avgoloupis, *et al.*, Astron. Astrophys. **156**, 95 (1986).
9. Ju. Huovelin, S. Linnaluoto, V. Piirola, *et al.*, Astron. Astrophys. **152**, 357 (1985).
10. Ju. Huovelin, S. H. Saar, and I. Tuominen, Astrophys. J. **329**, 882 (1988).
11. Ju. Huovelin, S. Linnaluoto, I. Tuominen, and H. Virtanen, Astron. Astrophys., Suppl. Ser. **78**, 129 (1989).
12. R. F. Griffin, Observatory **98**, 257 (1978).
13. R. A. Osten and S. H. Saar, Mon. Not. R. Astron. Soc. **295**, 257 (1998).
14. O. J. Eggen, Astron. J. **69**, 570 (1964).
15. S. M. Rucinski, Acta Astron. **31**, 363 (1981).
16. B. W. Bopp, P. V. Noah, A. Klimke, and J. L. Africano, Astrophys. J. **249**, 210 (1981).
17. B. W. Bopp, J. L. Africano, P. E. Stencel, *et al.*, Astrophys. J. **275**, 691 (1983).
18. I. Yu. Alekseev and N. I. Shakhovskaya, Izv. Krym. Astrofiz. Obs. **89**, 93 (1995).
19. I. Yu. Alekseev, Astron. Zh. **77**, 207 (2000) [Astron. Rep. **44**, 178 (2000)].
20. F. C. Fekel, B. W. Bopp, J. L. Africano, *et al.*, Astron. J. **92**, 1150 (1986).
21. O. J. Eggen, Astron. J. **89**, 1358 (1984).
22. K. G. Strassmeier and D. S. Hall, Astrophys. J., Suppl. Ser. **67**, 453 (1988).
23. L. J. Boyd, R. M. Genet, D. S. Hall, *et al.*, IAPPP Comm. **42**, 44 (1990).
24. L. Jetsu, Astron. Astrophys. **276**, 345 (1993).
25. G. Cutispoto, Astron. Astrophys., Suppl. Ser. **89**, 435 (1991).
26. G. Cutispoto, Astron. Astrophys., Suppl. Ser. **102**, 655 (1993).
27. G. Cutispoto, Astron. Astrophys., Suppl. Ser. **119**, 281 (1996).
28. G. Cutispoto, Astron. Astrophys., Suppl. Ser. **127**, 207 (1998).
29. G. Cutispoto, Astron. Astrophys., Suppl. Ser. **131**, 321 (1998).
30. K. G. Strassmeier, J. Bartus, G. Cutispoto, and M. Rodonó, Astron. Astrophys., Suppl. Ser. **125**, 11 (1997).

31. K. G. Strassmeier, J. B. Rice, W. H. Wehlau, *et al.*, Astron. Astrophys. **268**, 671 (1993).
32. K. G. Strassmeier, D. S. Hall, F. C. Fekel, and M. Scheck, Astron. Astrophys., Suppl. Ser. **100**, 173 (1993).
33. P. F. Chugaĭnov, Izv. Krym. Astrofiz. Obs. **55**, 85 (1976).
34. J. A. Eaton and C. H. Poe, Inf. Bull. Var. Stars, No. 2846 (1986).
35. B. W. Bopp, S. H. Saar, C. Ambruster, *et al.*, Astrophys. J. **339**, 1059 (1989).
36. K. G. Strassmeier and B. W. Bopp, Astron. Astrophys. **259**, 183 (1992).
37. I. Yu. Alekseev, Astron. Zh. **73**, 86 (1996) [Astron. Rep. **40**, 74 (1996)].
38. K. G. Strassmeier, E. Serkowitsch, and Th. Granzer, Astron. Astrophys., Suppl. Ser. **140**, 29 (1999).
39. J. D. Dorren and E. F. Guinan, Astrophys. J. **428**, 805 (1994).
40. S. H. Saar and J. Bookbinder, *Cool Stars, Stellar Systems and the Sun,* Ed. by R. Donahue and J. Bookbinder; Publ. Astron. Soc. Pac. Conf. Ser. **154**, 1560 (1998).
41. M. Güdel, J. H. M. M. Schmitt, and A. O. Benz, Astron. Astrophys. **302**, 775 (1995).
42. M. Güdel, J. H. M. M. Schmitt, A. O. Benz, and N. M. Elias, Astron. Astrophys. **301**, 201 (1995).
43. M. Güdel, E. F. Guinan, R. Mewe, *et al.*, Astrophys. J. **479**, 416 (1997).
44. M. Güdel, E. F. Guinan, and S. L. Skinner, Astrophys. J. **483**, 947 (1997).
45. P. F. Chugainov, M. N. Lovkaya, and G. V. Zajtseva, Inf. Bull. Var. Stars, No. 3680 (1991).
46. G. W. Lockwood, B. A. Skiff, and R. R. Radick, Astrophys. J. **485**, 789 (1996).
47. R. R. Radick, G. W. Lockwood, B. A. Skiff, and S. L. Baliunas, Astrophys. J., Suppl. Ser. **118**, 239 (1998).
48. J. D. Dorren, M. Güdel, and E. F. Guinan, Astrophys. J. **448**, 431 (1995).
49. M. P. Scheible and E. F. Guinan, Inf. Bull. Var. Stars, No. 4110 (1994).
50. Ju. Huovelin and V. Piirola, Astron. Astrophys. **231**, 588 (1990).
51. N. M. Elias and J. D. Dorren, Astron. J. **100**, 818 (1990).
52. N. M. Elias and J. D. Dorren, Inf. Bull. Var. Stars, No. 3541 (1990).
53. V. Piirola, Obs. Astrophys. Lab. Univ. Helsinki Rep., No. 6, 151 (1984).
54. G. Rosselló, R. Calafat, F. Figueras, *et al.*, Astron. Astrophys., Suppl. Ser. **59**, 399 (1985).
55. K. G. Strassmeier and J. B. Rice, Astron. Astrophys. **330**, 685 (1998).
56. I. Yu. Alekseev, *Spotted Low-Mass Stars* [in Russian] (Astroprint, Odessa, 2001), p. 137.
57. I. Yu. Alekseev and O. V. Kozlova, Astron. Astrophys. **396**, 203 (2002).
58. K. Oláh, Zs. Kolláth, and K. G. Strassmeier, Astron. Astrophys. **356**, 643 (2000).
59. I. Yu. Alekseev and O. V. Kozlova, Astrofizika **44**, 529 (2001).
60. Ju. Huovelin and S. H. Saar, Astrophys. J. **374**, 319 (1991).
61. J. D. Dorren, Astrophys. J. **320**, 756 (1987).
62. Z. Eker, Astrophys. J. **445**, 526 (1995).
63. Z. Eker, Astrophys. J. **473**, 388 (1996).
64. J. A. Eaton, G. W. Henry, and F. C. Fekel, Astrophys. J. **462**, 888 (1996).
65. I. Yu. Alekseev and R. E. Gershberg, Astron. Zh. **73**, 579 (1996) [Astron. Rep. **40**, 528 (1996)].
66. I. Yu. Alekseev and R. E. Gershberg, Astron. Zh. **74**, 240 (1997) [Astron. Rep. **41**, 207 (1997)].
67. J. B. Rice and K. G. Strassmeier, Astron. Astrophys. **336**, 972 (1998).
68. S. H. Saar, N. E. Piskunov, and I. Tuominen, *Cool Stars, Stellar Systems and the Sun,* Ed. by M. S. Giampapa and J. A. Bookbinder; Astron. Soc. Pac. Conf. Ser. **26**, 255 (1992).
69. S. H. Saar, N. E. Piskunov, and I. Tuominen, *Cool Stars, Stellar Systems and the Sun,* Ed. by J. P. Caillault; Astron. Soc. Pac. Conf. Ser. **64**, 661 (1994).
70. J. F. Donati, Mon. Not. R. Astron. Soc. **302**, 457 (1999).
71. S. V. Berdyugina, I. V. Ilyin, and I. Tuominen, *Cool Stars, Stellar Systems and the Sun,* Ed. by R. J. Garcia López, R. Rebolo, and M. R. Zapatero Osorio; Astron. Soc. Pac. Conf. Ser. **223**, CD-1207 (2001).
72. S. H. Saar and J. E. Neff, *Cool Stars, Stellar Systems and the Sun,* Ed. by G. Wallerstein; Astron. Soc. Pac. Conf. Ser. **9**, 171 (1990).
73. G. Cutispoto, M. Rodonó, and S. Messina, Astron. Astrophys. **367**, 910 (2001).
74. M. Landi Degl'Innocenti, Astron. Astrophys. **110**, 25 (1982).
75. G. Calamai and E. Landi Degl'Innocenti, Astron. Astrophys., Suppl. Ser. **53**, 311 (1983).
76. D. J. Mullan and R. A. Bell, Astrophys. J. **204**, 818 (1976).
77. M. Landi Degl'Innocenti, G. Calamai, E. Landi Degl'Innocenti, and P. Patriarchi, Astrophys. J. **249**, 228 (1981).
78. S. H. Saar and Ju. Huovelin, Astrophys. J. **404**, 739 (1993).
79. M. Schüssler, P. Caligari, A. Ferriz-Mas, *et al.*, Astron. Astrophys. **314**, 503 (1996).
80. Th. Granzer, M. Schüssler, P. Caligari, and K. G. Strassmeier, Astron. Astrophys. **355**, 1087 (2000).
81. S. H. Saar, *Stellar Surface Structure*, Ed. by K. G. Strassmeier and J. L. Linsky (Kluwer, Dordrecht, 1996), p. 237.

Translated by K. Maslennikov